CRANFIELD UNIVERSITY

MATHIAS TANTAU

Active Magnetic Bearing for Ultra Precision Flexible Electronics Production System

SCHOOL OF AEROSPACE, TRANSPORT AND MANUFACTURING

MSc by Research

Master

Academic Year: 2014–2015

Supervisor: Prof. FREng. Paul Shore, Mr. Paul Morantz

December 2015

This thesis is submitted in partial fulfilment of the requirements for the degree of Master.

Abstract

Roll-to-roll printing on continuous plastic films could enable the production of flexible electronics at high speed and low cost, but the granularity of feature sizes is limited by the system accuracy.

Technologies such as gravure printing and nanoimprint lithography demand a level of rotary motion precision that cannot be achieved with rolling element bearings. Manufacturing tolerances of the rotating parts, thermal drift and process forces in combination with structural compliance add up to additional error motions.

In this master by research an active magnetic bearing (AMB) solution is designed for a new, super-sized roll-to-roll flexible electronics production machine, which was so far based on hydrostatic bearings. The magnetic bearing could actively compensate the accumulated synchronous error and maintain high accuracy under all conditions.

However, the asynchronous error of a conventional AMB with the required size and power is a problem. In order to reduce the relatively high positioning uncertainty of active magnetic bearings an innovative radial position measurement based on linear, incremental encoders with optical conversion principle is proposed. A commercial encoder scanning head faces a round scale with concentric, coplanar lines on its face. By counting these lines the radial position can be measured.

Because such a scale is not readily available, it is made by micro-machining. In experiments, different machining methods are compared. Then a magnetic bearing is built to demonstrate the efficacy of the proposed sensor. As a result, the best measurement noise is 3.5 nm at 10 kHz and a position uncertainty of approximately 0.25 µm has been achieved for the magnetic bearing. These promising results are especially interesting for applications with high precision requirements at low speed of rotation.

Keywords

Active magnetic bearing; AMB; Optical encoder; Flexible electronics; Plastic electronics; Roll-to-roll printing; R2R; Printing machine; Precision sensor; Magnetic bearing design; Grating; Micro-machining; Speedgoat; Imaging scanning principle.

Sponsors

- EPSRC Centre for Innovative Manufacturing in Ultra Precision (EP / I033491 / 1)
- Integrated Knowledge Centre in Ultra Precision and Structured Surfaces (EP / E023711 / 1)
- Dr. Johannes Heidenhain GmbH
- Speedgoat GmbH
- Rittal GmbH & Co. KG

Contents

List of Figures

List of Tables

List of Abbreviations

ADC	analogue digital converter
AFVC	adaptive feed-forward vibration compensation
AMB	active magnetic bearing
ARM	advanced RISC machine
CAN	controller area network
CCD	charge-coupled device
CCI	coherence correlation interferometer
CPU	central processing unit
DAC	digital analogue converter
DC	direct current
DOF	degree of freedom
FEA	finite element analysis
FEM	finite element method
FESEM	field emission scanning electron microscope
FFT	fast Fourier transform
FPGA	field programmable gate array
FRF	frequency response function
HDL	hardware description language
IC	integrated circuit

ISA	Industry Standard Architecture
IO	input/output
JTAG	Joint Test Action Group
LBS	laser beam sensor
LED	light emitting diode
OP-AMP	operational amplifier
OPRA	overlay printing registration accuracy
P/A	pattern positioning accuracy
PC	personal computer
PCI	Peripheral Component Interconnect
PCIe	Peripheral Component Interconnect Express
PET	polyethylene terephthalate
PSD	position sensitive device
PWM	pulse width modulation
QPD	quadrant photo diode
R2R	roll-to-roll
RFID	radio-frequency identification
RISC	reduced instruction set computing
rpm	rotations per minute
RTAI	real-time application interface
TFT	thin film transistor
UART	universal asynchronous receiver transmitter
UV	ultraviolet
UV-NIL	ultraviolet nanoimprint lithography

Acknowledgements

The author would like to thank his supervisors Prof. Paul Shore and Mr. Paul Morantz for their guidance and their generosity in buying all the lab equipment.

The author also acknowledges the micro-machining work done by the Integrated Knowledge Centre in Ultra Precision and Structured Surfaces in North Wales and especially the support from the business manager Mr. John Allsop.

Many grateful acknowledgements to the technicians in the laboratory by the names of Mr. Alan Heaume, Mr. Andrew Eve, Mr. John Hedge and Mr. Kevin Howard. It is highly appreciated that they immersed themselves in the arising problems and established friendly and pleasant working conditions.

Thanks to Cranfield University for permitting the author to attend a number of taught courses covering precision engineering, metrology, technical writing, research integrity, conducting experiments and ethical research. They have all proven valuable and very helpful. Last but not least, the help of fellow students and all the other members of staff who where involved shall also be acknowledged.

Best wishes for the future and success with the R2R project. It would be nice to hear that the magnetic bearing has actually been put into practice as a new research base for magnetic bearings in the UK. The author will treasure the research experience and recommend the university to other German students.

Chapter 1

Introduction

Chapter 1 first explains the application that stimulates the interest in magnetic bearings and then goes into more details concerning the specifications for the magnetic bearing.

1.1 Stimulus of research: flexible electronics machine

This research deals with the development of an active magnetic bearing (AMB) for the printing roller of a new roll-to-roll (R2R) flexible electronics production machine. Flexible electronics are the counterpart of circuits on a rigid substrate with brittle materials for electrodes, resistors, electrolytes and semiconductors. Because the flexibility is often, albeit not necessarily, achieved with conductive polymer inks printed on polymer substrates, the phrase plastic electronics is also common. The idea of roll-to-roll production is that the flexibility of the substrate is utilized to print electronic circuits in a continuous process on a plastic film that reels off from one roller and re-reels on another roller after the printing process. The single devices are cut into their final size afterwards [19, 15].

The machine for R2R printing of flexible electronics is still in development, but the planned arrangement can already be seen in the Siemens NX export in figure 1.1. It is

a research platform that can flexibly be rearranged to cover a variety of research topics around plastic electronics: ultra-precision film steering of a 1,400 mm wide, continuous plastic web at high throughput rates, accurate real-time position measurement of the fabricated film to evaluate the film-steering capabilities, gravure printing, inkjet printing and ultraviolet light nanoimprint lithography (UV-NIL) on a continuously moving film [29, 28].

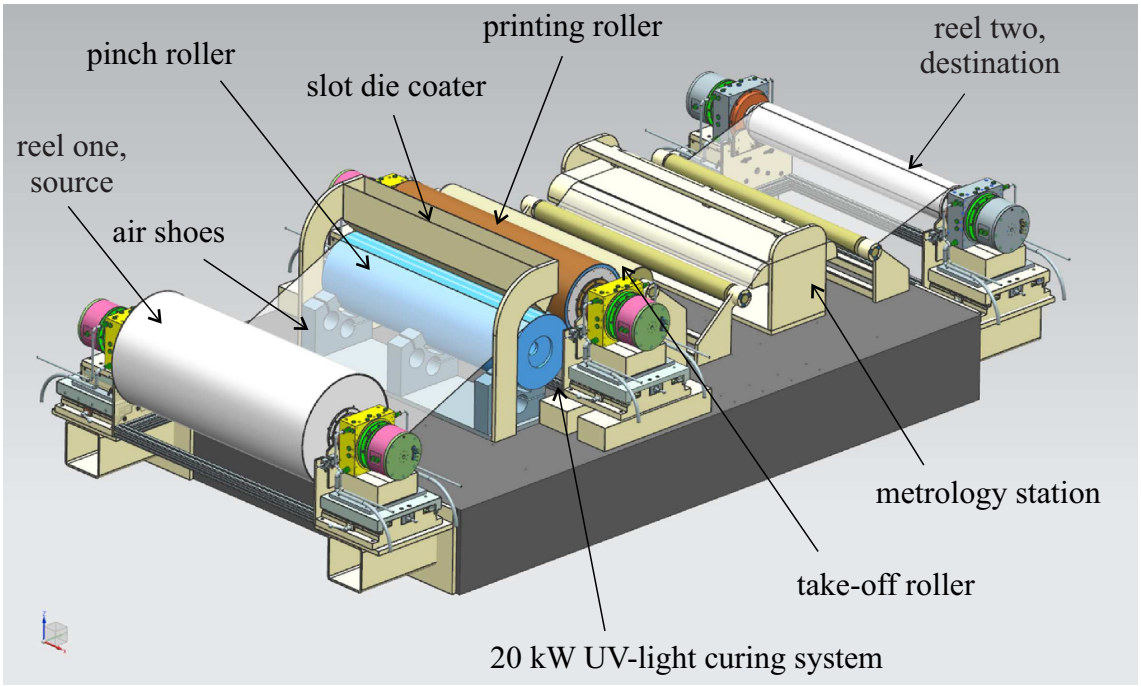

Figure 1.1: CAD image of roll-to-roll machine layout generated in Siemens NX by Roger Read from Cranfield University

The displayed arrangement supports UV-NIL, which works as follows: When the film reels off from the first reel, it is coated with a resist by the slot die coater. The pinch roller (also nip roller, press cylinder or support roller) then presses the film against the printing roller or patterning roller, which has a structured surface, a prefabricated mould. These structures are embossed into the liquid resist on the film. A UV-light under the printing roller hardens the resist before the take-off roller behind the printing roller separates film

and mould again. Finally the web is re-reeled [80, 27, 29].

In gravure printing the structured printing roller is temporarily immersed in an ink depository and a doctor blade wipes off the excess ink. Only the content of the cavities in the roller surface remains and is rolled on the substrate. Again the nip roller presses the film against the printing roller or gravure roller. In contrast to NIL the film is separated from the gravure roller before the resist is hardened [84, 14].

While good feature fidelity of UV-NIL and gravure printing has been demonstrated for R2R and nanometre scale features [71], the granularity of printable features is still limited by a lack of cleanliness and accuracy [84]. One problem is the residual layer of resist in places where it should be squeezed away by the mould or wiped off by the doctor blade, respectively [84]. Another problem is the non-uniformity of the resist layer due to deformations of the soft mould material [84, 71]. A hard mould can help if the process accuracy is so high that no elastic averaging is necessary [71].

An important quality indicator is the "overlay printing registration accuracy (OPRA)" [84], p. 275 or register error [65]. It is the maximum relative distance between two points in different layers that are meant to be printed in the same position. The OPRA directly limits the minimum transistor size. For example, with tolerances of $\approx \pm 50\,\mu m$ transistors cannot be smaller than $200\,\mu m$ [84]. TFTs are visually affected by defects or they do not work at all. Well established media printers are based on human perception and tolerate $100\,\mu m$ misalignments [85]. Current R2R facilities have $\pm 20\,\mu m$ OPRA, but for reliable TFT circuits that compare to Si-based TFTs the OPRA had to be improved to $\pm 5\,\mu m$ or $\pm 1\,\mu m$ [86, 85]. Main limitations to sufficient OPRA are vibrations, variability in web tension and thermal expansion [84]. Synchronization errors between rolls and roll eccentricities also enhance the OPRA [65].

Another quality indicator is the "pattern positioning accuracy (P/A)" [15], p. 3. This quality indicator deals with the deviation of a pattern position on each layer from its

target position. Apart from the film steering accuracy the P/A is limited by dynamic or kinematic errors in the system. The precision of each element like roll circularity, which is only as good as the machining capabilities allow it, causes deterioration in the P/A. High accuracy is "the biggest technical hurdle" [15], p. 1 in R2R printing [15].

The claim behind the new plastic electronics production machine is that high accuracy of the printing and nip roller in combination with a hard mould is a necessary step in solving the above accuracy problems. A simple and low cost setup can demonstrate basic principles of operation, but for a product with features small enough for display backplanes, RFIDs and others higher precision levels are required. Apart from the film steering it is not least down to the bearings to achieve the necessary accuracy under all conditions [27, 29, 28].

In the past the suitability of hydrostatic bearings for the printing roller has been investigated by Zhao [129]. The idea of this research project is that active magnetic bearings (AMB)s could be even better. Given the fact that precision is crucial to the functionality of the machine, magnetic bearings with their active control could be superior to passive bearings because they can eliminate geometric errors in the whole construction that are not directly related to bearing imperfections.

The literature review in chapter 2 explains the assets of magnetic bearings in more detail and analyses how magnetic bearings generally compete with other bearing technologies. Remaining questions are addressed in chapter 3 by designing a magnetic bearing for the machine. The main limitation of AMBs is the subject of the experiments in chapters 4 and 5. Finally, discussion, conclusion and future work are subject of chapters 6 and 7.

1.2 Bearing specifications

For the comparison of bearing technologies and for the design of a suitable magnetic bearing it is necessary to collect the specifications for the printing roller bearings. Some specifications can be adopted from the previous machine design and from publications of the research centre. The specifications that are magnetic bearing specific have to be initially defined.

Figure 1.2 shows a cross section view of the hydrostatic bearing of the printing roller with motor[1]. In addition to carrying the rotor the bearing also incorporates the angular encoder, the connection to the base and the flange for the connection to the printing roller on the left of figure 1.2. The AMB requirements are summarized in table 1.1. Spacial requirements result from the demand to build a magnetic bearing with the same connections as the hydrostatic bearing and about the same size, which is known from [129].

A benefit of the magnetic bearings is that they can compensate for errors that are not directly caused by the bearings, see section 2.1.4. Criterion 50 refers to the maximally expectable radial error that has to be compensated. Only a maximum run-out of 100 µm along the axis is allowed, i.e. ±50 µm, the remnant is reserved for static or quasistatic errors.

A load capacity of 1,500 N for each radial bearing is defined in [129] for the hydrostatic bearing. This is related to the spindle mass of approximately 200 kg. The film tension that acts upon the roller in horizontal direction is far below this value [40]. The specified magnetic bearing load capacity is two times higher because the static force of a magnetic bearing with two opposing electromagnets should be less than the load capacity [10]. The minimum axial load capacity is also twice the value defined in [129].

Point 80 follows from publications of the research centre [29, 28]. With a maximum

[1] The motor is of type TMK0175 from ETEL - motion technology.

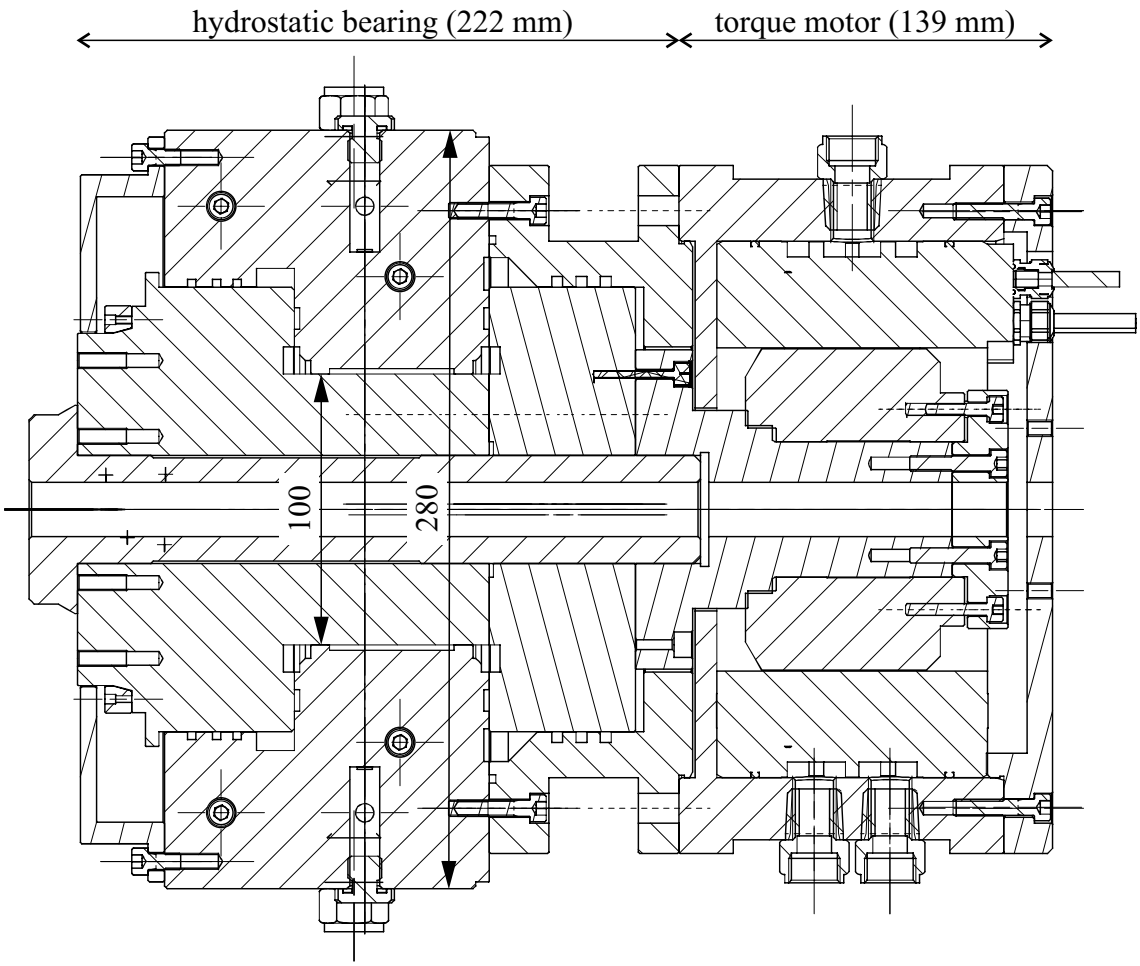

Figure 1.2: Section view of the printing roller's hydrostatic bearing with torque motor, designed by Roger Read from Cranfield University

film speed of 5 m/s and a cylinder diameter of 400 mm the fastest angular frequency of the printing roller that can occur is 239 rpm. 300 rpm velocity stability is safer for the bearing.

The positioning accuracy of the printing roller is defined by the achievable OPRA. $\pm 20\,\mu$m would be competitive already, but the long-term aim should be $\pm 1\,\mu$m or $\pm 5\,\mu$m [85]. In the annual report of the research centre 5 µm is set as the target specification for up to 3 m/min traversing speed [27]. The requirement for the P/A is 1 µm in each step [27]. The same value is assumed for the printing roller surface position. Allowing

Table 1.1: Spacial and functional requirements for the active magnetic bearing

Index	Requirement	Value min	Value opt	Value max	Unit
10	Length housing	-	222	300	mm
20	Width housing	-	280	300	mm
30	Height housing	-	280	300	mm
40	Shaft diameter in bearing	90	100	-	mm
50	Lateral range of compensation movement	± 100	± 200		µm
60	Radial load capacity, each	3,000	-	-	N
70	Axial load capacity	1,000	-	-	N
80	Angular velocity stability	300	-	-	rpm
90	Positioning accuracy, radial	-	± 0.25	± 0.5	µm
100	Positioning accuracy, axial	-	± 0.25	± 0.5	µm
110	Temp. rise of housing	-3	0	3	K

$\pm 0.5\,\mu$m remaining synchronous error motion of the spindle after repeatable errors have been compensated by the magnetic bearing, the permissible asynchronous error has to be as low as $\pm 0.5\,\mu$m at $3\,$m/min traversing speed.

Point 110, the temperature rise of the AMB housing during operation is defined for the hydrostatic bearing in [129]. It should be aimed at maintaining an average temperature equal to the room temperature of 20°C.

Chapter 2

Literature review and theory

This chapter covers a short comparison of common bearing technologies to warrant the choice of active magnetic bearings and also to point out potential shortcomings of this technology. These are installation space, stiffness, positioning noise and price. These shortcomings (excepting the price) are treated in more detail in the subsequent sections to differentiate the problems. Theory needed to design a magnetic bearing is also covered.

2.1 Comparison of bearing technologies

This section is not aimed at giving an exhaustive overview of different kinds of bearings, but it will establish a basis for the evaluation of magnetic bearings. Commercially available high precision rolling element bearings, hydrostatic oil bearings and air bearings are considered serious alternatives for this application.

2.1.1 Rolling element bearings

The load carried by a rolling bearing is transmitted through balls or rollers from one ring to the other. Ball or roller bearings can be mounted with interference fit to reduce the clear-

ance in the bearings, which makes them interesting for higher precision requirements. This is often achieved with tapered shafts or tapered sleeves, opposed angular-contact ball bearings and pre-loading [42]. Still, the accuracy depends on the machine component which the bearing is mounted to. For example, if a perfectly round outer ring is pressed into an out-of-round hole, the bearing will have large errors. Also, the form accuracy of the raceway needs to be high. Under ideal mounting conditions a radial bearing with 120 mm bore size and the best available tolerance has 3 µm total radial error motion [108].

The radial bearing stiffness in a particular direction varies as the balls or rollers recirculate. This causes a non-repeatable error motion when the bearing rotates under load. Double-row bearings have twice as many rolling elements and the effect is reduced slightly [108, 63].

Relevant advantages of rolling bearings are:

- Cool operation, in most applications, especially at low speeds or low loads no thermal consideration required [42]
- High stiffness [4]
- High load capacity combined with compact design [91]
- Easy to buy and cost effective

Relevant disadvantages are:

- Low accuracy, getting worse as the bearing ages [9]
- Additional errors due to thermal displacement [63]
- High and fluctuating friction especially at low speed with Coulomb characteristic, caused by the sources: elastic hysteresis, sliding in the raceways, sliding between

the cage and the rolling elements, seal friction and others [42]. This is not reconcilable with high precision rotary speed control.

- Very low damping [63, 119, 4]

(a) Type with excentric rings (b) Locating bearing type

Figure 2.1: Two examples of roller bearings for printing machines from the company FAG [99]

Consider the following two examples of rolling bearings as a solution for the R2R machine: Schaeffler Group Industrial with the brands INA and FAG offers special rolling bearings for printing machines. These are clearance-free single or multi row needle bearings. Eccentric rings allow the radial fine-adjustment of the axis of rotation to adapt the distance between the centre lines of grouped rollers, see figure 2.1, a. For locating bearings tapered rollers or radial cylindrical rollers with thrust needle rollers (figure 2.1, b are available [99]. The part DML3E105x210x80, for instance, is a two or four row radial roller bearing with location adjustment ring. The dynamic load capacity of the two row version is 219 kN, the stiffness is $1,429\,\mathrm{N}/\mu\mathrm{m}$ at a static load of 20 kN. It is suitable

for a shaft with 105 mm diameter and its outer dimensions are $210 \times 80\,\mathrm{mm}^2$. The frictional torque is 0.04725 Nm. The radial run-out of the inner ring is 5 µm and 10 µm is the run-out of the outer ring at tolerance class P4 [99].

The company SKF provides roller bearings with similar properties and finer tolerances: 3 µm radial run-out for inner ring and outer ring of a radial bearing with the same dimensions as the above mentioned one [106].

2.1.2 Hydrostatic bearings

A hydrostatic bearing or fluid static bearing supports relative sliding movements of two members with respect to each other by means of fluid in a narrow gap. The fluid is pressurised by an external pump and then fed into the gap through flow resistors. In combination with the resistance from the narrow gap they act as a compensation mechanism, that makes the pressure in the recesses adjust in response to an external load. The rotor is hence always precisely centred in a journal bearing if no load is applied. Error motions smaller than the cylinder form tolerances are expectable, because the fluid provides averaging [111].

The term hydrostatic allows the fluid to be either be a liquid or a gas. Air-lubricated bearings are called aerostatic bearings or air bearings whereas oil-lubricated bearings are referred to as hydrostatic bearings or oil bearings [117]. Air bearings have a lower stiffness at the same gap size owed to the low viscosity of air[1] and their load capacity is limited by the allowable supply pressure. Air bearings have no passive lubrication and they provide less damping[2] than oil bearings [93]. Oil is therefore more interesting for the R2R bearing and air bearings are not further considered.

[1] The reduced viscosity can be remedied with a smaller gap, but manufacturing tolerances set a limit [117].

[2] Wide lands and small pockets are incorporated to overcome this restriction or pads filled with porous material [33].

Stiffness and friction of hydrostatic bearings depend on the speed of rotation. Hydrodynamic actions dominate the stiffness of oil bearings at high speeds. They drag fluid into narrowing regions between the bearing members and the stiffness rises (squeeze-film effect). The squeeze-film effect dissipates energy which means good damping[111]. The smaller the clearance of the bearing the higher is the stiffness, but again the manufacturing tolerances set a limit [129]. The load capacity is limited by the supply pressure, about 1 MPa for air bearings and 4 MPa for oil bearings [61].

The following advantages can be derived from the structure of oil bearings:

- High accuracy of axis of rotation because of the averaging effect of the fluid [63]
- High stiffness and higher load capacity over a large frequency range than many other bearing types [93, 63]
- Good vibration and shock resistance [129]
- High damping [63]
- Low friction at low speed, only caused by the forces that sheer the oil, no Coulomb friction [111]

Relevant disadvantages are:

- Heat generation in the bearing due to oil shearing causes thermal drift [111, 63].
- Major impact of the recirculation system including pump, piping and filters on the initial costs and the subsequent maintenance in addition to the maintenance of the bearing itself [111, 93, 63]
- Need for smooth and coated surfaces with narrow form tolerances [129]
- The bearing characteristics change as the temperature of the oil rises [129].

Some features of the current R2R oil bearing solution have been investigated by Zhao [129]. The summary of his findings in table 2.1 allows an assessment of the printing roller spindle performance with hydrostatic bearings[3].

Table 2.1: Properties of one hydrostatic bearing in the R2R machine after [129]

Bearing	Calculated load capacity	Measured stiffness	Measured temperature rise	Deflection due to oil pressure
Journal	9.09 kN	$80-100\,\mathrm{N/\mu m}$	10 K	2.97 µm
Thrust	5.28 kN	$21.2-84.8\,\mathrm{N/\mu m}$	10 K	5.83 µm

No accuracy measurement has been done for this set of bearings, but it can be estimated. As to [111] the run-out without load of a hydrostatic bearing is one-fourth of the roundness and the cylinder surfaces in the journal bearing have been manufactured with a cylindricity specification of 1 µm. The resulting synchronous error related to form tolerances thereby comes to 250 nm.

2.1.3 Active electromagnetic bearings

In rotational active magnetic bearings the shaft is encompassed by a soft iron sleeve or a disc that is pulled in opposing directions by electromagnetic coils. The position of the rotor is measured without contact and the coil currents are controlled actively to levitate the rotor.

Some popular advantages of AMBs are:

- Stiffness and damping adjustable within limits [13]
- Active unbalance compensation possible: reduced unbalance induced deflection or rotation about the centre line of inertia [44, 105, 18]

[3] Deflections due to oil pressure have been simulated with ANSYS [129].

- Usable for fault diagnosis and rotor dynamics identification [2]
- Special features like constant process force control possible [11]

Disadvantages:

- Accuracy of rotation limited by the precision of the sensors [13]
- Low carrying capacity, four times below hydrostatic oil bearings with the same size [10].
- Low stiffness at medium frequencies, difficult to predict [22]
- Expensive compared with rolling element bearings [13, 22, 62]
- Application specific development required, no all-round products available, often years of engineering work [91]

The disadvantage of high power consumption can be overcome with hybrid magnetic bearings. Permanent magnets carry the static loads and electromagnets only stabilize minor deflections from the ideal position [112]. This low energy operation goes on expense of the precision and is therefore not further considered.

2.1.4 Making the decision

The target specification that suggests the use of active magnetic bearings is the accuracy of rotation. The analysis has shown that a rolling element bearing of the required size would not be precise enough. Because the machine is currently based on hydrostatic bearings, it is possible to compare hydrostatic bearings and magnetic bearings. A comparison between the rolling element bearings and the magnetic bearings would lead to the same conclusion.

As explained above the rotor of a hydrostatic bearing is precisely centred with respect to the bearing stator if no forces are applied, but this still does not mean that the position of the printing roller surface is precise to 1 µm under all circumstances: Under load the hydrostatic journal bearing gives way with a stiffness of $80-100\,\mathrm{N/\mu m}$. For example the gravity induced force of 1 kN makes the axis move 11 µm and the finite stiffness of the entire structure increases the compliance further. It can be assumed that the process forces change slowly over time, for example because of resist remnants and contaminations. It is therefore not possible to compensate all force induced deflections by manual adjustments. Furthermore, the oil bends the aluminium and it raises the temperature (table 2.1). Most importantly, the bearing lands will always have a run-out with respect to the roller. The entire shaft is not machined in one piece but it has flanges for changing the printing roller. This creates interfaces with high concentricity and perpendicularity requirements. The concentricity could be adjusted each time the printing roller is changed, but that would be time-consuming and difficult to measure. In the current design it is not possible to adjust the run-out.

Moreover, the combination of two cylindrical hydrostatic bearings is over-constraint. When the printing roller is changed to refresh the printing patterns, which wear off, a time-consuming process of aligning the two housing stators has to be undertaken. Conditions have to be kept constant during operation to prevent contact between the parts with only 25 µm oil gap in between. Solutions with flexible coupling on one end of the printing roller have been discussed, but this would reduce the stiffness.

A magnetic bearing could compensate for all these errors and because of the wider air gap the assembly is facilitated. Successful realisations of this idea, albeit in different applications are described in [59] for a linear magnetic bearing and in [64] for a rotary, radial bearing. Error motions and deflections of the entire R2R system could be measured and used to predict the behaviour of the roller. It is the idea to evaluate the production

outcome constantly in order to calculate correction motions for the following metres of film. For instance monitoring the roughness of the printed structures over one revolution represents run-out errors that can be compensated in the next revolution. In the long run magnetic bearings could also be used to support the film steering.

Having introduced magnetic bearings as a solution to all the problems with passive bearings the disadvantages are discussed now. The asynchronous error of rotation is the most important limitation. Although synchronous disturbances can be compensated, a certain level of noise will always remain. The asynchronous error of magnetic bearings is analysed more thoroughly in the following sections. The second disadvantage in the above listing, the low carrying capacity at a given installation space raises the question of restrictions to the load capacity. The stiffness is adjustable, but there are limits. How is the stiffness adjusted and what are the boundaries? How does the stiffness depend on the frequency? Price and development effort have to be considered at the design state.

An alternative to magnetic bearings may be the use of oil or air bearings in combination with a fast tool servo. In tool machines fast tool servos are used to compensate for straightness errors of guideways, imperfections of ball screws and periodic errors of roller bearings [58, 114, 38]. Here it is considered more elegant to have one bearing with the capability to perform active movements rather than having positioning systems that move the entire housing of the bearing. Fast tool servos have a very high bandwidth with light targets but when moving the bearing housing the reaction to a command would always be delayed owned to the limited fluid bearing stiffness [58]. Furthermore it is questionable if a fast tool servo with three directions of movement would be less complex than a magnetic bearing.

2.2 Magnetic bearings

Following the general discussion of AMB advantages and disadvantages this section analyses their characteristics more thoroughly to evaluate their suitability and also to provide background knowledge for the design of a magnetic bearing.

2.2.1 Introduction

Magnetic bearings are well established in a number of applications and excessive literature on different facets of their design and control is available. The textbooks [101, 112, 10, 81] are recommended.

Applications of AMBs that have been analysed thoroughly and are described in papers are:

- Turbo-molecular vacuum pumps, where the absence of lubricants and contaminating wear is advantageous [81]
- Energy storage flywheels: The high frequency stability and the low friction are utilized in this application [16].
- Blood pumps: The suspension without contact spares the blood cells [73]
- Generators in power stations where maintenance is a problem and reliability is important [116]
- Compressors operate at high speed and benefit from low friction and long periods of time without servicing [124]
- A newer and rather rare application is the use in machine tools, initially described in 1993 [91, 22]

- In hard disk drives (HDD) AMBs could outweigh external vibrations, but because of their low stiffness currently fluid film bearings are preferred [4].

There are a few patents that describe the use of AMBs in printing machines [8, 36, 82]. The patents suggest the application of radial and axial magnetic bearings to perform lateral and axial translations and tilts. These could serve the film steering, they could eliminate vibrations due to friction, they could serve to adjust a constant process force or a certain force profile in response to a process induced displacement. Also, the drive currents of the AMB coils could be used as an indicator of the roll weight, which changes when the drum wears off. Finally, magnetic bearings could compensate for position changes of the rollers [8, 36, 82]. But the use of AMBs in printing machines has hardly been investigated in research and media printing machines work on a different precision level so that the performance requirement for a magnetic bearing in such a machine is different. High precision R2R printing with magnetic bearings has not been described yet.

Figure 2.2 shows a possible structure of a heteropolar radial bearing[4] and a thrust bearing. The coils make magnetic fields recirculate in the iron and they are typically grouped into four independent channels in the radial bearing and two channels in the thrust bearing case. These numbers result from the degrees of freedom multiplied by two directions of movement. Figure 2.2(a) shows a variant with eight poles. Three poles or more than eight are also possible [13].

The shown AMBs exhibit variable reluctance actuators with electromagnetic forces on permeability boundaries in contrast to Lorentz force based electrodynamic actuators. A magnetic bearing is called "active" if the position is stabilized by a sensor-actuator closed loop. Completely passive bearings (that means no control) based on repulsive forces from permanent magnets are also possible but according to the Earnshaw stability criterion they

[4]Heteropolar means that the magnetisation of the rotor changes when it rotates because the magnetic field lines penetrate the rotor in circumferential direction. The opposite is homopolar with axial flux [112].

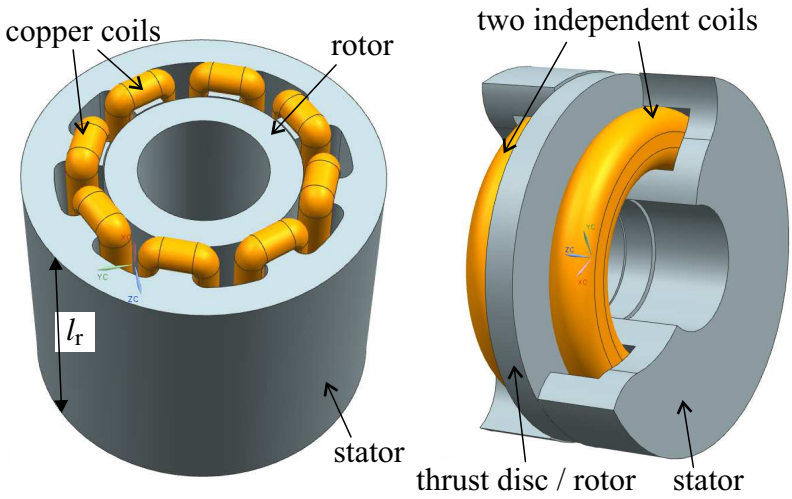

(a) Radial bearing (b) Axial bearing

Figure 2.2: Radial and axial version of active magnetic bearings based on reluctance force, Siemens NX models

cannot stabilize the shaft in all directions. At least one degree of freedom still must be controlled actively [66]. Lembke [66] gives an overview of achievements with passive magnetic bearings. See [10] for a full classification of magnetic bearings.

Variable reluctance actuators with active electromagnetic transducers are most common, because they show the strongest forces, the best damping and a simple structure. Lorentz force magnetic bearings, i.e. electrodynamic devices are favoured if hysteresis is a problem [10].

The pictures do not show the auxiliary bearings, also called retainer bearings or touch-down bearings. An active magnetic bearing needs additional rolling element bearings or sliding bearings that are wider than the shaft and do not revolve during normal operation. Their purpose is to prevent contact between rotor and stator if the system fails or the load exceeds the bearing's capacity [10].

2.2.2 Derivation of the force on a radial bearing rotor

In order to evaluate the feasibility of the specifications and to contemplate the characteristics of magnetic bearings it is important to reflect on the forces and the non-linearities. Figure 2.3 shows the schematic of a radial magnetic bearing with eight poles. One coil out of four independent coils is displayed. The two halves of the coil are connected in series and the total number of windings is n. The stator of this radial bearing has an inner diameter of d_r. Between rotor and stator is the air gap with a length of s_0. Small radial deviations x in the rotor position increase the air gap on one side and reduce it on the opposing side.

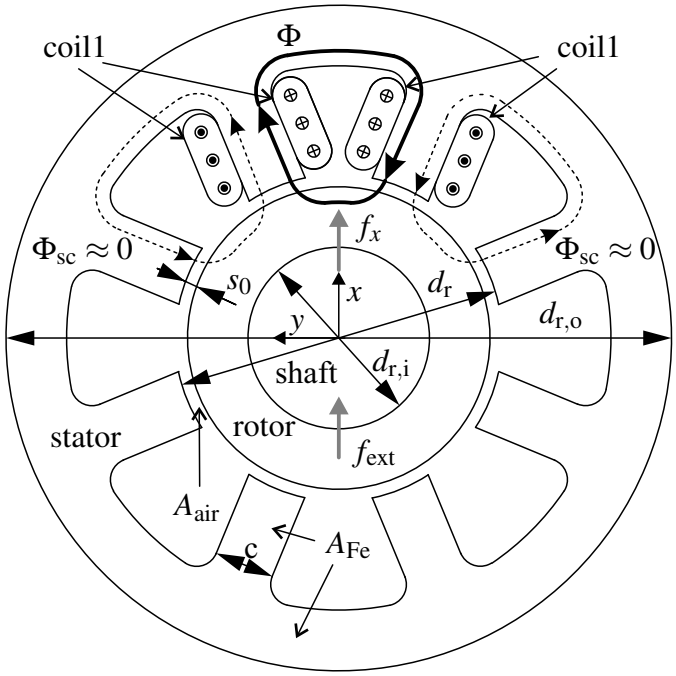

Figure 2.3: Radial bearing schematic with magnetic flux Φ resulting from one coil

In contrast to a Lorentz actuator the force of a reluctance actuator is a non-linear function of the coil current i and the rotor position. In [81] the force of a general reluctance actuator is calculated from the energy equilibrium. The shortened version of this deriva-

tion can be found in appendix A. As a result, the force from the displayed coil acting on the radial bearing rotor can be written as

$$f_{x1} = \frac{1}{2} i^2 \frac{\mathrm{d}L(x)}{\mathrm{d}x}. \tag{2.1}$$

For the inductance $L(x)$ the magnetic reluctances in air $R_{\mathrm{m,air}}(x)$ and in iron $R_{\mathrm{m,Fe}}$ are calculated as functions of the iron path length l_{Fe}, the nominal air gap s_0 and the current deviation x from the nominal width. μ_{rFe} is the relative permeability in iron and A_{Fe} and A_{air} are the respective cross-section areas, see figure 2.3. The inductance results [50]:

$$L(x) = \frac{n^2}{R_{\mathrm{m}}(x)} = \frac{n^2}{R_{\mathrm{m,Fe}} + R_{\mathrm{m,air}}(x)} \tag{2.2}$$

with

$$R_{\mathrm{m,Fe}} = \frac{l_{\mathrm{Fe}}}{A_{\mathrm{Fe}} \mu_{\mathrm{rFe}} \mu_0} \quad \text{and} \quad R_{\mathrm{m,air}}(x) = \frac{2s_0 - 2\cos(\frac{\pi}{8})x}{A_{\mathrm{air}} \mu_0}. \tag{2.3}$$

For this calculation all scattering effects are neglected ($\Phi_{\mathrm{sc}} = 0$) and equal cross section areas are assumed ($A_{\mathrm{air}} = A_{\mathrm{Fe}} = A_{\mathrm{r}}$). Merging the equations (2.1), (2.2) and (2.3) leads to the force on the rotor in x-direction from coil 1:

$$\begin{aligned} f_{x1} &= \frac{1}{2} (ni)^2 \frac{\mathrm{d}}{\mathrm{d}x} \frac{A_{\mathrm{r}} \mu_0}{\frac{l_{\mathrm{Fe}}}{\mu_{\mathrm{rFe}}} + 2s_0 - 2x\cos(\frac{\pi}{8})} \\ &= (ni)^2 \frac{\cos(\frac{\pi}{8}) A_{\mathrm{r}} \mu_0}{\left(\frac{l_{\mathrm{Fe}}}{\mu_{\mathrm{rFe}}} + 2s_0 - 2x\cos(\frac{\pi}{8})\right)^2}. \end{aligned} \tag{2.4}$$

The impact of other coils on the rotor is the same for the respective direction and more than one coil may be active at a given time, see section 2.2.3. The maximal admissible

current is softly limited by the heat that can be accommodated by the chilling system [10]. Another limitation is the saturation of the iron that occurs at higher flux densities, see section 3.1.

For the axial bearing the calculation is analogue and the result only looks different because the force is exactly parallel to the direction of movement:

$$f_{z1} = \frac{(ni)^2 A_\mathrm{a} \mu_0}{\left(\frac{l_\mathrm{Fe}}{\mu_\mathrm{rFe}} + 2s_0 - 2z\right)^2}. \tag{2.5}$$

z is the deviation from the nominal position in axial direction and A_a is the cross-section area of the axial bearing's iron circuit.

2.2.3 Dependencies of the force on the current and the displacement

Equation 2.4 shows that the force is proportional to i^2 and approximately inversely proportional to the air gap length squared. So, the system is non-linear even if saturation effects are neglected. A linear model, which often facilitates the control circuit development, seems inappropriate. This is a drawback of AMBs.

Typically, two opposing coils are turned on at the same time so that the resulting force is reduced to the difference between the two forces that pull in opposite directions. In a simple bias current approach one coil is driven with the current $I_0 + \Delta i$ and the opposing one with the current $I_0 - \Delta i$ [115, 127]. This is called constant current sum (CCS) or Class A control [41]. I_0 is a constant bias current of the size 0.2 to 0.5 times the maximal admissible current of the bearing [10]. Δi is the control current. The resulting force

$$f_x = \frac{n^2 (I_0 + \Delta i)^2 \cos(\frac{\pi}{8}) A_\mathrm{r} \mu_0}{\left(\frac{l_\mathrm{Fe}}{\mu_\mathrm{rFe}} + 2s_0 - 2x\cos(\frac{\pi}{8})\right)^2} - \frac{n^2 (I_0 - \Delta i)^2 \cos(\frac{\pi}{8}) A_\mathrm{r} \mu_0}{\left(\frac{l_\mathrm{Fe}}{\mu_\mathrm{rFe}} + 2s_0 + 2x\cos(\frac{\pi}{8})\right)^2} \tag{2.6}$$

is illustrated in figure 2.4 ($\mu_{\mathrm{rFe}} \to \infty$). If the rotor is centred, i.e. $x \approx 0$, the force-current-relation becomes a linear function of Δi:

$$\begin{aligned} f_x|_{x=0} &= \frac{n^2 \cdot \cos(\frac{\pi}{8}) A_\mathrm{r} \mu_0 \left((I_0 + \Delta i)^2 - (I_0 - \Delta i)^2 \right)}{\left(\frac{l_\mathrm{Fe}}{\mu_\mathrm{rFe}} + 2 s_0 \right)^2} \\ &= \frac{n^2 \cdot \cos(\frac{\pi}{8}) A_\mathrm{r} \mu_0 \cdot 4 I_0 \Delta i}{\left(\frac{l_\mathrm{Fe}}{\mu_\mathrm{rFe}} + 2 s_0 \right)^2}. \end{aligned} \tag{2.7}$$

As a consequence, a constant force-current factor c_i can be calculated or identified, as demonstrated in [127], if the rotor is operated in a position close to the bearing centre. This factor depends proportionally on the bias current I_0, as can be derived from equation 2.7. The derivative of the force with respect to the control current Δi is qualitatively displayed for different bias currents in figure 2.5. The figure also shows, how the factor changes, if the rotor is moved out of centre. Only for small deflections the changes are negligible. To ensure force-current linearity, Δi shouldn't rise above I_0 and the bearing can only react to disturbances fast if c_i is high, because the coil inductance limits the current slope. For these two reasons the bias current is chosen high if energy consumption is not an issue [92, 105].

During normal operation and without static load the control current Δi is close to zero. The resulting force-displacement slope for $\Delta i = 0$

$$\begin{aligned} c_x = \left. \frac{\mathrm{d} f_x}{\mathrm{d} x} \right|_{\Delta i = 0} &= \frac{\xi}{\left(\frac{l_\mathrm{Fe}}{\mu_\mathrm{rFe}} + 2 s_0 - 2 x \cos(\frac{\pi}{8}) \right)^3} + \frac{\xi}{\left(\frac{l_\mathrm{Fe}}{\mu_\mathrm{rFe}} + 2 s_0 + 2 x \cos(\frac{\pi}{8}) \right)^3} \\ \text{with} \quad \xi &= 4 n^2 \cos\left(\frac{\pi}{8} \right)^2 A_\mathrm{r} \mu_0 I_0^2 \end{aligned} \tag{2.8}$$

is not a linear function like the force-current relation, but figure 2.6 shows that the slope is almost constant for small deflections. This fact gives the AMB a spring-like

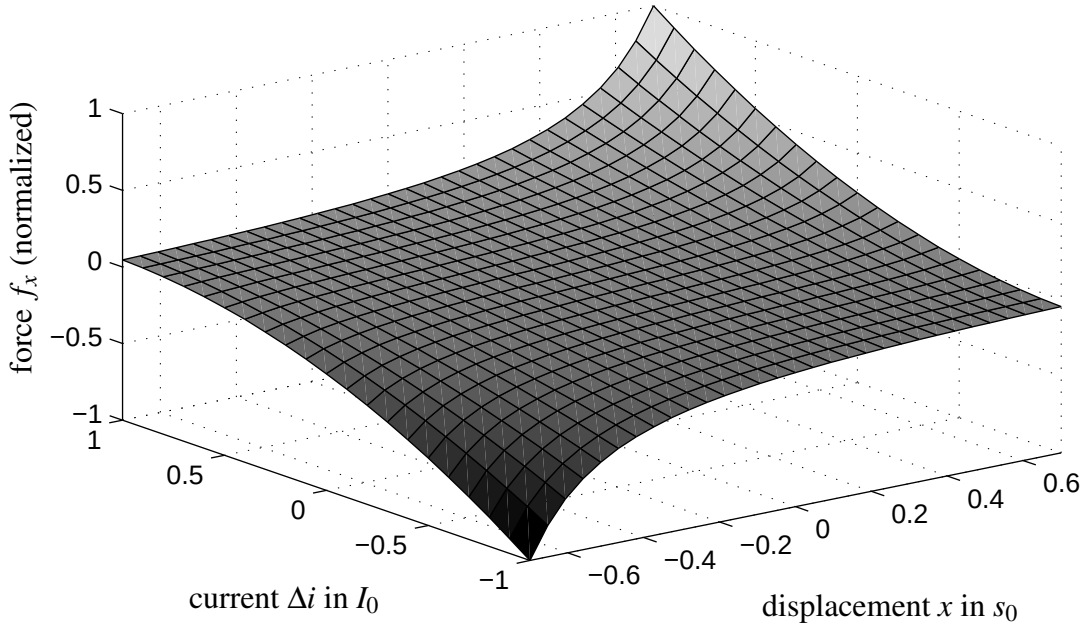

Figure 2.4: Force f_x with respect to x (unit: s_0) and Δi (unit: I_0)

behaviour, excepting that the force has the wrong sign. It strives to amplify deflections instead of stabilizing the system like a spring would. This derivative is also called 'passive stiffness' [122], as opposed to the active stiffness of a spring. For operations close to $x = 0$ a constant force-displacement factor c_x can be used. Because of the iron saturation the force is smaller at great deflections than calculated with this simple estimate. The flux density does not rise above a certain saturation level and thus the slope declines at the margins.

2.3 Design considerations for AMB control circuits

To operate an AMB a controller is necessary because of the "anti-spring behaviour" that is innate in the uncontrolled bearing. Only the one-dimensional case is explained extensively, but this is sufficient to show most of the effects at low speed.

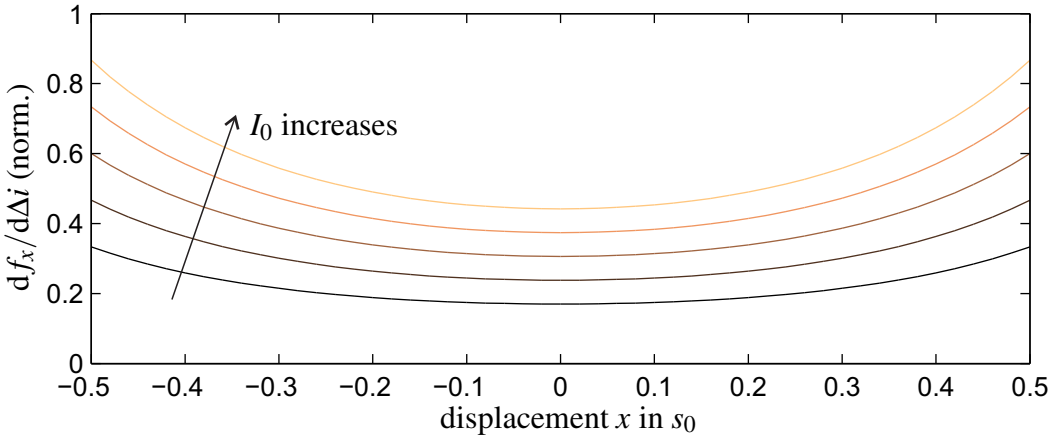

Figure 2.5: Force-current-factor plotted against the rotor displacement x in multiples of s_0. The contour lines show the graph for different values of I_0 ($0.1 \sim 0.5\cdot$ max. current)

2.3.1 One dimensional stiffness and damping design

In section 2.2.3 it was shown that a constant factor between bearing force and displacement, respectively between force and current is a reasonable linearisation around the operating point if only small deviations from the air gap centre occur and if the bias current is high.

In order to stabilize the system a controller with phase lead like PD, $\mathrm{PD_{T1}}$ is necessary. This can be shown by equating the unstable system to a bearing model with normal stiffness and damping [10]: If the inertia of the rotor is represented by the mass m and the influence of the environment is summarized in the force f_{ext}, the force equilibrium becomes:

$$m\ddot{x} = c_x \cdot x + c_{\mathrm{i}} \cdot \Delta i + f_{\mathrm{ext}}. \tag{2.9}$$

$c_x \cdot x$ is the inherent force of the two opposing coils with bias current I_0, see section 2.2 and figure 2.3. The transfer function of the unstable system in the Laplace domain with

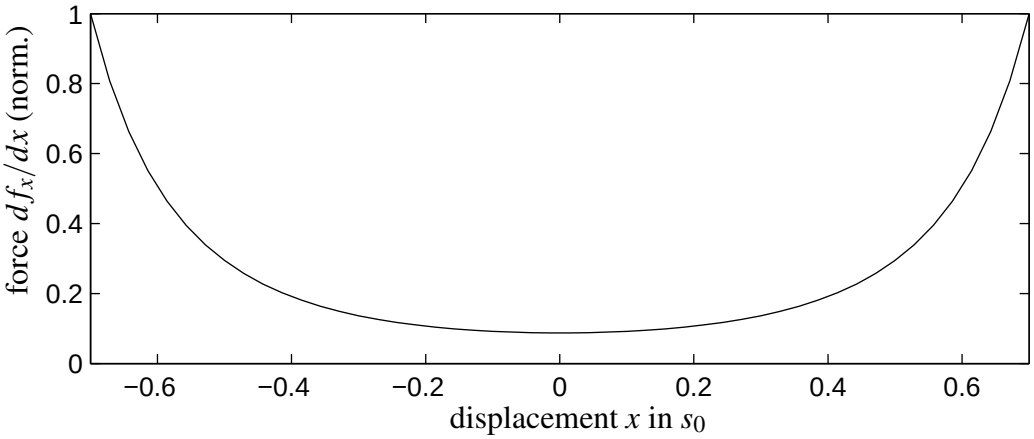

Figure 2.6: Inherent stiffness c_x for the case of two opposing coils. The abscissa is scaled to multiples of s_0.

the Laplace-variable s is [92]:

$$G_{\text{Plant}}(s) = \frac{X(s)}{\Delta I(s)} = \frac{c_{\text{i}}}{ms^2 - c_x}. \tag{2.10}$$

Equation (2.9) is equated with the desired stiffness c_{aim} and damping d_{aim} characteristic:

$$m\ddot{x} = c_x \cdot x + c_{\text{i}} \cdot \Delta i + f_{\text{ext}} = -c_{\text{aim}} \cdot x - d_{\text{aim}} \cdot \dot{x} + f_{\text{ext}}. \tag{2.11}$$

The equation can be resolved for Δi with

$$\Delta i = \frac{1}{c_{\text{i}}} \left((-c_x - c_{\text{aim}})x - d_{\text{aim}}\dot{x} \right). \tag{2.12}$$

$c_{\text{aim}}, d_{\text{aim}}$ and c_x are all positive constants. A PD controller with a reference signal of 0 results. The desired characteristic can only be implemented if both values c_x and c_{i} are exactly known and in any case they change as the rotor departs from the operating point,

as shown in section 2.2. The range of c_{aim} and d_{aim} is restricted, see next section [10, 128].

If deflections close to the air gap width occur, this linear approximation has limitations. Non-linear control strategies have been described [120] as well as procedures to measure or calculate the non-linearities of the force-field and to compensate for them [46, 45, 88, 91, 41]. Typically a linear control outputs actuator forces rather than currents and based on look-up tables or formulas the currents are derived to create the desired forces. This is, however, no remedy to avoid the bias current, because the controllability still depends on the current-force slope [41].

Control strategies with reduced bias current have been described for energy sensitive applications [79, 50]. Also, the eddy currents can be reduced this way [115]. Such a compromise is the "partial bias control" [105], p. 2, which means a small bias current ($I_0 = 0.1 I_{\text{max}}$) and non-linearity compensation. With this small bias current a higher positioning accuracy is achieved than without any bias current [105].

2.3.2 Stability limits and possible values for stiffness and damping

There are different factors that restrict the choice of the quantities for c_{aim} and d_{aim}. If the desired stiffness is chosen too small, uncertainties in the current gain and the inherent stiffness c_x become more significant and the control current may not suffice to overcome the bias field [10].

The upper stiffness limit is more difficult to predict and very important in the given application. This limit is determined by many factors like non-linearities (section 2.2.3), sensor noise at high frequencies, the inductance of the coils, which forbids infinitely fast current changes and the power limits of the amplifiers [91, 10].

An intuitively accessible explanation can be made over the bandwidth: Flotor mass and bearing stiffness together set the frequencies of the rigid body modes. The higher

the stiffness, the higher are these frequencies. The servo bandwidth of the control must be above the rigid body modes and anything that limits the bandwidth also limits the achievable stiffness. The bandwidth should not significantly exceed one-third of the first flexible mode, thus bending modes of shaft and support structure limit the stiffness. Delay times in the signal path limit the servo bandwidth because at high frequencies they cease the phase lead and thereby they also limit the stiffness [50, 81]. Delay times mainly result from the limited amplifier and sensor bandwidth and from the sampling delay of the controller. Typically, the delay time equals one or two sampling time delays [10].

The higher the stiffness, the smaller is the permissible range for the damping that leads to stable operation. This phenomenon can also be elucidated by the signal delay. In [92] the PD controller from section 2.3.1 is modelled as a PD_{T1}-controller to incorporate the sampling time delay:

$$G_{\mathrm{PD}}(s) = K_{\mathrm{P}} \frac{T_{\mathrm{D}} s + 1}{T_1 s + 1}. \tag{2.13}$$

Together with the system transfer function (2.10) investigations with Hurwitz criterion and root locus are made, which yield a lower border for c_{aim} and for T_{D} with respect to T_1 [92].

Su [113] finds that for a given set of stiffness and damping the maximum admissible time delay for a 1-DOF system is

$$T_{\mathrm{dead}} \ll \min\left(\frac{m}{d_{\mathrm{aim}}}, \frac{d_{\mathrm{aim}}}{c_x + c_{\mathrm{aim}}}\right). \tag{2.14}$$

As to [101], a good choice for the target stiffness is $c_{\mathrm{aim}} = 1 \cdot c_x > 0$ or max. $c_{\mathrm{aim}} = 3 \cdot c_x$, which results in indulgent behaviour. In [81] the recommendation is also $c_{\mathrm{aim}} = 1 \cdot c_x$. There are different rules for the choice of d_{aim}, see [81] for a frequency-domain design.

According to [101] $d_{\mathrm{aim}} = \sqrt{m \cdot c_{\mathrm{aim}}}$ is a good choice. In this case the quotient of slew rate σ and swaying frequency ω of the resulting vibration is $\sigma/\omega = -1/\sqrt{3}$. This quotient should always be in the range $-0.1 \sim -1$ [101]. As to [92] d_{aim} should be close to but smaller than $\sqrt{m \cdot c_{\mathrm{aim}}}$.

In addition to these basic estimates a few further tricks should be considered in the design of hardware and control, although it is more difficult to predict in advance how much they will affect the stability limits:

A method to reduce the noise level of the derivative feedback without introducing a phase delay is a state observer such as the Kalman-filter or Luenberger observer [22]. It predicts the sensor measurement from an internal system model and uses the sensor feedback only to correct this estimate [100]. It can also be used to fuse acceleration and position sensors to reduce the effective sensor noise for the AMB control [95].

In applications with high rotational velocities cross-couplings between the individual degrees of freedom due to gyroscopic effects should be counteracted. This justifies centralized control [92] or alternatively decentralized control with disturbance observer [91].

There are more advanced attempts to deal with flexible modes than just to reduce the stiffness especially as the load sometimes dictates a minimum stiffness. One way is to flatten peaks in the frequency domain with notch filters in the sensor path but this approach does not always help and it is difficult to realize if conditions change over the life time [11, 51]. Another way is the tilt control introduced by Okada [89], which detects and actively dampens the inclination of the shaft in the bearing points. These inclinations are related to the bending modes. A third way works if the frequencies of natural vibrations are known *a priori*. Then the sensor signals can be decomposed and the discrete frequencies are attenuated individually to some degree [18].

If a bending node coincides with either a sensor or an actuator, the mode is not observ-

able or not controllable, respectively [11]. Also, it must be avoided in the hardware design state that bending nodes fall between non-collocated position sensors[5] and actuators. The corresponding nodes are excited by the control rather than damped [35].

2.3.3 Analysis of the stiffness as a function of the frequency

If the reference signal is not 0 to centre the rotor as assumed in section 2.3.1 but any small value x_{ref}, then the control law must be adapted to support reference signal tracking [41]. In general this is only as accurate as the system parameters like c_{i} and c_x can be determined. In order to reduce the remaining control offset and also to improve the rejection of low-frequency disturbances integrating feedback is added to the control law and a PID control with the transfer function $G_{\text{PID}}(s) = K_{\text{P}}\left(1 + \frac{1}{T_{\text{I}}s} + T_{\text{D}}s\right)$ results.

In [122] the dynamic stiffness of an AMB with PID control is calculated as a function of the frequency. The transfer function from the disturbing force $F_{\text{ext}}(s)$ to the position $X(s)$ with $X_{\text{ref}}(s) = 0$ is the dynamic compliance, see figure 2.7 and equation (2.10). The reciprocal value is the dynamic or complex stiffness [122]:

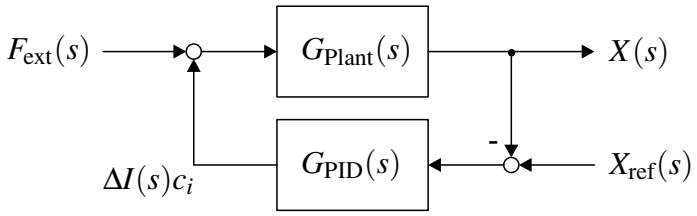

Figure 2.7: Active magnetic bearing $G_{\text{Plant}}(s)$ with PID control $G_{\text{PID}}(s)$ in a block diagram

$$\frac{F_{\text{ext}}(s)}{X(s)} = \frac{ms^3 - c_x s + c_{\text{i}} K_{\text{P}}(s + \frac{1}{T_{\text{I}}} + T_{\text{D}}s^2)}{c_{\text{i}} s}. \tag{2.15}$$

The amplitude frequency response declines at low frequencies because of the s in the

[5]Non-collocated means the sensor is not in the same axial position as the actuator [10, 11].

denominator and after the three zeros it rises again. In [122] it is therefore compared to a bathtub, that means a function with a minimum and ascends on both sides. Practically speaking, the stiffness increases at high frequencies because of the high forces necessary to move the inertia of the rotor. As a result, the stiffness resulting from section 2.3.1 is the minimum stiffness over the frequency range and depending on the frequency of F_{ext} the dynamic stiffness can be higher [122].

2.4 Position sensors for magnetic bearings

The accuracy of a magnetic bearing is primarily determined by the signal quality of the position sensors. The asynchronous error of the AMB can only be low if the sensor resolution is a small number [10, 110, 115, 13, 94]. For the sensor resolution statement it is practical to measure the sample standard deviation σ of the noise and to declare this value as the resolution. Alternatively multiples of the standard deviation or the peak-to-peak value[6] are stated [70]. The number is only valid in combination with the bandwidth for the reason given in section 2.4.5. The four types of position sensors in AMBs are: optical, inductive, capacitive and eddy current transducers [110]. Sensor-less magnetic bearings have been investigated, too, but their strength is not the high accuracy [90]. This section briefly explains the four techniques and gives examples of achievable performance values.

2.4.1 Eddy current sensors

An eddy current sensor consists of a primary coil around an open, non-ferrous core that is supplied with an AC voltage of $\approx 1\,\text{MHz}$. An alternating magnetic field is induced in

[6] Peak-to-peak is not the preferred option because the value is higher if the recording time is longer. To minimize this effect Fleming recommends 100 s acquisition time, which is hardly practical [32].

the conductive surface of the target, causing eddy currents to circulate in the target like in a short circuited secondary transformer coil. Depending on the measured distance both the amplitude and the phase of the current in the primary coil are affected in return and represent the position information [13, 81].

Eddy current sensors have a limited full-scale range to resolution ratio, also called dynamic range and they have temperature drift. In magnetic bearings disturbances can occur when the bearings are driven by switching power amplifiers, especially if the switching frequencies are close to the modulation frequency of the sensors. When the sensors are mounted to close together and the oscillators are not synchronized, mutual interference occurs [78]. A major cause of disturbance in the application of magnetic bearings is related to inhomogeneities in the target material. As soon as the shaft rotates, material impurities and micro cracks with varying conductivity lead to false movement detections ("electrical noise") [10, 87, 81, 70]. In control loops with very high update rate the phase lag of the eddy current sensors deteriorates the performance [60].

Companies for eddy current sensors are Micro-Epsilon [78], Lion Precision, Meggitt, AEC Applied Electronics Corporation and others [32]. An example of a high performance eddy current sensor system is the ECL150 from Lion Precision with 1.25 mm range and 140 nm RMS resolution at 10 kHz on a nonferrous material. It has a bandwidth of 15 kHz, 0.25 % full-scale non-linearity and a temperature drift of 0.04 % full-scale per K. It is available for approximately £1,300 per channel [70]. Other eddy current sensors have comparable characteristics. The range is dictated by the air gap of the magnetic bearing and the mounting tolerances. Two eddy current probes would be operated differentially as opposing sensors, ie. two sensors for each DOF. With five DOF this is a considerable expense.

2.4.2 Capacitive sensors

A capacitive sensor determines the capacitance between the sensor and the target that changes with the distance. Again, a differential arrangement in which the target is in the middle is common and improves the linearity. Limitations of capacitive sensors are the crosstalk between the sensors, thermal effects and changes in the dielectric due to humidity and contamination. For their use in AMBs it is important to note that the electrostatic field is disturbed by external electric fields and that a curved sensor target degrades the linearity [32].

Capacitive sensors are favourable for small distances because their noise is approximately proportional to the distance squared [32] and sensors for wider stand-off, as needed in this application, have large housing diameters - a problem with round shafts [108]. For most sensors the target needs to be grounded with special, conductive brushes. Arrangements with two concentric electrodes separated by a guard ring for non-grounded targets have been described, but the capacity is reduced to one-fourth by this means and the working distance must be even smaller [81, 78]. Best results are achieved with grounded targets [78].

Capacitive sensors don't detect target material inhomogeneities as much as eddy current sensors, but they also rely on the form and smoothness perfection of one single surface in a small point [70]. In AMBs there are approaches to replace the probe type capacitive sensors by cylindrical or plate-type sensor shapes, which provide averaging over a wider target surface area to improve the resolution [52, 104]. None of these extensions shows a better resolution under good conditions[7] than commercially available capacitive sensors.

Again the specifications of a high quality sensor from Lion Precision shall be given,

[7] Good conditions means, the rotor is not deliberately designed to have imperfections.

which would be suitable for the given magnetic bearing design: The P016-6032 probe with $1,250\,\mu m$ full-scale range and 20 nm RMS resolution at 10 kHz has a bandwidth of 15 kHz and 0.2 % full-scale non-linearity. The temperature drift is 0.04 % full-scale per K and the price is £3,163 per channel according to a quote for ten sensors from Lion Precision [70]. Quotations from other companies also confirm that capacitive sensors are even more expensive than eddy current sensors.

2.4.3 Inductive sensors

Inductive position sensors work on the basis that the self-inductance of a coil changes if the magnetic circuit reluctance is altered. The rotor is part of this magnetic circuit and the air gap length varies with the displacement to the rotor. In contrast to eddy-current sensors inductive sensors require a soft-magnetic target material and the core of the coil is a ferrous material. Inductive sensors are not as sensitive to disturbing magnetic fields as the above sensors, but switched power amplifiers may interfere if their frequencies are close to the sensors' modulation frequency. The iron hysteresis is a drawback. Resolutions are 10 to 1 µm [32, 10].

2.4.4 Electro-optical sensors

Before the above sensors were introduced for magnetic bearings, electro-optical sensors were more in vogue than today. Because of the higher linearity and sensitivity of the other three sensors, optical sensors are today only found in a few magnetic bearings. In these application they are favoured because of their immunity against magnetic fields, their high bandwidth and their low price [110]. "Electro-optical sensor" is a collective term for a number of operation principles: The shadow line of the shaft can be located by charge-coupled device (CCD) sensors, the irradiance of a light beam can be modulated by

partial interception, or the position of a laser spot is detected by a position sensitive device (PSD) [110, 34]. Sridharan reports 1 µm resolution at standstill with partial interception. The resolution of CCD based sensors is limited by diffraction [10].

Yet another principle is the optical proximity detector, a device consisting of a light emitting diode (LED) and a photo-transistor next to it. LED and photo-transistor are separated by a wall so that the photo-transistor receives no light. As soon as the reflective magnetic bearing shaft approaches the device, the LED light is reflected at the shaft and reaches the photo-transistor. Over a certain range of short distances the measured irradiance increases with the distance. At wider offset it is exactly the other way round, albeit with a less steep slope. The accuracy is limited by the cleanliness of the LED current, the ageing of the LED, variations in the target's reflectivity, ambient light and noise in the detector [81].

2.4.5 Interplay bandwidth - resolution

The challenge of contact-less position measurement with high resolution and high sampling rate at the same time intensifies in active magnetic bearings with sampling rates of 5 to 20 kHz [69, 98, 4, 41], see also section 3.4.2. Fleming [32] explains this problem as follows: Noise is a mean-free random process $\chi(t)$ with the power spectral density

$$S_\chi(f) = 2 \cdot \mathrm{E}\left[\frac{1}{T}\left|\mathrm{F}_T\left\{\chi(t)\right\}\right|^2\right]. \tag{2.16}$$

F_T denotes the Fourier transform over a long time T and E is the expectation operand.

The power spectral density represents the noise power distribution across the frequency spectrum (unit for example V^2/Hz). Position sensors have a noise characteristic

of the form

$$S(f) = A\frac{f_{\mathrm{nc}}}{|f|} + A. \tag{2.17}$$

Characteristic is the $1/f$ pink noise component[8] with corner frequency f_{nc} and the constant thermal noise with power spectral density A. The standard diviation σ is the square root of the integral over the measured bandwidth f_l to f_h:

$$\sigma = \sqrt{\int_{f_l}^{f_h} A\frac{f_{\mathrm{nc}}}{|f|} + A\mathrm{d}f}. \tag{2.18}$$

Solving the integral leads to

$$\sigma = \sqrt{A f_{\mathrm{nc}} \cdot \ln\frac{f_h}{f_l} + A k_e (f_h - f_l)}. \tag{2.19}$$

Typically, the lower frequency f_l is not zero for noise measurements but 0.01 or 0.1 Hz to exclude the effect of drift and f_{nc} is 10 Hz. k_e accounts for the low-pass filter that limits the bandwidth and it is 1.57 for a first order linear filter. As a result the RMS noise of the mean-free signal, which equals the standard deviation, is approximately proportional to the square root of the low-pass filter cut-off frequency f_h [32].

That is the reason why the resolution was stated together with a bandwidth in the above sections. Eddy current sensors and capacitive sensors with short stroke have resolutions of a few nanometres if they are sampled at 1 or 10 Hz [70], but not at 10 kHz sampling rate and appropriate stroke.

[8] This is excess noise, also called flicker noise caused by imperfect contact between two conductors and thereby fluctuating conductivity [50].

2.5 Precision magnetic bearings

In AMB applications that are optimized for high precision, which is only rarely the main concern, different aspects play a role in achieving this aim: The phase lead characteristic of the high bandwidth control, which is inevitable to stabilize the system, amplifies high frequency noise from the sensors. An intrinsically stable system can be controlled without derivative feedback, which makes it more precise [17]. Rotating machinery has to deal with periodic disturbances that simply don't exist in linear position controls like linear motors. The challenge is to hold the rotor in a constant position as it rotates with conditions changing. Only very few rotational AMBs with nanometre accuracy exist and in industrial applications orbits are not better than 10 or 20 µm [105, 10].

Among the main periodic disturbances are run-out errors along the shaft, mass unbalance and sensor target inhomogeneities [102, 18, 6]. Run-out errors are also referred to as magnetic offset [41] or magnetic run-out [60]. Because of the limited stiffness of magnetic bearings and their characteristic displacement-force relationship external forces have much impact. Methods to counteract periodic disturbances have been studied excessively, albeit more often with the aim of high speed stability than high accuracy of axis of rotation at low speed [102].

In linear magnetic bearings the situation is different because some of the disturbances don't exist. Consequently, there are linear bearings with high stationary accuracy. Below, examples of both types are cited.

Kim and Kim simulate the effect of imperfections in the sensor target surface, misalignment errors and inclinations of the thrust bearing plate [57]. According to the simulations these three factors have the greatest influence on the error motion. Setiawan et al. detect the sensor target surface run-out including higher harmonics and compensate it automatically. Mass unbalance is also considered [102].

An example of a nanometre accuracy radial AMB is the one described in [105]. The vertical spindle is supported by axial air bearings and only the two horizontal translations are controlled magnetically. The iron material for stator and rotor is expensive Ni-Fe with high linearity and high initial permeability. The capacitive sensors with 15 nm resolution have a measuring range of 200 µm. Linear drives are used instead of switching amplifiers. In experiments 3σ positioning accuracies of less than 40 nm are demonstrated for up to 1,500 rpm. As a further improvement the periodic run-out caused by unbalance at high rotational speed is reduced by means of active unbalance control, called repetitive control [69]. In [68] the algorithm for rotation about the centre line is augmented to work with spindles whose geometrical centre line is not defined by the sensor target surfaces. Also, instead of the inductive motor, compressed air accelerates the rotor to eliminate the ripple forces. In [126] the results of the various methods applied to this magnetic bearing are compared. Especially at high speeds the improvement of the combined repetitive control is obvious. At 2,880 rpm the 3σ positioning accuracy is reduced from 301.2 nm to 21.9 nm.

The test rig is an example of a very accurate radial bearing but not all degrees of freedom are levitated magnetically and the rotor mass of 3.29 kg is less than the printing roller mass. A linear low-noise amplifier may not be economical for a magnetic bearing with high load capacity and high load. These are important differences to the magnetic bearing in the roll-to-roll machine. See [60] and [50] for two more examples of rotary magnetic bearings with nm position uncertainty achieved with low rotor mass and linear amplifiers.

Petzold describes the design and commissioning of a rotary magnetic bearing system with higher spindle mass, approximately 1,900 kg. The eddy current sensors have a nominal resolution of 200 nm at a range of 2 mm. Without rotation the positioning noise is approximately ± 3 µm [91]. This is an example of a high load magnetic bearing where the

positioning accuracy for very slow rotations is important. In [100] the positioning accuracy of an AMB is improved from a bit more than 2 μm peak-to-peak to approximately 1 μm peak-to-peak by means of extended Kalman filter. The two test rigs have a rotor mass of 250 kg and 25 kg, respectively. With PID_{T1} control only, the accuracy is limited by sensor noise at high frequencies [100]. Approximately 1 μm peak-to-peak error motion of a radial magnetic bearing and a bit more in axial direction are demonstrated at standstill in [43]. This seems to be a better result, but it must be said that the rotor mass is only 0.35 kg.

Precise position tracking with magnetic bearings requires either feed-forward in combination with PID control or particularly high bandwidth PID control. Grochmal and Lynch [41] demonstrate tracking control of a radial bearing with 50 and 80 μm amplitude of the sinusoidal reference signal at 10 Hz. ±3 μm accuracy is achieved for a non-rotating shaft and at 14,000 rpm deviations from the reference of 20 to 30 μm occur. The rotor mass is 0.98 kg [41]. In [43] tracking control on micrometer level at 1 Hz is implemented for a radial magnetic bearing with high bandwidth. The reference signal amplitude is 30 μm and the rotor mass is 0.35 kg [43].

For a rotor with 8.34 kg mass tracking control in radial direction is incorporated by Lee et al., as already cited above to compensate for tool axis misalignment errors. In addition to the stabilizing PD-control a feed-forward control is built based on identified system parameters. At 2,000 rpm and approximately 60 μm run-out a following error of ±3.3 μm remains [64]. The diamond turning lathe with a magnetically levitated spindle in [56] is designed to perform radial compensation movements in the range of ±100 μm, but no active compensation of errors is actually presented in the paper [56].

Very high precision levels for levitation in constant position have been demonstrated for linear bearings at the University of North Carolina at Charlotte [47]. Three capacitive sensors provide vertical position feedback and interferometers measure the horizontal

position. The vertical positioning noise is less than 2.2 nm (3σ) and 0.6 nm (3σ) noise in horizontal direction is achieved with linear motors. For disturbance rejection and against mechanical coupling of the axes the stage is floating in oil. A Zerodur metrology frame is mounted independent of the main frame [47].

2.6 Concluding remarks

The precision of the printing machine axes has been identified as a key optimisation target to make flexible electronics printable with small feature sizes. High quality fluid-film bearings are therefore even more suitable than commercially available printing machine rolling element bearings. The comparison of bearing technologies suggests that oil lubricated bearings are the better fluid film bearings than air bearings because the latter have even tighter alignment requirements and their specific load capacity is lower. Also, air bearings have low damping and are costly to manufacture. But as soon as the entire machine is considered, neither of the passive bearings can meet the accuracy requirements of the grouped rollers in the machine. It can be anticipated that the positioning of the surfaces of interest would not be accurate enough although the fluid-film bearing itself defines its rotor precisely. Reasons for that have been given.

Active magnetic bearings are a promising improvement over passive bearings because they can compensate for imperfections of the spindle and the entire assembly. Tunable stiffness and damping expand the opportunities to tailor the bearings at run-time. For static forces the stiffness is infinite. As a positive side-effect there are reasons to believe that maintenance and alignment efforts are reduced with AMBs.

Nevertheless, printing machines are not a typical application of AMBs and the reasons may be the low stiffness at medium frequencies and the unavoidable positioning noise. A number of factors limit the stiffness and they are all well known and have been studied

excessively. It will still be necessary to determine the actually achievable stiffness for the R2R magnetic bearing. The following issues can be inferred from the literature review that could limit the stiffness of the printing roller levitation or complicate its design and control:

- The necessity to move the rotor around actively may lead to problems with non-linearities compared to applications where it is merrily centred (section 2.2.3).
- The horizontal operation of a heavy spindle is a problem. Unless the bearing's load capacity is very high, non-linearities need to be considered.
- With a hollow printing roller of limited rigidity bending modes might interfere with the bandwidth that results from the desired stiffness.
- Although it is important to locate the sensors close to the actuators one may be inclined to measure the position of the roller directly because of run-out errors. This would cause problems with bending nodes between sensors and actuators.

The accuracy limitation of AMBs has been addressed in sections 2.4 and 2.5. In rotating magnetic bearings countermeasures are necessary to eliminate periodic disturbances. Light rotors can be levitated very precisely as shown by the references. In the given application with low speed of rotation it can be anticipated that algorithms for rejection of periodic disturbances will achieve satisfactory results or that they are not even necessary.

Unfortunately, the positioning uncertainty seems to be a function of the rotor mass and the sensor range. With heavy rotors there is always a non-repeatable error motion of a few micrometres, even if the rotor is not rotating and no disturbing forces are present. This is related to various tricks applied in small, precise magnetic bearings as explained above, for instance, larger magnetic bearings must be driven by switching power amplifiers that disturb the sensors. Large AMBs also have sensors with wide stroke to account for the

wider air gap. A magnetic bearing of the required size would hardly be precise enough to meet the specifications.

Regarding the gap sensors, capacitive and eddy current sensors are the sublime gap sensors, but in contrast to optical sensors they are prone to field disturbances. At the high sampling rate in magnetic bearings especially eddy current sensors may have too much noise and they introduce a phase lag. Capacitive sensors are available with higher resolution, but they are expensive and their measurement principle is affected by the electromagnetic fields in active magnetic bearings. Regarding the position sensors there seems to be no ideal solution for large magnetic bearings with high bandwidth and high accuracy over a wide stroke of movement.

Another aspect that will become important is the tracking control of radial magnetic bearings. There are not many publications that deal with this problem but some examples have been cited.

The situation is clearer for the bearing dimensioning and the choice of materials. The load capacity can be related to the approximate bearing size and the current starting with the calculations in section 2.2.2. Heteropolar radial bearings are used in the majority of research platforms and their characteristics are well known. It seems that the dimensioning of the actuators is straightforward and that no innovative design is required.

2.7 Aim and objectives

The aim of this master by research study is to investigate the applicability of active magnetic bearings to high precision R2R production.

In section 1.1 the purposed long-term research has been described and justified. Unresolved questions and potential problems have been identified in the literature review and summarized in section 2.6. Within the scope of this research study the following objec-

tives shall contribute to the overlying aim and push the use of active magnetic bearings in printing machines:

- Justification of magnetic bearings as a potential improvement of high precision R2R printing machines
- Description of an innovative radial position sensor for magnetic bearings based on linear optical encoders
- Definition and experimental comparison of different techniques to create amplitude gratings for ordinary optical encoders by micro-machining
- Experimental validation of the position sensor and characterisation of chosen aspects
- Design, assembly and commissioning of a new magnetic bearing test rig
- Performance demonstration of the position sensor in closed loop control of a rotary magnetic bearing
- Design of a magnetic bearing spindle for R2R production systems including optical encoders for position measurement, discussion of associated limitations

Chapter 3

Magnetic bearing design work

In this chapter the design of a magnetic bearing for the printing roller is approached in some initial steps. These include the dimensioning of the AMB, the power amplifiers, theoretical considerations on optical, linear encoders for the position measurement and the choice of a suitable control hardware as well as reflections on discarded options. A first spindle design of the R2R AMB is also provided.

3.1 Bearing dimensioning

The next step is to verify the feasibility of the target specifications regarding force-size relation and to determine further characteristics. In section 2.2.2 the force has been calculated in terms of the rotor displacement and current. To account for requirement 50 from table 1.1 the radial bearing clearance is set to 300 µm. The air gap length should be about two times this value, $s_0 = 600\,\mu\text{m}$, because of the structural compliance [10]. The same values have been chosen for the axial bearing.

The required size of the AMB is determined by the load capacity in combination with the iron saturation. If the flux density B was raised beyond the saturation point B_{sat}, much

more electric power would be required. A material with sufficient saturation polarisation, low eddy current loss and affordable price is Silicon-iron [39]. Non-grain-oriented M290-50A is a compromise between energy loss and high saturation polarisation. It has a lamination thickness of 0.5 mm, core losses of 1.14 W/kg at 1 T and 50 Hz and an induction of $B_{\mathrm{sat}} = 1.58\,\mathrm{T}$ at $2,500\,\mathrm{A/m}$ [83][1].

In order to calculate the radial force at B_{sat}, equation (2.4) is taken as a starting point. With

$$\Theta = ni = \Phi R_{\mathrm{m}} = BA_{\mathrm{r}}\left(R_{\mathrm{m,air}} + R_{\mathrm{m,Fe}}\right) \tag{3.1}$$

the magnetomotive force $\Theta = ni$ can be replaced in equation (2.4). This eventually leads to the easy form

$$f_{x1} = \frac{1}{\mu_0} B^2 A_{\mathrm{r}} \cos\left(\frac{\pi}{8}\right), \tag{3.2}$$

which allows to calculate the force from the flux density.

The area A_{r} equals cl_{r}, which can approximately be expressed as $A_{\mathrm{r}} \approx \frac{1}{16}\pi d_{\mathrm{r}} l_{\mathrm{r}}$. Because of the space for the coils only half of the circumference is available for iron [10]. Refer to pictures 2.2 and 2.3 for geometric constants. With this assumption the force of the radial bearing can be related to the size of the rotor:

$$f_{x1} = \cos\left(\frac{\pi}{8}\right) B^2 \frac{\pi d_{\mathrm{r}} l_{\mathrm{r}}}{16\mu_0}. \tag{3.3}$$

The maximum quotient of force and rotor area $d_{\mathrm{r}} l_{\mathrm{r}}$, which is called the specific load

[1] The guaranteed characteristics differ slightly from manufacturer to manufacturer.

capacity [10], is

$$\frac{f_{x1,max}}{d_r l_r} = \cos\left(\frac{\pi}{8}\right) B_{sat}^2 \frac{\pi}{16\mu_0} = 360\frac{\mathrm{kN}}{\mathrm{m}^2}. \tag{3.4}$$

The cross section area of the radial bearing rotor corresponding to the load capacity of 3 kN is 83 cm^2. The radial bearing stator must have an inner bore suitable for such a rotor, which seems reconcilable with the dimensional requirements at the first glance, but the question of the overall size will be treated in more detail later.

One might be tempted to dimension the magnetic bearing with the aim that its stiffness is the same as that of the hydrostatic bearing. The passive radial stiffness in vertical direction can't be calculated with equation (2.8), because the bearings have to carry the mass m of approximately 200 kg, so the control current is not 0. With only one active coil the force-displacement slope can be calculated from equation (2.4):

$$\frac{\mathrm{d}f_{x1}}{\mathrm{d}x} = \frac{4(ni)^2(\cos(\frac{\pi}{8}))^2 A_r \mu_0}{\left(2s_0 - 2\cos(\frac{\pi}{8})x + \frac{l_{Fe}}{\mu_{rFe}}\right)^3}. \tag{3.5}$$

Assuming a static load of $\frac{1}{2}mg$ the expression for the force in equation (3.5) can be replaced:

$$\left.\frac{\mathrm{d}f_{x1}}{\mathrm{d}x}\right|_{OP} = \frac{1}{2}mg\frac{4\cos(\frac{\pi}{8})}{2s_0 - 2\cos(\frac{\pi}{8})\cdot 0 + \frac{l_{Fe}}{\mu_{rFe}}} \approx 2.9\,\frac{\mathrm{N}}{\mu\mathrm{m}}. \tag{3.6}$$

μ_{rFe} is set to $5,000$ at this undersaturated point and $l_{Fe} \approx 0.3$. The stiffness can be increased if the lower magnet is also energized. This additional force $f_{x,add}$ increases the force of the upper magnet in the operating point by the same amount, because the force

equilibrium is still maintained. The resulting stiffness is:

$$c_x = \frac{\frac{1}{2}mg + 2f_{x,\text{add}}}{\frac{1}{2}mg} \cdot 2.9\,\frac{\text{N}}{\mu\text{m}} = \left(1 + 4\frac{f_{x,\text{add}}}{mg}\right) \cdot 2.9\,\frac{\text{N}}{\mu\text{m}}. \tag{3.7}$$

If this negative stiffness had to be as high as the stiffness of the hydrostatic radial bearing ($100\,\text{N}/\mu\text{m}$, as measured in [129]) an additional force of $f_{x,\text{add}} = 16.4\,\text{kN}$ would be required. With a load capacity of two times this value, the rotor area had to be $(d_\text{r} l_\text{r}) = 912\,\text{cm}^2$, for example $l_\text{r} = 350\,\text{mm}$ and $d_\text{r} = 260\,\text{mm}$. The bearing had to be bigger than allowed by the requirements in table 1.1. In figure 3.1 the anticipated size of such a magnetic bearing is shown. It is intuitively too big and also too expensive. The company MECOS Traxler AG in Switzerland estimates a price of CHF$250,000 \approx$ £$166,000$ for one radial bearing.

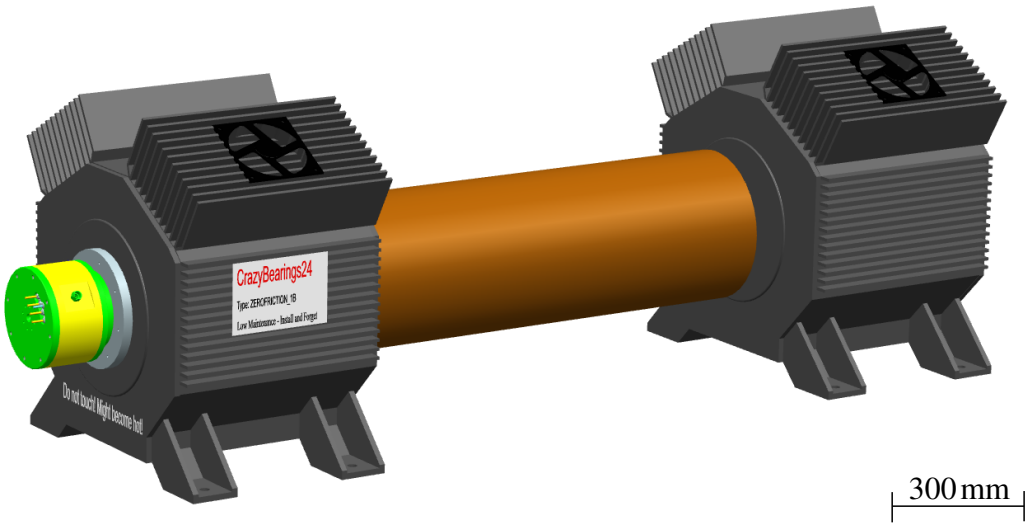

Figure 3.1: Anticipated outline of magnetic bearings with the same minimum stiffness as the hydrostatic bearings, shown with the printing roller in between. The bearings have a length of 660 mm.

The conclusion from this thought experiment is that the aim should not be to build

a magnetic bearing with the same stiffness as the hydrostatic bearing. The stiffness at medium frequencies will always be lower. Realistic stiffness values are stated in the next section for the actual product.

3.2 Outsourcing of standard components

A detailed design of the magnetic iron circuits and the electric coils could now be carried out on the basis of the requirements and section 3.1. However, these calculations are state-of-the-art [115, 7] and there are no special requirements that would exclude a standard design. The iron for rotor and stator, the coils and the amplifiers should be outsourced to specialized companies.

The global search for companies that design and manufacture magnetic bearings returned the following results: SKF has operational sites in many countries and it has the longest experience in industrial magnetic bearings [115]. In the USA there are Synchrony ® magnetic bearings, headquartered in Virginia, Airex Corporation in Vermont, Calnetix Technologies in California and Waukesha Bearings in Wisconsin. Foshan Genesis [31], founded in 2012, is the youngest company and it is located in Foshan City, China. German companies are Schaeffler with the brands FAG and INA, Elektrische Automatisierungs- und Antriebstechnik (EAAT) GmbH Chemnitz, LEViTEC in Lahnau and evico GmbH in Dresden. In Switzerland there are the companies Levitronix in Zurich and MECOS Traxler AG in Winterthur.

It can be observed that magnetic bearing companies generally refuse to sell single parts of the mechatronic system and the product always includes amplifiers, sensors, the controller and the cabinet. Only a few companies made offers for a subset of the usual delivery and service, but in the given case with special sensor system, interchangeable control unit and complex spindle and housing design it is impossible to outsource the

entire magnetic bearing design.

To the amplifier requirements, it is important that the current slew rate be as high as possible because the bandwidth for full force amplitude is proportional to the saturation power [115]. Thus the DC intermediate circuit voltage should be as high as possible and the amplifier should support two-quadrant operation, ie. both signs of the output voltage [41]. Negative output currents are not required, because the direction of the force is the same, but [53] still argues for four-quadrant power stages to improve the dynamic performance[2]. The PWM duty-cycle of a switching type amplifier is either proportional to the control variable or it is actually controlled based on current measurement to follow the reference signal (transconductance amplifier). The later makes the output current more predictable and linear to the reference signal and it allows more rapid changes [72]. A transconductance amplifier is therefore preferred. Furthermore each amplifier should be able to drive its electromagnetic coil at maximum current.

The most suitable offer for two radial magnetic bearing stators and one axial magnetic bearing stator pair was made by Foshan Genesis [31], see details in table B.1 and figure B.1 in appendix B. The delivery also includes two radial, inductive sensors and the dedicated signal conditioners. Regarding the amplifier the BA30 from Aerotech with integrated feedback current control and four-quadrant operation has been chosen and bought, see table B.2 in appendix B [3].

Almost all the promised magnetic bearing features seem to fulfil the requirements from section 1.2, but the geometrical specifications can only be approved on the basis of the entire housing and rotor design. What is not sufficient is the resolution of the sensors. For the targeted positioning accuracy sensors with finer resolution are required and this set of sensors cannot be used. From equation 2.2 the inductance of one radial

[2]Bidirectional currents are more commonly used in hybrid magnetic bearings. The permanent magnet bias flux adds to control current induced flux that can be positive or negative to stabilize the position [120].

magnetic bearing coil can be estimated: $18\,\mathrm{mH} > 1\,\mathrm{mH}$. The inductance of the axial bearing is approximately $160\,\mathrm{mH} > 1\,\mathrm{mH}$. So, the amplifiers are suitable to drive both coil types and the current capability is sufficient to drive both bearings with maximum force continuously.

From equation (3.7) a radial, vertical stiffness of $c_x = 12.7\,\mathrm{N}/\mu\mathrm{m}$ results, assuming a maximum continuous force of half the load capacity. The radial, horizontal stiffness is $c_y = 15.6\,\mathrm{N}/\mu\mathrm{m}$ and the thrust bearing stiffness is $c_z = 15.5\,\mathrm{N}/\mu\mathrm{m}$, based on the same assumption.

3.3 Sensor system for spindle position measurement

It has been shown in the review of AMB sensors and notorious high precision bearings that the position sensors determine the precision of levitation significantly and that commercially available sensors have critical limitations. The proposed design for the radial sensors is based on linear incremental optical encoders as they are known from machine tools to measure the position of a carriage relative to a slideway. In order to use them as a radial position sensor a special scale has to be made that is not available on the market. This section explains the operation principle of the scale in different types of encoders to allow an estimation of the feasibility to machine a suitable scale.

3.3.1 Encoders based on the imaging scanning principle

A reading or scanning head counts periodic structures on a scale grating while reading head and scale move relative to each other. The irradiance of a light source is modulated by the scale and directed either at photodetectors behind the scale (trasmissive type) or at photodetectors on the same side of the scale as the light source (reflective type) [81].

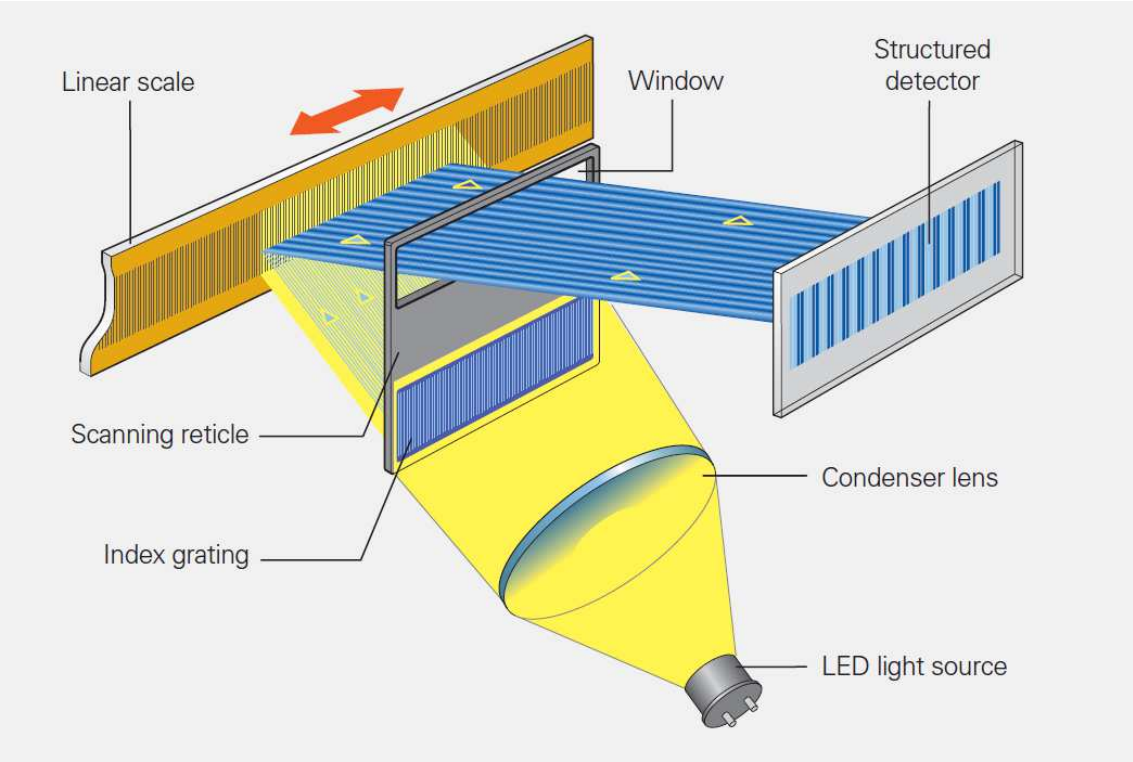

Figure 3.2: Imaging scanning principle with reflective scale and single-field detector, source: Heidenhain [24]

This so called imaging scanning principle is shown in figure 3.2 for a reflective scale. The parallel light emanating from a light source with condensor lens passes through a reticle with index grating and is then reflected by the scale. The index grating has an interchanging pattern of transparent and absorbent or reflective fringes with a period of p that cast lines of shadow on the scale. The scale has reflective and absorbent lines, too, so that the light is modulated by a relative movement. During a movement of p the light on the measuring standard changes from maximum to minimum and back [24, 30].

With ideally sharp fringes and a point light source the intensity on the detector would follow a triangular pattern. But the light is blurred because of the size of the light source and the reading head is designed in a way that the output signal is close to sinusoidal. Furthermore, the index grating has a slightly different grating period from the scale or it

is tilted a few degrees. Consequently, the irradiance is not homogeneous over the entire sensor area but resembles a moving wave with longer wavelength than the scale graduation but the same frequency. This effect is called Vernier magnification[3] and allows the recognition of speed and direction by CCD sensors in the detector when the scale is moving. Sometimes the moving fringes with magnified grating period are referred to as moiré fringes. The outputs are two differential, harmonic voltage signals for each encoder with 90° phase difference. One period of the output signal represents a movement of p [81, 118].

It is important to note that the reflective lines of the scale must be highly reflective and they must reflect the light in the right direction. Contrast is created on the scale with etching and vacuum evaporation techniques. For the substrate, materials with expansion coefficients close to that of steel or cast iron are often used, e.g. steel, glass or glass-ceramic [118, 24]. The imaging scanning principle is used for grating periods of 10 µm to 200 µm [24]. At these structure sizes diffraction is only a side-effect and short optical paths of the light keep it at a minimum [118, 81, 108].

A reading head communicates the incremental position with sinusoidal current signals, sinusoidal voltage signals, quadrature signals or with digital interfaces. In the case of sinusoidal voltage signals the information is contained in the two 90° phase-shifted, harmonic signals a and b. The amplitude of both signals is A, ideally $A = 0.5\,\mathrm{V}$, $M = 2A = 1\,\mathrm{V}$, see figure 3.5. A high amplitude can only be achieved with high scale contrast, so that the peak-to-peak amplitude M is an important performance indicator. Depending on the exact reference a range of $0.6 \leq M \leq 1.2$ [25] or $0.75 \leq M \leq 1.25$ [24] is rated as acceptable. The signal phase is reconstructed with the function $\alpha = \mathrm{atan2}(a,b)$ [24].

[3]The word Vernier magnification stems from to the French inventor Pierre Vernier (1580 - 1637) [81].

3.3.2 Interferometric encoders

For finer grating periods the imaging scanning principle has two limitations: Diffraction becomes more critical and the mounting tolerances of the reading head become too tight to be practical. Encoders with grating periods of 8 µm, 4 µm and finer operate according to the interferometric principle [24, 30] with diffraction gratings. The gratings modulate the phase of the incident light and the light beam is diffracted into different orders. The diffraction that is inevitable at finer grating periods is utilized to deliberately split the light and the interference of different paths contains the position information. The reflective Heidenhain encoders of interest are equipped with transparent phase grating reticles, respectively reflective phase gratings on the linear scale [81]. Refer to [81] for the exact operation of interferometric encoders.

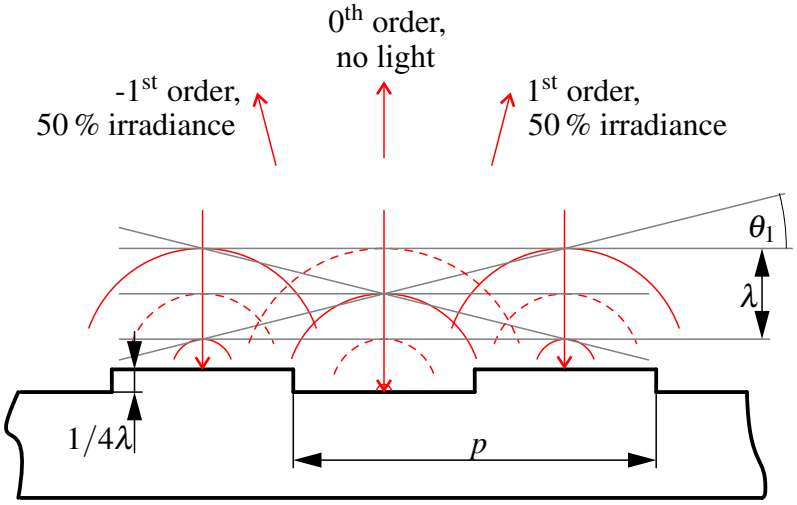

Figure 3.3: Scale for differential encoder with reflective phase grating

Figure 3.3 shows a reflective Lamellar grating that constitutes the scale[4]. The surface has reflective stripes at two alternating heights. When this surface is illuminated with monochromatic light (wavelength λ) in the vertical direction, the light reflected at the top

[4] "Lamellar grating" refers to the rectangular cross section and the equal spacing between upper and lower surface [74].

surface interferes with the light reflected at the bottom. The step height of $1/4\lambda$ cancels the light that would otherwise be reflected back into the light source (0^{th} order) and makes the 1^{st} orders as bright as possible. The constructive and destructive interference is only perfect if the height of the structure is exactly $1/4\lambda$, for example $0.2\,\mu\text{m}$. The grating period p determines the angle of reflection:

$$n\lambda = p\sin(\theta_n). \tag{3.8}$$

The encoder only works with the correct angle θ_1, so that exact depth and width of the structures are both crucial [81].

3.3.3 Radial position measurement with incremental optical encoders

The idea is to make a special scale for the magnetic bearing with concentric, coplanar circles on a disc, see figure 3.4. The encoders count the lines of the round scale as they would otherwise count the lines of a linear scale. In contrast to a rotary encoder the lines are not aligned in radial direction, but each line is a circle. A rotary encoder with four reading heads could measure the radial position, too [75], but it has drawbacks: Firstly, the speed of rotation is limited, even without run-out because counting mistakes must be avoided. Secondly, the accuracy might deteriorate when the shaft rotates quickly, because the output signals change constantly. Thirdly, four position signals have to be fused by the control instead of two, which makes it more costly and the sensor noise adds. With linear encoders and concentric circles the extrapolated line of measurement for each sensor goes through the centre line of the shaft, so that its position can be measured without Abbe offset [81]. The displayed disc should be mounted close to the actuators to avoid errors due to bending modes of the shaft.

The suitability of conventional optical sensors for AMBs has already been discussed

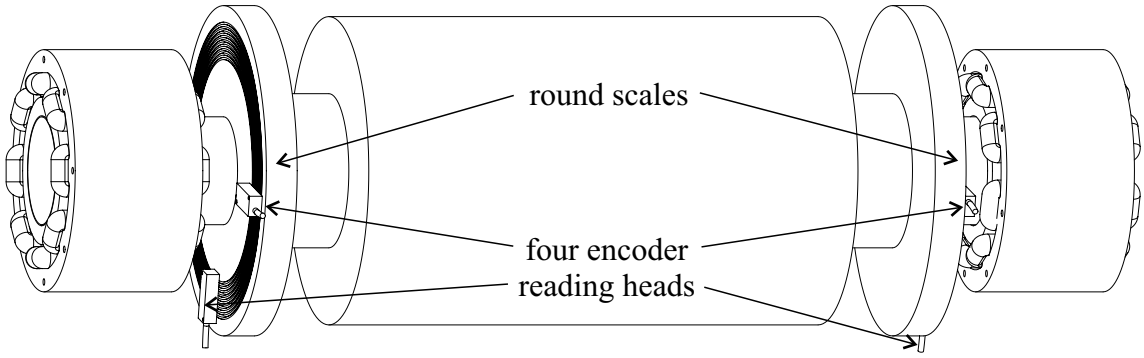

Figure 3.4: Proposed setup for radial spindle position measurement with incremental, optical encoders

in section 2.4.4. The reasons why incremental, optical encoders could have the potential to be better for a high precision magnetic bearing are:

- Signal distortions of the analogue output voltage may have less effect because the span from minimum to maximum output voltage only represents $1/2p$, not the entire measurement range.
- Linear optical encoders have a high accuracy and linearity of up to 5 ppm at 1 m range. That is about 200 times better than capacitive sensors [32].
- Encoders have been widely used in machine tools since the 1950s and they are highly optimized [32]. They are cheaper than gap sensors, see prices below.
- Optical sensors have a high bandwidth, e.g. 400 kHz, see also manufacturers' websites and at the same time a high resolution [110].
- They are not sensitive to external electromagnetic fields that are present in magnetic bearings and interfere with ordinary gap sensors [110, 115]
- The simultaneous evaluation of several square millimetres of scale (14.5 mm^2 for the LIDA 48) provides spacial averaging of statistically distributed scale errors [24,

118].

- The effect of thermal drift is reduced because the scale is separated from the electronics by an air gap.

- Assumption: Thanks to the incremental principle, the range of movement can be wider than with gap sensors while maintaining a high resolution.

It is possible to extend the described arrangement by cutting gratings into the cylindrical surface of the disc, too. This would add the capability to measure the axial position of the spindle, but the mounting tolerance of the reading head would limit the radial range of movement. The distance between reading head and scale is specified and must be kept to a tolerance of $\pm 250\,\mu m$ or $\pm 100\,\mu m$, depending on the exact type [24]. This tolerance always restricts the movement in one direction. The proposed principle is therefore only applicable in applications where either the radial or the axial vibrations are below these tolerances. For the printing roller only radial run-out is supposed to be compensated and fast axial movements are not planned. The axial position measurement would also bring about a high Abbe offset and possibly difficulties to reference the incremental sensors. For these reasons the axial position still has to be measured with for instance capacitive sensors but that could be possible as the range is not wide.

3.3.4 Grating period and scale type

As a next step the grating period in accordance with the scale type (imaging scanning principle or interferometric) is chosen. As explained in section 3.3.2 diffraction grating scales for interferometric encoders are only functional if the structures have the right depth and the right widths. With a grating period of $4\,\mu m$, ie. $2\,\mu m$ width of the grooves and 200 nm depth the dimensions are very small for a turning process [37]. If the grooves

were cut into a flat surface, it would be difficult to maintain a constant depth of 200 nm in spite of thermal spindle growth. Adjusting the depth of a cut more precisely than to 1 µm requires special equipment or test runs to monitor the exact depth [74].

This only leaves encoders based on the imaging scanning principle. There are two exposed linear optical, incremental encoder types from Heidenhain based on the imaging scanning principle: AK LIDA 48 and AK LIDA 28[5]. Their characteristics are summarized in table 3.1 [24].

Table 3.1: Characteristics of two Heidenhain encoder types with imaging scanning principle, table based on information from Heidenhain [24]

Type	Grating p period	Smallest measurable step	Deviations per signal period	Mounting tolerance	Price
LIDA 48	20 µm	0.01 µm or 0.05 µm	±0.2 µm	±100 µm	£315.00
LIDA 28	200 µm	0.5 µm	±2 µm	±250 µm	£195.30

The scale for the LIDA 28 can be machined with less delicate tools and promising results are thus more likely. It also allows the detection of 10 times faster radial movements; the speed limit is exceeded when the relative movement reaches half a signal period per sampling delay or more. Assuming a sampling frequency of 10 kHz this is equivalent to 1,000 mm/s average speed for 0.1 ms in case of 200 µm grating period or 100 mm/s for 20 µm grating period. This limitation, however, is irrelevant because the spindle only moves radially to compensate the roller run-out. According to section 1.2 the ultimately expectable radial speed is $50\,\mu\text{m} \cdot 2\pi \cdot 5\,\text{Hz} = 1.57\,\text{mm/s}$. The effect of high frequency vibrations in the controlled position should be less critical because these have a small stroke.

[5]The last digit represents the way of internal interpolation. Only AK LIDA 48 and AK LIDA 28 output the analogue signals directly and don't interpolate internally. Analogue output signals are needed for the experiments.

Three reasons suggest the use of the LIDA 48. Firstly it has the smaller specified measurement steps, small enough to fulfil the accuracy requirement of the magnetic bearing. Secondly with the ten times smaller grating period more grooves are measured at the same time, which strengthens the spacial averaging effect [118]. Thirdly, noise caught by the signal cable and errors of the analogue circuits and the ADCs are less amplified and have less influence than with 200 µm pitch. This third aspect can be visualized in a calculation:

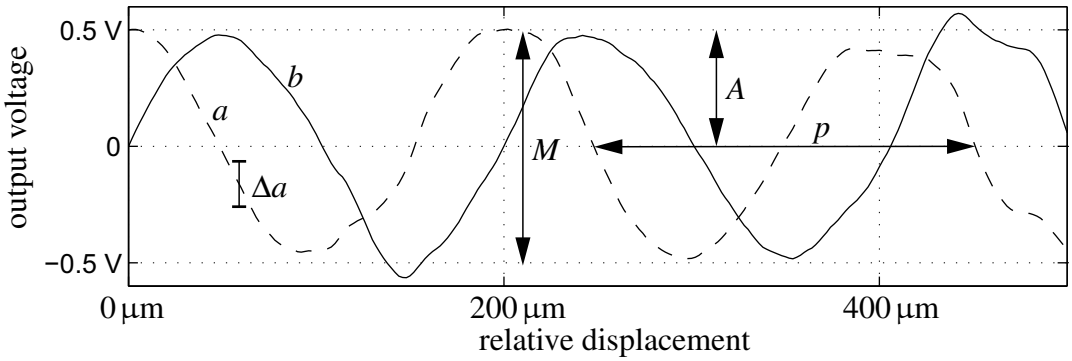

Figure 3.5: Incremental encoder output signals a and b with errors (qualitative figure). The grating period is 200 µm.

Each output signal a and b is to some degree disturbed and distorted, see figure 3.5. In order to calculate the error in the phase α in terms of the voltage errors of a and b, the derivative of $\alpha = \text{atan2}(a,b)$ with respect to a and b is evaluated:

$$\frac{\partial \alpha}{\partial a} = \frac{\partial}{\partial a}\arctan\left(\frac{a}{b}\right) = \frac{b}{a^2+b^2}, \tag{3.9}$$

$$\frac{\partial \alpha}{\partial b} = \frac{\partial}{\partial b}\arctan\left(\frac{a}{b}\right) = \frac{-a}{a^2+b^2}. \tag{3.10}$$

The position error related to the error in a only is

$$\Delta x(\Delta a) = \frac{p}{2\pi} \left.\frac{\partial \alpha}{\partial a}\right|_{\mathrm{OP}} \cdot \Delta a \tag{3.11}$$

and for b respectively.

When both signals together are considered, two cases must be distinguished: The first case deals with the noise propagation from signals a and b to the position noise. Δa and Δb are standard deviations of the noise that leads to the coupled position noise Δx with

$$\Delta x(\Delta a, \Delta b) = \frac{p}{2\pi} \sqrt{\left.\frac{\partial \alpha}{\partial a}\right|_{\mathrm{OP}}^2 \Delta a^2 + \left.\frac{\partial \alpha}{\partial b}\right|_{\mathrm{OP}}^2 \Delta b^2}, \tag{3.12}$$

assuming uncorrelated disturbances [50]. Assuming further that $\Delta a = \Delta b$ and plugging equations (3.9) and (3.10) into (3.12), the resulting noise turns out to be independent of the signal angle:

$$\Delta x(\Delta a = \Delta b) = \frac{p}{2\pi} \frac{\Delta a}{A}. \tag{3.13}$$

Note: $a = \cos(\alpha)A$, $b = \sin(\alpha)A$.

The second case of interest describes the maximum position error resulting from a certain offset in a and b of Δa and Δb respectively. In this case the error influences are added [97]:

$$\Delta x(\Delta a, \Delta b) = \frac{p}{2\pi} \left(\left.\frac{\partial \alpha}{\partial a}\right|_{\mathrm{OP}} \cdot \Delta a + \left.\frac{\partial \alpha}{\partial b}\right|_{\mathrm{OP}} \cdot \Delta b \right). \tag{3.14}$$

When for example Δa equals Δb, then the resulting position deviation

$$\Delta x(\Delta a = \Delta b) = \frac{p}{2\pi} \frac{\Delta a}{A} (\sin \alpha - \cos \alpha) \tag{3.15}$$

is still a function of the signal angle α. The maximums and minimums, both of interest coincide with the bisectrix:

$$\frac{\partial}{\partial\alpha}\left(\frac{\Delta a}{A}(\sin\alpha-\cos\alpha)\right)=\frac{\Delta a}{A}(\sin\alpha+\cos\alpha)\stackrel{!}{=}0\Rightarrow\alpha=z\cdot\pi+\frac{3}{4}\pi. \tag{3.16}$$

with $z\in\mathbb{Z}$. This case is relevant for the distortions caused by non-zero-free signals and for the peak-to-peak error [97]. Both cases show that a smaller signal period reduces the influence of noise from the analogue electronics and the ADC. A high signal amplitude has the same effect.

One disadvantage of a smaller grating period, apart from the difficulties in machining it, is the tight mounting tolerance. Decisive is the tolerance for the distance between reading head and scale as indicated in table 3.1 and the parallelism tolerance. Furthermore, when the curved scale moves radially in the direction perpendicular to the measurement direction of a certain encoder, the reading head sees a rotation of the scale lines. This misalignment is labelled x_c in figure 3.6.

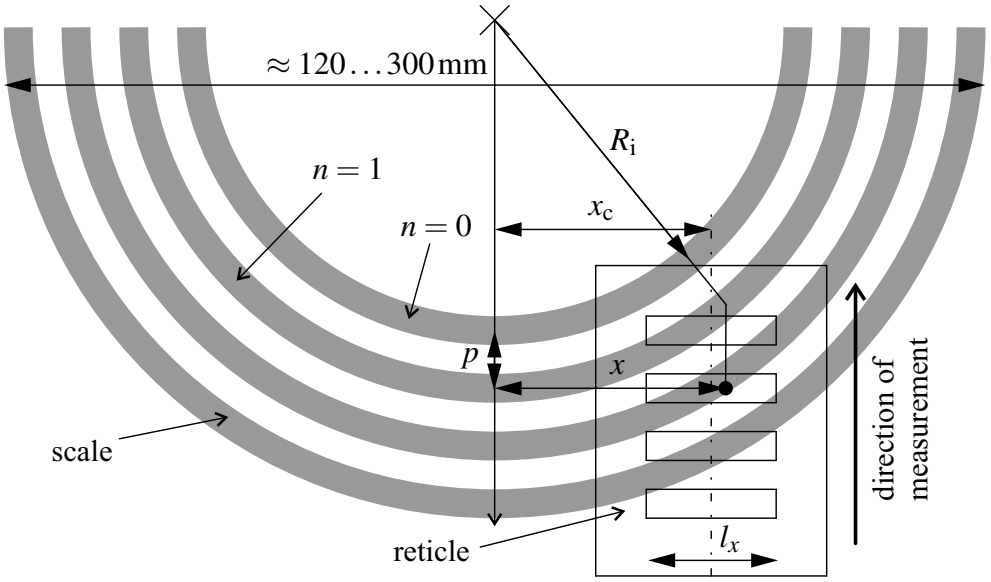

Figure 3.6: Theory of misalignment between scale and reading head reticle

The moiré fringe effect degrades when reticle and scale fringes are rotated against each other, because the contribution of each groove to the output signal is phase-shifted by a different angle. Groove n has approximately the phase $\varphi_n(x)$:

$$\varphi_n(x) = \frac{2\pi}{p}\sqrt{(R_\mathrm{i} + np)^2 - x^2} \tag{3.17}$$

R_i is the radius of the innermost groove that is evaluated. Assuming that m slots[6] with a length of l_x in the reticle contribute equally to the measured output signal, then the voltage amplitude A can be estimated:

$$A = \frac{1}{ml_x}\left|\sum_{n=0}^{m-1}\int_{x_\mathrm{c}-l_x/2}^{x_\mathrm{c}+l_x/2} e^{j\cdot\varphi_n(x)}dx\right| \cdot A_\mathrm{max}. \tag{3.18}$$

This estimate might differ from the reality because the reading head may have additional, unknown features. Especially the number of slots m and the length l_x are unknown so that a precise calculation cannot be made at this point but it is obvious that the correct alignment is more critical for higher numbers of slots and a smaller grating period p. How far the signal amplitude is actually affected by the orthogonal movement should be determined in experiments for both grating periods because this characteristic is important. It limits the measurement range of the radial sensor system. It shall also be mentioned that a false measurement of approximately $R_\mathrm{i} + pm/2 - \varphi_{m/2}(x_\mathrm{c}) \cdot p/(2\pi)$ occurs, but this effect is known from gap sensors in magnetic bearings, too; they also measure a curved target.

[6]For simplicity only four slots and four grooves are shown but in reality the number is higher.

3.4 Controller hardware

For the controller hardware especially powerful equipment is required. The number of analogue and digital interfaces is higher than usual because of the redundant position measurement. At the same time a high sampling rate must be achieved. This section first gives an overview of available systems, without considering the project requirements in detail. Later, these requirements are stated and finally a decision among the most promising candidates is made.

3.4.1 Overview of possible systems

As in any other application the control of a magnetic bearing can be implemented either with analogue or with digital hardware. If the sensor inputs and the control outputs are analogue voltages, an analogue control with very short delay time and low manufacturing cost can be an asset [11]. The first active magnetic bearings were based on analogue controllers with tube amplifier [55]. However, for a research project the lack of interchangeability in a hard-wired electronic circuit would become a problem. Possibilities of analogue or hard-wired controllers are therefore disregarded.

Digital control systems can be assigned to the groups microprocessor, digital signal processor (DSP), field programmable gate array (FPGA), personal computer (PC) and software-in-the-loop / rapid prototyping equipment. Intersections and ambiguities are possible, but typical characteristics of these groups are still evident as follows.

General purpose microprocessors and microcontrollers are cheap and easy to buy. Evolution boards for rather powerful ARM microcontrollers are available for less than £20 for example from STMicroelectronics, but such a platform does not provide enough analogue field connections with the required update rate, noise rejection and resolution. The possibilities to record experimental data are restricted.

In [11] the digital signal processor (DSP) TMS320C25 from Texas Instruments demonstrates the performance of DSPs in a 5-DOF AMB with 15 kHz sampling frequency. The paper concludes that DSPs with an instruction set optimised for data processing and pipelining are better suited than general purpose microprocessors and that they allow a reasonable algorithm complexity.

To ease the development with modern, very complex DSPs the company Visual Solutions, Inc. in Massechusetts distributes the software VisSim, a visual block diagram programming language that is translated into C-code for one of the supported signal processors. The software allows simulation, code optimisation and debugging [1]. With this software the problem of building a reliable, high quality hardware platform is not solved. Also, the proprietary and rare programming language may have mistakes and limitations. The user is dependent on the vendor [48].

For high speed parallel data processing FPGAs are an alternative to DSPs. The reconfigurable hardware of the FPGA combines the advantages of parallel, low-latency hardware processing with the interchangeability of microprocessor programmes. FPGAs are available in different sizes and complexities and they can be found with integrated DSPs, microprocessors, memory blocks and calculation units [121, 5]. Analogue voltages have to be connected via external DACs and ADCs.

FPGA and DSP evolution boards are available for example from the company orsys, but there are not enough analogue connections on these boards. The platforms "X3-SD16" and "X3-Servo" from the company Innovative Integration are based on Spartan3A FPGAs from Xilinx [121]. Both boards are Matlab/Simulink programmable, avoiding time-consuming HDL implementations, and prices are around £8,000 including software to enable most of the functionality. Additional software has to be purchased from Xilinx for translate, link, place and route and the designer needs experience in a hardware description language, not only in Matlab [49]. The build time is also too long to be practi-

cal: approximately 12 minutes for a 2.4 GHz PC when the FPGA is 85 % full. After each power-up the configuration has to be reloaded because there is no non-volatile memory on the boards [49].

Personal computers (PCs) are of interest if they have a real-time extension [7]. This solution makes use of the very powerful and comparatively cheap PC hardware in combination with analogue and digital input and output plug-in cards as they are available for example from Meilhaus Electronic and Innovative Integration. Linux or Windows CE are popular operation systems, Linux in combination with RTAI, Xenomai, Embedix, RT-Linux and others [1]. There are also independent, commercial real-time operation systems such as Lynx, QNX and VxWorks [91].

The suitability of RT-Linux for a magnetic bearing control with state control with 45 states has been investigated in a case study in [48]. Humphrey proves the predictability (ability to meet sampling deadlines) and demonstrates a cycle-time of 125 µs in an AMB control. Petzold successfully builds a magnetic bearing based on RTAI [91]. The real-time problem can be overcome, but the expense of work for programming is immense and modifications of the underlying system may become necessary [48, 91].

Systems for software-in-the-loop development or rapid prototyping are characterized by their especially powerful hardware and their ease of programming, debugging and connecting external signals [1]. Unfortunately, these systems are very expensive, see below.

An example of rapid prototyping equipment is the modular product family "NI CompactRIO" from National Instruments Corporation. The company dSPACE [26] also provides a range of modular and single-board architectures. dSPACE products are programmed in Matlab/Simulink and for real-time monitoring and data recording dSPACE

[7] PC does not neccesarily imply an x86 architecture. There is a plethora of for example ARM boards with Linux operation system. None of them shall be cited here because the range is too numerous to give an exhaustive overview.

offers its own data visualisation software. For the magnetic bearing control either a well equipped modular system (about £25,000) or one of the most powerful single-board platforms had to be employed. dSPACE hardware is often used for AMB control, e.g. [69, 68, 98]. Systems from the Swiss company Speedgoat GmbH [109] fit into the same category[8]. The modular concept is based on x86 computer hardware for the main controller, but the operation system is not Windows or Linux, but "Simulink Real-Time kernel" based on RTOS-32 from the company On Time. IO modules are available for analogue signals, digital, general purpose lines, serial protocols, PWM and others. The use of reconfigurable FPGAs in some of the IO modules makes it possible to change the set of supported protocols without buying new hardware [109].

It can be inferred that rapid prototyping equipment is the most recommendable choice if ease of development and interchangeability have a higher priority than a low price for the hardware. Also, powerful FPGA boards are not cheap either. Rapid prototyping equipment provides a very powerful solution regarding connectivity and CPU power and it provides easy methods to visualize and store date. Before single products can be evaluated, the requirements have to be defined.

3.4.2 Requirements for the controller hardware

A development-friendly AMB control for the roll-to-roll machine must meet the following requirements[9]:

1. A servo update rate of 10 kHz: In section 2.3.2 the significance of a high update rate has been explained. Magnetic bearings often have 10 kHz [69, 43, 11, 11, 68, 98, 4, 41] or 5 kHz or even 20 kHz [91, 64, 60, 124] update rate. Is 5 kHz sufficient in this

[8] Speedgoat is an offspring of MathWorks and supersedes the "xPC-Target-Box", an obsolete MathWorks product [1].

[9] These requirements apply to the magnetic bearing for the R2R machine and they are independent of the actually achievable objectives for this research project.

application? This question can be answered by budgeting the phase margin [50]. The radial AMB with a maximum stiffness of $15.6\,\mathrm{N/\mu m}$ moves a mass of $1/2m = 100\,\mathrm{kg}$. The intersection frequency is $f_\mathrm{c} = 1/(2\pi)\cdot\sqrt{2c_y/m} = 63\,\mathrm{Hz}$ and the open-loop unity-gain cross-over frequency is two times more [81]: $f_\mathrm{d} = 2f_\mathrm{c} = 126\,\mathrm{Hz}$. At this frequency the phase lead should be 30° or more [107]. Assuming the derivative feedback acts from $1/3f_\mathrm{d}$ corner frequency and the P(I)D control is tamed at $3f_\mathrm{d}$, as recommended in [81], then a phase of 72° can be attributed to the PD control at 126 Hz and −18° to the taming action. A sensor amplifier[10] with a first order low-pass filter at 18.45 kHz causes further −0.4° and a power amplifier with 2 kHz bandwidth −3.6° at 126 Hz. With 5 kHz sampling frequency the controller delays the signal by approximately $2\cdot 200\,\mu\mathrm{s} = 400\,\mu\mathrm{s} \equiv -18.1°$ [10]. Everything together leaves 31.9° phase margin. That is just enough, but it leaves no safety for further unconsidered delays and the control hardware has a considerable contribution to the overall phase lag. 10 kHz is therefore safer and might even allow to enhance the stiffness slightly.

2. Min. 16 differential analogue inputs with min. 15 bits resolution and at least 10 kHz sampling rate. Eight of them are used to read the four encoders with two analogue outputs each[11], five measure the absolute position of the shaft plus potentially one compensation measurement[12] and two measure the temperature of the bearing housings. The temperature must be monitored to avoid overheating when the water cooling beaks down. The minimal sampling frequency equals the control update frequency of 10 kHz. 15 bits resolution are necessary for the absolute sensors to

[10] The sensor amplifier is necessary to read the encoders, see section 4.1.2. Gap sensors may have approximately the same cut-off frequency.

[11] Only the signals *a* and *b* are used, because reference and limit switch are not supported by the scale.

[12] The temperature drift of gap sensors can either be compensated with two opposing sensors for each channel or as suggested here with one additional reference sensor with known gap size.

achieve a resolution of at least 50 nm at 1 mm range.

3. Min. 10 analogue outputs with at least 10 kHz sampling rate and ± 10 V output range for the ten actuators. A higher sampling rate than 10 kHz could be advantageous to allow instant output changes after the calculation to shorten the overall delay time. ± 10 V is the input voltage range of the amplifiers [3].

4. Min. 1 incremental encoder interface input for one rotary encoder, fast enough to capture harmonic or square wave signals with 115 kHz. The current angular encoders of the axis[13] have $2,300$ lines on the circumference and rotate at a maximum speed of 300 rpm. Currently, the encoders output analogue 1 V_{PP} signals, but the control interface needn't necessarily be analogue. Interpolation is not necessary because the signal is only used for the magnetic bearing control, not for the rotary motor control.

5. Control of all actuators in one unit to allow for centralized control. This denies distributed, possibly easier solutions.

6. Hard real-time capability and reliability.

In addition to these strict requirements some additional functions would be useful such as an interface to the superordinate machine control. Also, the system should have non-volatile memory for the programme so that it can run stand-alone without the host computer and start automatically after power-up. Alternative requirements, for example external interface electronics for the encoders with quadrature output, could be formulated, but this set is considered most promising.

[13] These are two optical angular encoders with 150 mm nominal diameter, company Renishaw, type RESM20USA150. They might be replaced by different encoders later, see section 3.5.

3.4.3 Introduction of possible systems for the AMB control

The vast amount of companies and products can be narrowed down to three most promising solutions that meet the requirements best:

1. The single-board hardware "MicroLabBox" from dSPACE is based on a dual-core processor with 2 GHz CPU speed. It has its own mobile housing with different options for the connectors. It can run the programme in stand-alone operation, ie. without the host computer and from its own non-volatile memory. It is Matlab/Simulink programmable and shipped with software for graphical run-time monitoring of variables. In addition to the required interfaces it incorporates a sensor power supply and UART and CAN interfaces [26]. These might be useful for the communication to the machine control.

2. The DS1103 from dSPACE is also a single-board hardware, but it consists of several pieces of hardware. The main controller board with 1 GHz PowerPC and slave-DSP TMS320F240 is supposed to be connected to the host via ISA. If the host computer has no ISA slot, an extension box for the DS1103 PCB is connected to a PCI card by means of an optical cable. The DS1103 cannot run stand-alone. The analogue and digital IOs are accessible via BNC and sub-D connectors on a separate connector panel. Considerable digital interfaces for the communication to other systems are SPI, UART and CAN [26].

3. A certain configuration of modular hardware from Speedgoat depicts the third option. It is the "performance real-time target machine" with the IO modules "IO106", "IO111" and "IO317". Digital interfaces are implemented on the FPGA-module IO317. The other two modules are responsible for analogue inputs and outputs. The system is programmable in Matlab/Simulink.

These general characteristics make all three systems appear well suited. The next sections analyses which system meets the exact specifications, especially the IO requirements best.

3.4.4 Final decision

Table 3.2 compares the options introduced in section 3.4.3 with respect to certain requirements including prices and lead times[14].

Table 3.2: Listing of the control hardware specifications and three potential platforms including prices and lead times [109, 26]

Criterion	Requirement	MicroLabBox	DS1103	Speedgoat
Analogue input channels	16×15 bits, 10 kSPS, simultaneous	8×14 bits, 10 MSPS+ 24×16 bits, 1 MSPS, simult., diff.	16×16 bits, 1 MSPS, multiplexed, single-ended	16 diff. or 32 single-ended, 16 bits, up to 200 kHz, simultaneous
Analogue output channels	10 with min. 10 kSPS ± 10 V range,	16×16 bits, 1 MSPS, ± 10 V, simultaneous	8×16 bits, 5 µs settling time, ± 10 V, simultaneous	16×16 bits 300 kSPS, ± 10 V, simultaneous
Encoder input interfaces	1, digital or better analogue 1 V_{PP}, 115 kHz	2, digital	6 digital, 1 analogue 1 V_{PP}, 600 kHz	3, digital, 10 MHz
Controller update rate	10 kHz	unknown	10 kHz	20 kHz
Price	not defined	£11,292	£7,644	CHF25,135.2 $\approx$ £17,565.25
Lead time	-	6 – 10 weeks	3 – 6 weeks	4 weeks

All three products satisfy the analogue input requirement. On the performance: The DS1103 multiplexes four internal ADCs to read 16 analogue inputs, but the sampling rate is 100 times higher than the minimum - high enough for multiplexing. The MicroLabBox

[14]The prices and lead times are based on quotations and include 20 % VAT and shipping.

has differential inputs, but there is only one BNC connector per channel, not one for plus and one for minus. The second criterion is met by all except the DS1103. The limitation to eight outputs can be conquered with an additional analogue circuit, if the method of a constant bias current is applied as described in section 2.2.3. With this method only eight degrees of freedom are necessary to drive ten coils[15], but the interchangeability would be restricted. All products have the required number of encoder inputs, but for the MicroLabBox the speed is not known, because the product is new and detailed information on this interface is not available yet.

The estimate of the update rate for the Speedgoat equipment is based on documentation from Speedgoat [109]. The IO modules IO106, IO111 and IO317 all cause a latency depending on the amount of channels. These add to the kernel and algorithm delay. Table 3.3 shows the calculation of the predicted cycle time.

Table 3.3: Estimate of the cycle time for the proposed Speedgoat product, with *nChannel* being the number of signals generated or captured with the IO card

Instance	Function	Formula	nChannel	Time slice
IO106	Analogue in	$7.2\,\mu s + 1.4\,\mu s \cdot nChannel/2$	16	$18.4\,\mu s$
IO111	Analogue out	$1.0\,\mu s + 0.2\,\mu s \cdot nChannel$	10	$3.0\,\mu s$
IO317	Digital in/out	$6.4\,\mu s + 3.2\,\mu s \cdot nChannel$	1	$9.6\,\mu s$
CPU	-	-	-	$8.0\,\mu s$
Sum	-	Σ	-	$39.0\,\mu s$

With a total of 39 µs and a few percent safety 20 kHz update rate should be possible.

The sampling rate of 10 kHz for the DS1103 can be estimated by comparing similar projects with the same control hardware [69, 68]. In [98] a "DS1005 PPC Board" from dSPACE is used for the control of a magnetic bearing. It utilises the same CPU (PowerPC 750GX and 1 GHz) as the DS1103. A controller update rate of 10 kHz is reported. For the

[15]The bias current is assumed to be the same value for the right radial bearing and the left radial bearing, whereas the horizontal and the vertical bias current may differ.

MicroLabBox no evaluations as magnetic bearing controller are available yet, but compared with the DS1103 the higher CPU power ($2 \times 2\,\text{GHz}$ in contrast to $1 \times 1\,\text{GHz}$) and the high sampling rates of the simultaneous DACs and ADCs suggest a higher performance.

The degree of satisfaction of the three products varies. In the evaluation chart in table 3.4 a value of 3 represents the highest merit.

Table 3.4: Evaluation chart for the three alternative controllers

Criterion	Weighting factor	MicroLabBox	DS1103	Speedgoat
Analogue IOs	0.3	2	1	3
Digital IOs and communication	0.05	2	2	3
CPU performance	0.15	2	1	3
Software usability	0.1	3	3	2
Price	0.3	2	3	1
Availability	0.1	1	3	2
Sum	1.0	2.0	2.05	2.2

According to table 3.4 the Speedgoat product has the highest merit (2.2). The main problem with the MicroLabBox is its availability (not even ten weeks lead time can be promised) and the DS1103 has the limitation of only eight analogue outputs. A discount of 30 % was negotiated and the Speedgoat product was bought.

3.5 Mechanical design of the magnetic bearing axis

A pivotal contribution to the discussion if magnetic bearings are applicable to R2R printing is the mechanical design of the printing roller axis. A suitable arrangement of components would combine all the necessary functions with good dynamic properties. This section highlights some basic design considerations and makes a suggestion for a mag-

netic bearing layout.

3.5.1 Boundary conditions

Boundary conditions for the design arise from the dimensional specifications in section 1.2, from the sizes of the actuators and sensors shown in figure B.1 and the required overall functionality. The following functions have to be incorporated into each of the two bearing blocks on either side of the printing roller:

1. One radial actuator so that together with the other bearing block four degrees of freedom are controllable

2. At least one thrust bearing actuator for the entire axis

3. Radial position measurement in two directions with linear optical encoders

4. Inductive radial position measurement with the inductive sensors supplied by Foshan Genesis, see figure B.1. This additional position measurement is necessary for the commissioning because the encoders don't yield the absolute position and they only function when the axial position is already in the valid range.

5. Two sets of touch-down bearings. When the printing roller is changed it is required to rotate each part of the spindle independently, which would not be possible with only one touch-down bearing on each side of the roller.

6. The same torque motor as in the hydrostatic design

7. An angular encoder for the motor control

8. An axial flange to connect the printing roller including its trunnion

9. A water cooling system for the AMB that can accommodate the energy dissipation of approximately 500 W

10. A hollow shaft for the connection of the printing roller water cooling

The underlying postulate of the design is that radial movements of the spindle are in the range of hundred micrometers or more while axial movements are restricted to a few micrometers. Far axial movements as they could be caused by thermal expansion would lead to layer registration errors in the printing process and must be avoided by precise temperature control.

The arrangement of components should allow easy replacement of the touch-down bearings without the need to take everything apart and to realign it afterwards. Moreover the radial position sensors should be as close to the radial actuators as possible because of the bending nodes that would otherwise fall between the actuators and the non-collocated sensors [35, 11]. Radial position sensors and the radial actuator should also be close to the printing roller because that is the part of the axis that has to be controlled precisely. It could even be argued to have the encoder gratings on the printing roller itself which would make the calibration easier. One disadvantage of that solution would be that the profile had to be renewed each time the structures on the printing surface are resharpened as the whole printing roller is submerged for the coating. An other disadvantage is the increased distance between sensors and radial actuators.

The distance between axial sensors and axial actuator is considered less critical because the stiffness in longitudinal direction of the shaft is usually high, resulting in high frequencies of longitudinal resonant modes. It is, however, important to minimize the distance between axial sensors and the printing roller to eliminate the influence of thermal expansion of the shaft inside the bearing. Finally the axial sensors should be installed in line with the axis to avoid the Abbe offset.

3.5.2 Proposed arrangement of components

Figure 3.8 shows the proposed integration of components. It is a section view of the Siemens NX magnetic bearing model with horizontal viewing direction. A different cut through the same assembly is shown in figure 3.9. The exterior dimensions are that of a cuboid, only the motor housing is round. Figure 3.7 displays the assembled axis including the printing roller designed by Roger Read from Cranfield University.

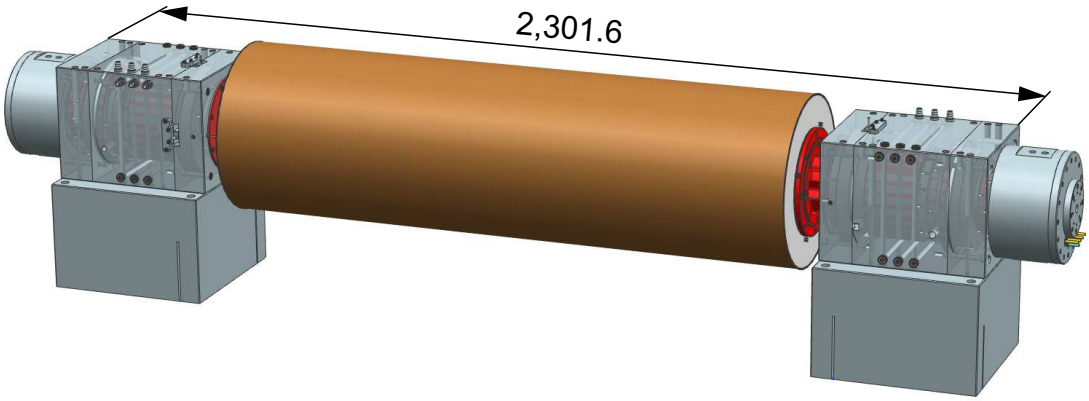

Figure 3.7: Printing roller axis with magnetic bearings

The radial actuator with inductive sensor on one end and radial encoders on the opposing end is located close to the trunnion that is connected to the printing roller to allow for accurate position control. Because the inductive sensors are only used for the commissioning before the more precise radial encoders take over, they are located at the end of the radial bearing that is further away from the drum.

Even closer to the printing roller is one of the touch-down bearings. The reason for the touch-down bearing to be at the end of the housing is that it must be accessible later. When this touch-down bearing is changed, trunnion and printing roller have to be disconnected and when they are reconnected, the run-out may have changed. This is a drawback of having two sets of touch-down bearings in two different axial positions; Only by opening

the axis the inner touch-down bearings can be serviced.

For ideal alignment the radial encoder in figure 3.8 can be adjusted in three degrees of freedom. The mounting plate on the outside of the housing allows adjustment of the encoder ride height, horizontal positioning and rotation about the vertical axis. Radial adjustments are not necessary. Respective conditions are valid for the second radial encoder that is visible in the section view 3.9.

The parts that needn't be close to the roller are the axial bearing, the outer touch-down bearings, the motor and its rotary encoder. In this design the thrust bearing actuator comes next. The main reason is its relatively wide shaft diameter. The motor with a shaft diameter of 50 mm would weaken the shaft if it was not at the far end of the construction. With the proposed order the shaft is getting increasingly strong from the motor to the printing roller. The trunnion, which was noticeably thin in the old design, had to be redesigned. Changing the touch-down bearings is possible by removing the motor and its housing. For performance reasons the longer, axially constrained touch-down bearing is further away from the printing roller.

Instead of the ordinary construction for the axial bearing with two opposing coils and the thrust disc in between, the solution shown here can only move the rotor in one direction. Together with the magnetic bearing on the other end of the printing roller both directions of movement are essentially possible, but the implications of this solution are still critical. For example the construction of the printing roller must have a certain strength to bear the continuous axial forces of the bias current control. The reason why only half a thrust bearing is located on either side is that the construction should be as short as possible. An additional axial stator would make the housing about 42 mm longer and that would not only cause a space problem in the machine but it would also lead to excessive radial vibrations of the torque motor rotor. With a complete axial bearing on only one end of the roller the two housings would look different which is not advisable for

a cost-effective production or alternatively one of them would be hollow where the axial bearing is missing. For precise axial positioning it may also be better to have a completely symmetric system, not only sensors in symmetric places [108].

At the very end is the angular encoder for the motor control. Concentricity adjustments of the angular encoder can be done when everything else is assembled and the magnetic bearing is in operation, but it has to be readjusted each time the printing roller is changed. To save time it is beneficial to have a rotary encoder with wider run-out tolerance. That is the reason why the original encoder of the hydrostatic design with radial air gap has been replaced by this encoder (ERO 6000 from Heidenhain [23]) with axial air gap. The axial mounting tolerance of $\pm 100\,\mu m$ is narrow, but the radial run-out tolerance is extended. This is consistent with the posit that the axial position is controlled precisely and only radial motions occur. In order to maintain good accuracy in spite of concentricity errors of the encoder, two reading heads are mounted on opposing sides of the scale, one on top and one below. The signals of the two are averaged later.

In figure 3.9 the capacitive sensors for axial position measurement are shown. They are close to the printing roller, which is good, but they are not in line with the axis, because a hollow shaft is required for the water cooling of the printing roller. As a workaround two capacitive sensors are averaged. Their target surface is the encoder disc that can be cut level and smooth when the structures on the other side are cut, so that a good target surface is achieved without much additional effort.

Suitable capacitive probes would be CS08, CS1, CS1HP or CSE1 from Micro-Epsilon or the P016-6032 - C8-3.2 -2.0 from Lion Precision [70] with 250 to $1,500\,\mu m$ range and 20 nm RMS resolution at 10 kHz bandwidth. The price is about £ 15,000 for four sensors. The fixture with a set screw as shown is the preferred way of mounting capacitive sensors but the screw should be from plastic and when the alignment is complete it should be supported by low-shrinkage epoxy [108, 78]. There are capacitive sensor systems that

don't require target grounding but the sensor channels must be synchronised [78].

3.5.3 Details and materials

The material for all parts of the casing and the shaft is aluminium. The casing benefits from the high thermal conductivity and the shaft from the low weight of aluminium. The weight reduction is reinforced by the centre hole in the shaft. Aluminium is also quick to machine and easy to buy in large blocks as required here [129]. There are grades of aluminium with low internal stresses and good plasticity [74]. Slots in the sockets make up for different thermal expansion of the aluminium and the stone base underneath although the temperature should not normally vary at any time.

The radial bearing journal is supposed to be made from non-grain-oriented silicon-steel as it is an affordable material with low anisotropy, reduced eddy current losses and a thin hysteresis curve [39]. Grade M290-50A has the same high saturation density as the stator material [83]. In general low carbon steel with less than 0.001 % carbon, cobalt-iron or nickel-iron could be used instead of silicon-steel, as long as the saturation induction is at least as high as in the stator material. However, silicon-steel is an affordable choice if no special requirements like very high saturation polarization, high initial permeability or particularly low hysteresis are a concern. Silicon-iron has a higher breaking stress than pure iron [20, 39]. In contrast to the radial rotor the axial rotor should not be laminated because it does not see a changing field and stability is of importance. The inductive sensor target is also from silicon-steel and can be made from the same sheets as the radial rotor. The sensor supplier Foshan Genesis [31] recommends titanium rings on both sides of the iron ring.

The auxiliary bearings have tolerance rings around the outer ring as elastically soft support to limit the load and frequency of the whirl motion when the shaft drops. The

massive aluminium structure around still maintains integrity of the bearing and precise alignment. This is recommended by Schweitzer and Nordmann [10]. Rolling element bearings together with damping rings absorb the energy of a de-levitation and avoid excitation of bending modes by damping. The tolerance rings from spring steel are the preferred option for heavy rotors. For light rotors o-rings made from fluor-kautschuk can be used instead [10].

The water cooling consists of several holes that go all the way through the aluminium and are sealed by plugs. They intersect with each other to create three continuous pipes of 960 mm length. These can be connected in parallel or in series to work with different chillers.

3.5.4 Limitations of the design

Reflecting on the boundary conditions from above it must be noted that most of them have been accomplished but not all of them: The axial position is not measured in line with the shaft and the length of the whole composition is longer than allowed by the specifications and much longer than the hydrostatic bearing. Drawbacks of the design are also the high cost of the capacitive sensors, the limited graduation accuracy of the rotary encoder and the weakening of the housing because of the big scale for the radial encoders. The design prompts that the integration of radial sensors is more difficult for encoders than for ordinary gap sensors. The temperature control of the printing roller must be precise and safe to avoid thermal expansions of more than the encoders' mounting tolerance. Details of the design like tolerances and the exact procedure of the alignment and commissioning are not defined yet. It may be necessary to validate the design with FEA tools and if it turns out that the printing roller construction is too weak, it needs modifications, too. The water cooling for the printing roller is still to be designed.

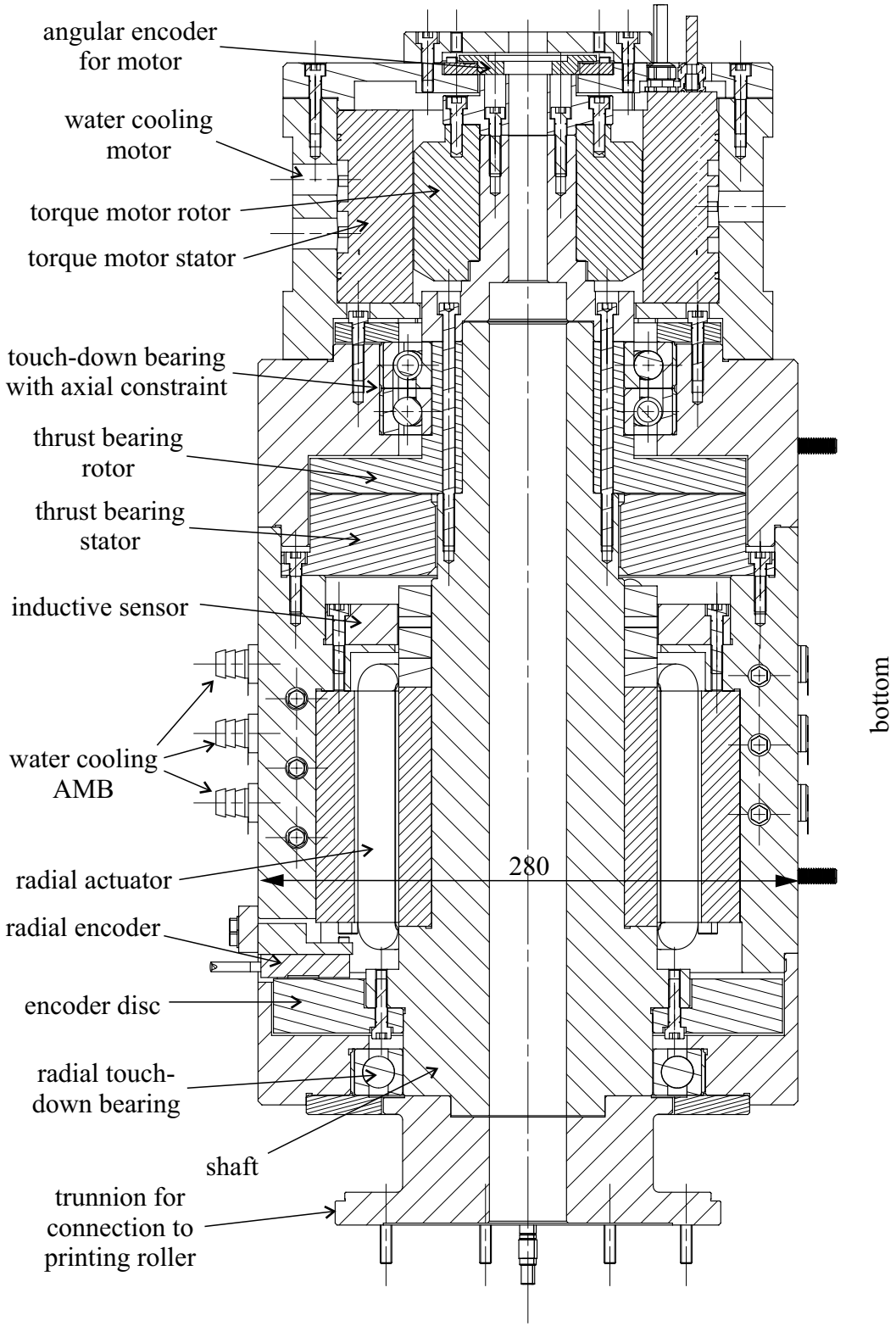

Figure 3.8: Elevation of magnetic bearing spindle for patterning roller axis

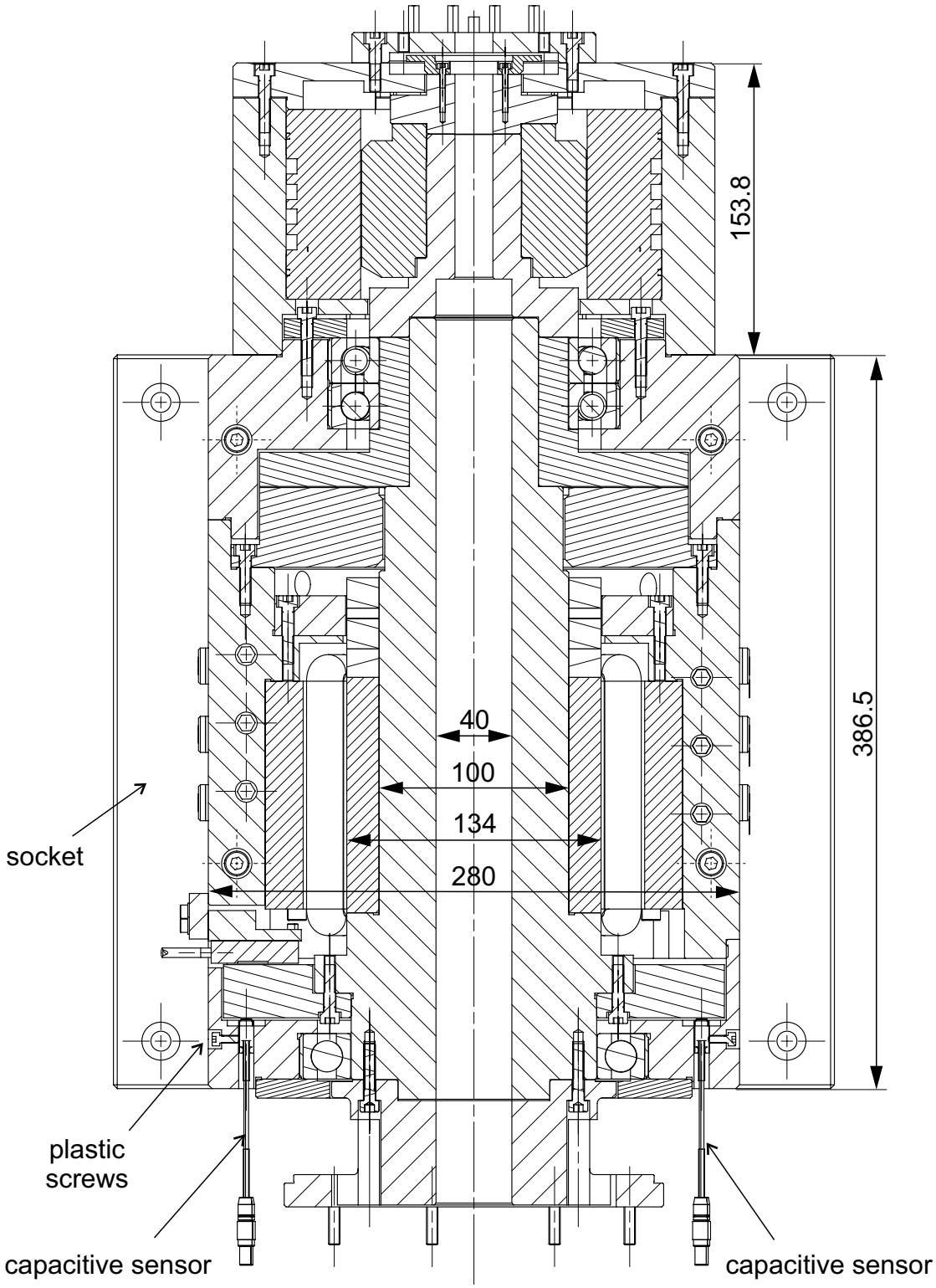

Figure 3.9: Section view of magnetic bearing spindle for patterning roller axis

Chapter 4

Experimental procedure

The description of experimental procedures is divided into two parts: firstly, arrangements and procedures with linear encoders and concentric, mechanically ruled scales, secondly, the magnetic bearing experimental test rig.

4.1 Encoder gratings experiments

The concept to measure the radial position of the spindle with linear, incremental, optical encoders and turned scales has been described in section 3.3. The aim of the experiments is to find a process to create a suitable profile and to measure its performance.

4.1.1 Replication of gratings by machining

The production of scales with conventional lithography, etching and deposition techniques is optimized for each encoder type and brief descriptions can be found in [24], but the required round scale with concentric, coplanar fringes is not readily available. A prototype made with conventional technologies would require "extremely specialized and costly equipment and procedures" [21] p. 334 and it would be difficult to make the patterns

concentric with the axis. Also, the exact process parameters for photolithography, etching and deposition are not published but company specific know-how. On the other hand, ruling gratings, that means cutting grooves into a flat surface with a diamond tool or other hard material is not an outlandish technique to produce gratings and it finds application in spectrometers and encoders of capacitive or optical type [12, 67].

The history of ruling machines used for phase gratings dates back to the nineteenth century where Fraunhofer made diffraction gratings with a ruling machine for spectral analysis with an optical spectrometer [12]. These first diffraction gratings were made with randomly chosen diamond splitters and the characteristics couldn't be shaped actively before the 20th-century. The precision of the groove spacing was only as good as the lead screw, which couldn't be manufactured more precisely than to $\pm 200\,\text{nm}$. This limitation was only overcome in the second half of the 20th-century with feedback position control [74].

Today, a favoured profile for mechanical ruling is the blazed grating, grooves with triangular footprint placed close to each other so that the original surface completely vanishes and a saw-tooth or ladder structure is created [54, 21, 67]. Sinusoidal profiles are also feasible with CNC milling machines [37]. These two profiles are designed in a way that they can be cut with a tool that is much bigger than the resulting grooves. Blazed gratings with $4,000$ grooves per mm have been reported [74]. Because the entire surface is reshaped when cutting sinusoidal grooves or blazed gratings, it can be anticipated that inaccuracies caused by thermal spindle growth, non-perpendicular machine axes, workpiece and machine distortions are eliminated.

Examples of more recent blazed gratings are the one reported by Davies [21] cut into 6061 aluminium with a grating period of $151.05\,\mu\text{m}$ or the experiments conducted in [54] to optimize geometrical parameters for a cutting process with $12.66\,\mu\text{m}$ graduation period. An example of a sinusoidal profile is the grid cut into an aluminium surface as a 2D scale

for position measurements with an incremental encoder [37]. This encoder is based on a deflected laser beam that is detected by position sensitive devices. With a pitch of 100 µm and a special, round profile an ordinary radius tool with 1 mm nose radius can be used for the entire surface [37].

Regarding the material, aluminium and in particular 6061 aluminium seems to be a common choice for gratings that needn't be highly wear resistant. Aluminium is reflective over a wide range of wavelengths and the formation of Al_2O_3 on the surface only reduces the reflectivity below 200 nm and this limit can be extended with MgF_2 or LiF coatings. Aluminium combines low internal stress with good deformability. Aluminium of the grade 6061 wears the diamond tool less than aluminium with higher concentrations of impurities. Other materials are only possible if they are diamond turnable and highly reflective. Gold and alloys of tin and copper [67] are sometimes preferred, but 95 % of all gratings are made from aluminium [74, 12]. From the machining point of view and especially when feature fidelity is considered, nickel-phosphorous (NiP) seems to be a good material, too [123]. The experiences made by Davies with aluminium prove the suitability of aluminium. The burr formation is not severe [21].

It can be concluded that the history of mechanical ruling dates back to the 19th-century and that diamond turning of gratings is a well-established technique. However, the focus lies clearly on diffraction gratings that can be made in form of blazed gratings and the applications are different. In order to make scales that meet the requirements of the linear encoder reading heads (section 3.3) the techniques for sinusoidal or blazed gratings can't be adopted directy. It seems that the required pattern of reflective and absorbent or scattering lines is difficult to make. The experiments described in this section must reveal a suitable technique for the machining process.

4.1.2 Experimental arrangement

Both cutting of the gratings and encoder experiments are conducted on a Nanotech 350UPL diamond turning lathe from Moore Technology Systems. The workpart is an aluminium disc, type 6061-T6 with 120 mm diameter and 29 mm length that is held by a vacuum chuck, see figure 4.1. Only the face is structured with concentric, coplanar grooves, not the cylindrical surface. The cuts are applied from radius $r = 43$ mm to 59 mm, starting with the bigger radius, creating a scale "length" of 16 mm for the encoder's optical area of 14 mm. In the figure half of the final raster area is already cut.

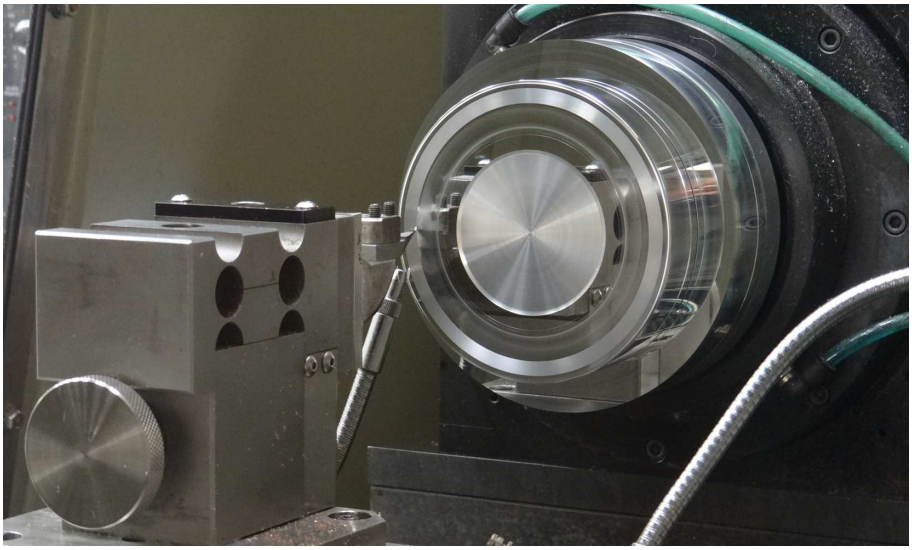

Figure 4.1: Photo of the encoder scale turning process on the Moore machine

The aluminium sample is smaller than the disc that will be used in the real magnetic bearing sensor. This makes the experiments less time-consuming and less expensive, but unfortunately the experiments exclude effects that may deteriorate the quality of the actual magnetic bearing sensor. These are mainly thermal spindle growth and tool wear. Because of the long turnaround time of the turning work (four to twelve weeks per sample) it was still decided to work with smaller discs. The reason for the wide thickness of the discs is

the flexibility of aluminium. A thinner sample would deflect under the turning forces and the forces of the vacuum chuck, leading to varying structure depths.

The cutting parameters are: 600 rpm spindle speed, 0.6 mm/min feed-in rate for plunging the grooves, which is 1 µm per revolution, and at the bottom of each groove one second dwell. An upwards jet of compressed air and white spirit from underneath is used for lubrication. The rake angle of any form tool is 0°. The radius tool generated flat surfaces are turned at 6 mm/min feed rate.

After finalisation of a certain profile the tool is replaced with the encoder reading head which can be mounted vertically (figure 4.2) or horizontally (figure 4.3). In both orientations the distance to the scale can be set according to the specification by moving the tool holder along its slideway. Tilt adjustments can be made with the fixture. The radial position must be adjusted so that the window is covered by the raster area completely.

Out of the two orientations of the reading head the vertical one is preferable to adjust the encoder position in tangential direction, see figure 4.2. Because the scale is curved, only in one position the scanned section of the scale is parallel to the fringes of the reticle and this position is not specified in the encoder documentation. Moving the spindle with the workpiece horizontally along the reading head allows to find the optimum position by evaluating the output signal quality. That is the benefit of the vertical arrangement. In the horizontal orientation radial movements can be performed, which is necessary for accuracy and related measurements.

The incremental position signals a and b are recorded with the analogue input module IO106 from Speedgoat, see section 3.4. Because the ADCs have 120 kHz low-pass filters and the controller update rate is only 10 kHz, an additional low-pass filter is required. This measure should reduce the measurement noise. The circuit diagram of the interface between encoder output and ADC is displayed in figure 4.4. In addition to the low-pass characteristic it converts the differential input signal into a single-ended signal and

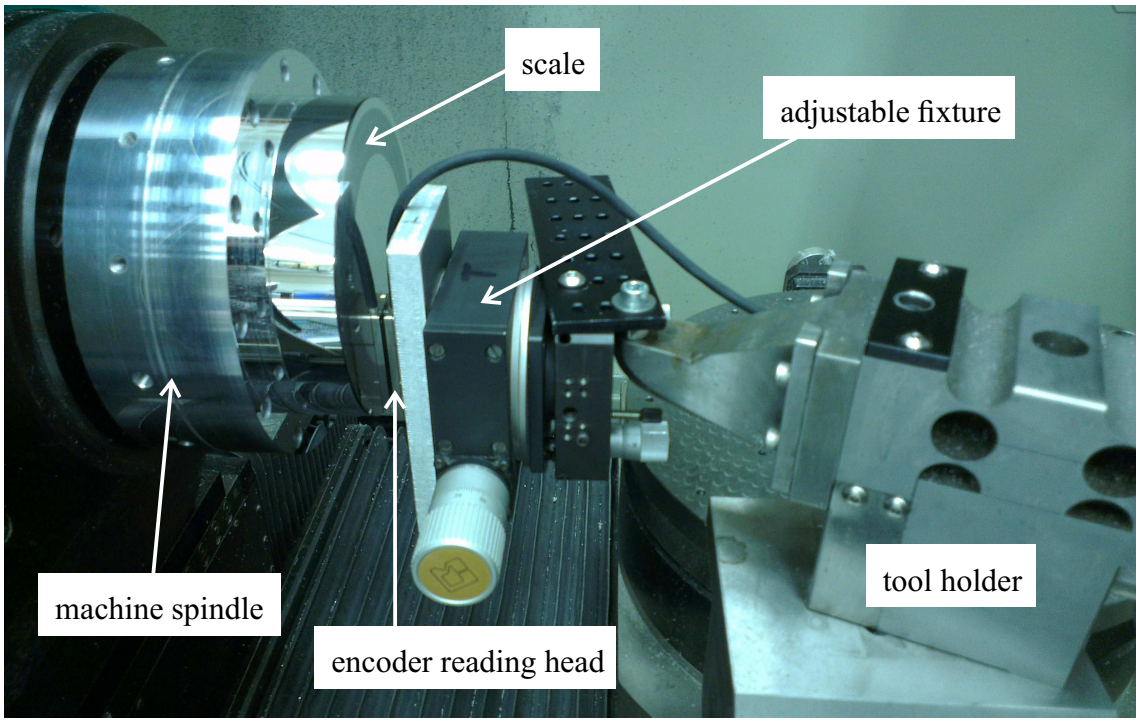

Figure 4.2: Photo of the experimental arrangement to test each scale with its encoder reading head in vertical pose

amplifies it by a factor of 3.92. The amplification could reduce the effective quantisation error and ADC noise and the single-ended signal is the preferred option for the ADC board in the final magnetic bearing. The low output impedance of the operational amplifier allows to use long cables and the circuit protects the encoder from short circuits and other operator mistakes. In appendix C the transfer characteristic

$$U_{\text{out}}(\mathrm{j}\omega) = \frac{39.2\,\text{k}\Omega}{10\,\text{k}\Omega} \frac{1}{\mathrm{j}\omega \cdot 39.2\,\text{k}\Omega \cdot 220\,\text{pF} + 1} \left(U_{\text{a}+}(\mathrm{j}\omega) - U_{\text{a}-}(\mathrm{j}\omega)\right) \tag{4.1}$$

is derived from the circuit diagram. This circuit diagram is recommended by the sensor manufacturer Heidenhain [24]. Because of the above benefits it is used for the encoder connection, albeit with adapted parameters.

It is necessary to determine the certainty of experimental results. For that reason all

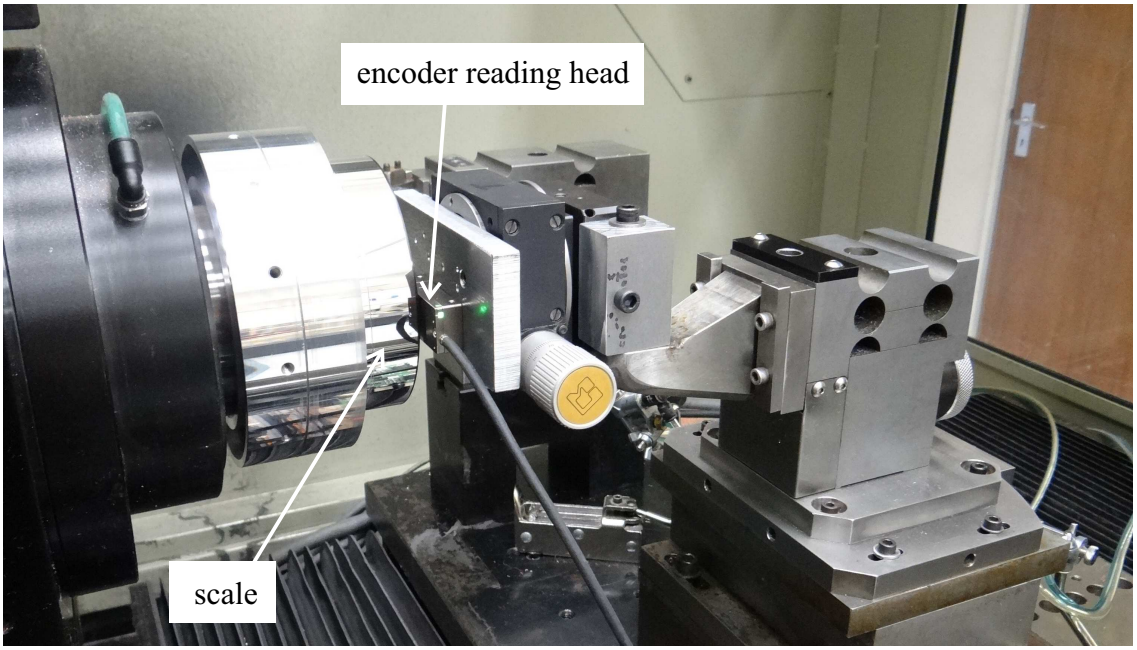

Figure 4.3: Photo of the experimental arrangement for horizontal encoder measurement

experiments are repeated n times and the sample standard deviation s is calculated with the formula

$$s = \sqrt{\frac{1}{n-1}\sum_{i=1}^{n}(x_i - \overline{x})^2}. \tag{4.2}$$

x is the individual reading and $\overline{x}$ is the sample mean. In most experiments n is 5. RMS values are calculated with n in the denominator, not $n-1$. All experiments are carried out at 10 kHz sampling rate.

4.1.3 Definition of grating profiles

The two encoder scanning heads LIDA 28 and LIDA 48 have been sponsored by Heidenhain, see section 3.3. With the available diamond cutting tools there are at least six different ways of creating contrast for these encoders by cutting grooves into aluminium.

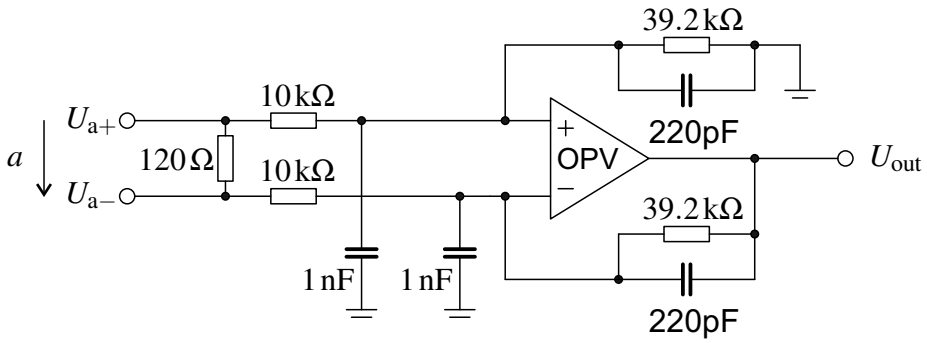

Figure 4.4: Circuit diagram of interface electronics to connect the encoder to the Speedgoat analogue inputs

Figure 4.5 illustrates three for 200 µm and three for 20 µm grating period. The requirement of the imaging scanning principle is an interchanging reflective and absorbent pattern with a space ratio of one to one, see section 3.3. For profiles (a) and (d) the sample is first cut blank with a round tool, creating a highly reflective surface. Then a pointed tool cuts the grooves that are meant to trap the light. According to Yan micro-cutting of V-grooves creates burr at the margins of the grooves and material stagnation at the tool-tip is a problem, but good results can be achieved if the final depth is approached in steps [123]. With different material, included angle and sample geometry the results are not directly comparable.

In versions (b) and (e) the entire surface is shaped with only one tool. A reduction of the spindle growth influence may be the advantage of these profiles as stated in the references [37, 21] and others from these authors. Also, the burr formation may have less influence compared with (a) and (d). The light is supposed to be reflected at the ground of the grooves. Versions (c) and (f) use blackboard paint to create an absorbent surface that lies flush with the reflective aluminium. The last cut is made with an ordinary round tool. This way any burr is cut off. Here the risks are that the paint wears the tool too quickly and that the paint as an unexplored material brings about other unexpected issues.

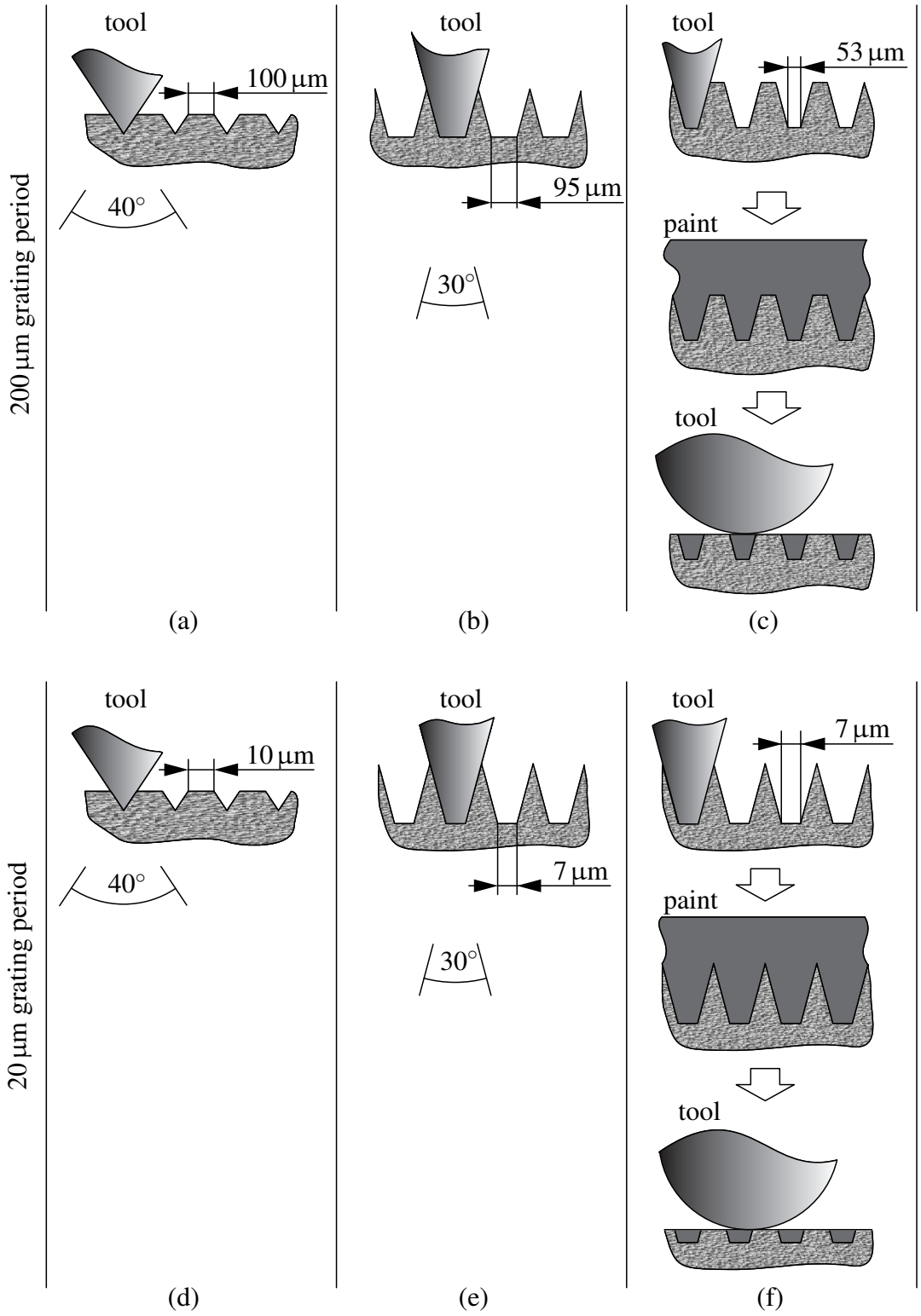

Figure 4.5: Six methods of cutting grating profiles into 6061 aluminium

In order to find a suitable profile and evaluate its performance, more than one of the six profiles should be machined and tested, but not necessarily all of them. An experimental procedure with branching is required to cope with the dilemma of a limited time scale on the one hand and the need to machine several profiles for the comparison on the other hand.

The procedure starts in the first row of figure 4.5, as the ten times wider structures are expected to be easier to manufacture. It was pointed out in section 3.3.4 that the smaller pitch is more likely to fulfil the precision requirements, but the coarse profile could at least prove the concept. Version (c) is arbitrarily set as the first run. If it does not function, versions (a) and (b) are made. If it works, no more discs need to be machined with 200 µm grating period. Proceeding in the second row the three profiles (d), (e) and (f) are made and the best one is selected for the magnetic bearing position sensor.

4.2 2-DOF magnetic bearing demonstrator with encoders

The magnetic bearing spindle designed in section 3.5 has not been built in the scope of the research project. The main reason is the complexity of the design and the limited time scale. Furthermore, other parts of the axis are still missing like the motor control and the water cooling for motor and roller, which are not part of this research project. Most importantly, the radial position measurement with encoders needs to be verified first.

4.2.1 Hardware description of the experimental AMB demonstrator

Instead of the R2R design, a less complex prototype has been built to demonstrate the radial encoder performance, see figure 4.6. It has only one radial bearing on the right to control two degrees of freedom of the shaft. The other end of the shaft is connected to the

spindle of the diamond turning lathe "Nanocentre" from the company Cranfield Precision via flexible coupling. The machine stabilizes the remaining four degrees of freedom and it can rotate the shaft at a defined speed. The flexible coupling in form of a bendable rod has been chosen after initial experiments with universal coupling had shown stability problems. Universal couplings are commonly used to decouple the driving motor from the magnetic bearing spindle [96, 18], but in this case the backlash of about 100 µm hindered the precise alignment and caused vibrations at certain angles of the shaft. The flexure is dimensioned in a way that it changes the expectable AMB stiffness only by about 0.5 % and in radial direction it is 80 times stiffer than the AMB so that it can be modelled as an ideal universal coupling. Refer to figure 4.8 for the realized setup.

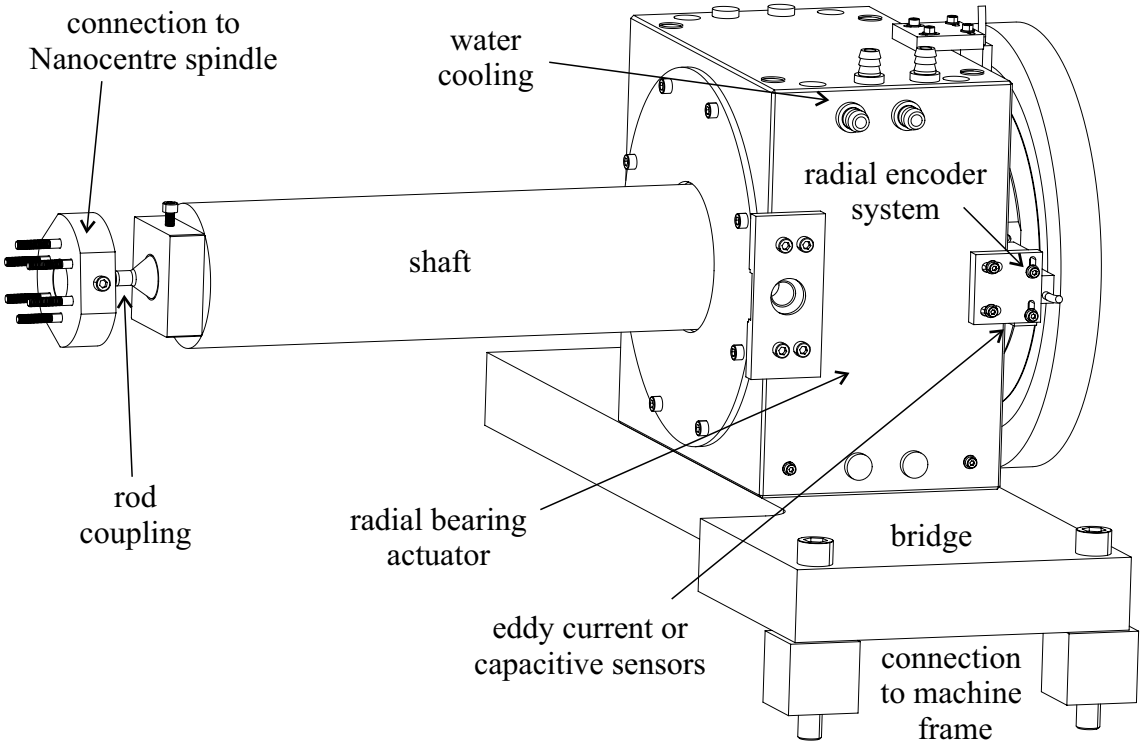

Figure 4.6: 2-DOF magnetic bearing demonstrator

Figure 4.7 visualises the arrangement of eddy current and capacitive sensors and encoders. They can be used alternatively to measure the position. The round aluminium

scale of the encoder, which usually covers the sensor ring behind it, is not displayed in the picture. The fixtures for the encoders are suitable for both LIDA 28 and LIDA 48 so that the type of reading head and scale profile can be incorporated according to the results of the grating experiments. For tangential and axial position adjustment the same principle with bolts in slots is used as in the proposed R2R magnetic bearing design. The eddy current sensors with 500 µm range are from Kaman Instrumentation Corporation (KDM7200) and the capacitive sensors from Lion Precision (DMT12) with 20 kHz bandwidth have a 75 nm peak-to-peak resolution specification for 10 kHz. The full-scale range is 508 µm. These sensors have been available easily but their short range denies their use in the final magnetic bearing. The RMS noise has to be measured. Because the gap sensors are hidden in holes inside the aluminium, they are indicated with dashed lines. The performance can be compared with encoders as all sensors act in approximately the same axial position.

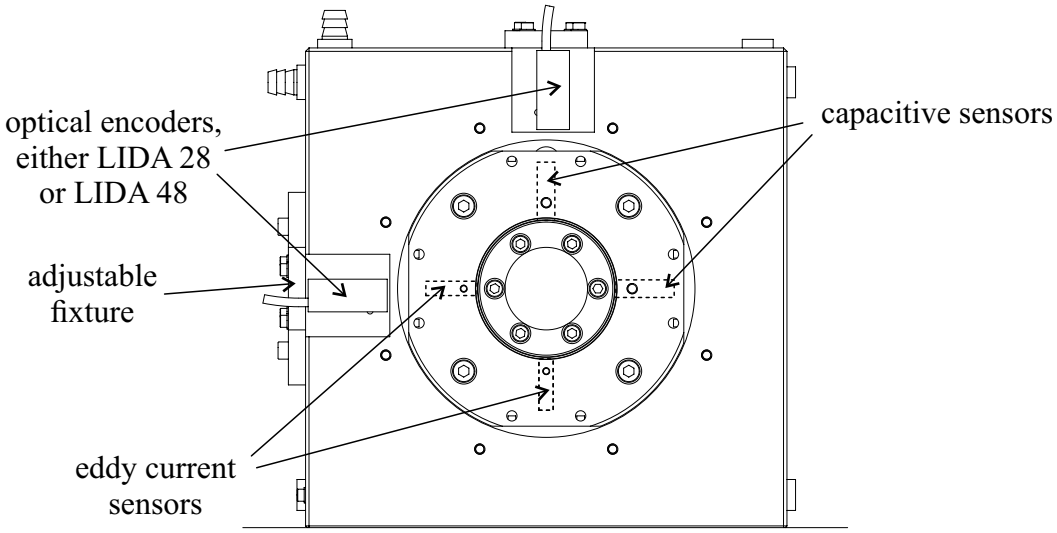

Figure 4.7: Sensor arrangement in the magnetic bearing prototype, displayed without encoder scale

To reduce the expenses and to establish comparable conditions, the same radial sta-

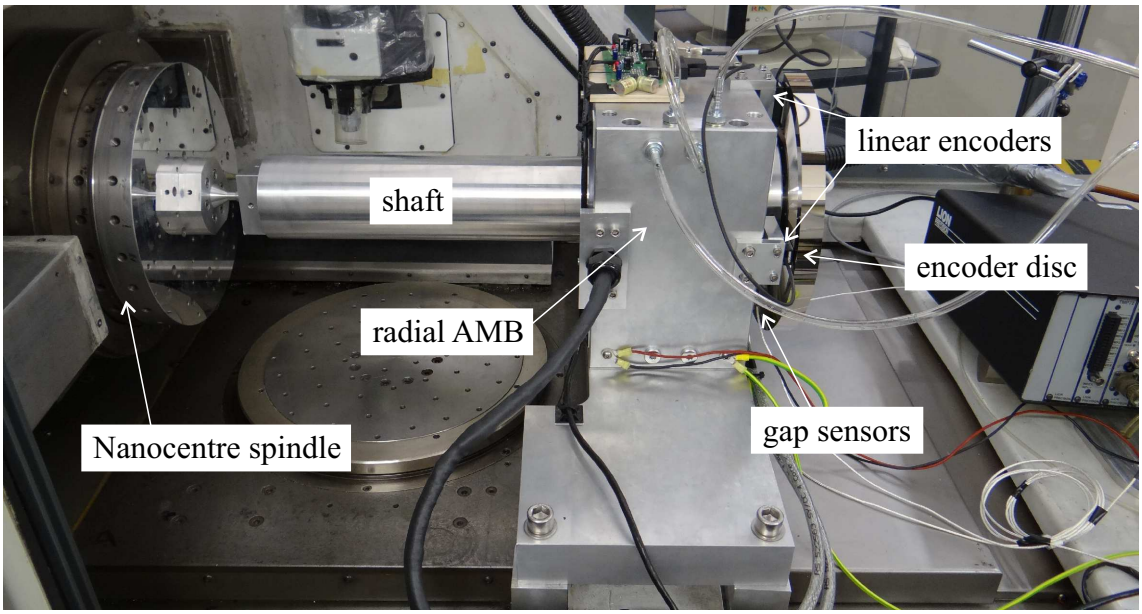

Figure 4.8: Photo of magnetic bearing setup in Nanocentre diamond turning machine

tor and power amplifiers are used as chosen for the R2R bearing, see section 3.2. The prototype uses the same water pipe system, albeit with only two pipes instead of three to account for the missing axial bearing. The nominal air gap width of the iron circuit is 0.6 mm and the auxiliary bearing clearance is 0.3 mm. The housing has a square exterior surface with 280 mm edge length. For the control and data logging Speedgoat hardware is employed as explained in section 3.4 with 10 kHz sampling rate. This sampling rate is used in all experiments. The iron rotor material is non-grain-oriented cold rolled electrical steel of the type M290-50A. The 0.5 mm sheets are insulated with bonding varnish and shrunk onto the shaft.

Objectives of the experiments with the simplified AMB rig are

- research on the general suitability of optical encoders for the position control in a magnetic bearing,

- measurement of the accuracy of axis of rotation at low speed and

- function testing of the radial stator in combination with the aerotech amplifiers.

The prime distinctions between the R2R magnetic bearing design and the actual experimental setup are the reduced weight of the demonstrator's rotor, its higher stiffness, the absence of a torque motor and the absence of other magnetic bearings along the shaft. With a diameter of 98 mm and a length of 600 mm the shaft is so stiff and compact that a flexible body analysis is considered unnecessary. The simplified design should ease the programming work, but it is also obvious that the experiments with it haven't got the same merit as the full-scale bearing.

4.2.2 Decentralized PID control

The theory of the one dimensional stiffness and damping design from section 2.3.1 is now applied separately to the two degrees of freedom of the prototype, see figure 4.9. The inherent behaviour without control on the left is thereby converted into the stable levitation on the right. Point P is the centre of rotation, which the scalar of inertia $J^{(\mathrm{P})}$ also refers to. For simplicity reasons the flexible coupling is treated as an ideal joint without tilt stiffness. Small deflections from the horizontal orientation are denoted with x_a at the point of the actuators and x_s at the sensors. $M_\mathrm{g} \approx 87.7\,\mathrm{Nm}$ represents the moment from gravity.

For the rotation about the pitch axis in point P, the equations of motion are:

$$\frac{J^{(\mathrm{P})}}{l_\mathrm{a}^2}\ddot{x}_\mathrm{a} = x_\mathrm{a}c_x + c_\mathrm{i}\Delta i - \frac{M_\mathrm{g}}{l_\mathrm{a}} = -d_\mathrm{aim}\dot{x}_\mathrm{a} + c_\mathrm{aim}(x_\mathrm{ref} - x_\mathrm{a}). \tag{4.3}$$

This yields a function for the control current Δi:

$$\Delta i = -\frac{d_\mathrm{aim}}{c_\mathrm{i}}\dot{x}_\mathrm{a} + \frac{c_\mathrm{aim}}{c_\mathrm{i}}(x_\mathrm{ref} - x_\mathrm{a}) - \frac{c_x}{c_\mathrm{i}}x_\mathrm{a} + \frac{M_\mathrm{g}}{l_\mathrm{a}c_\mathrm{i}}. \tag{4.4}$$

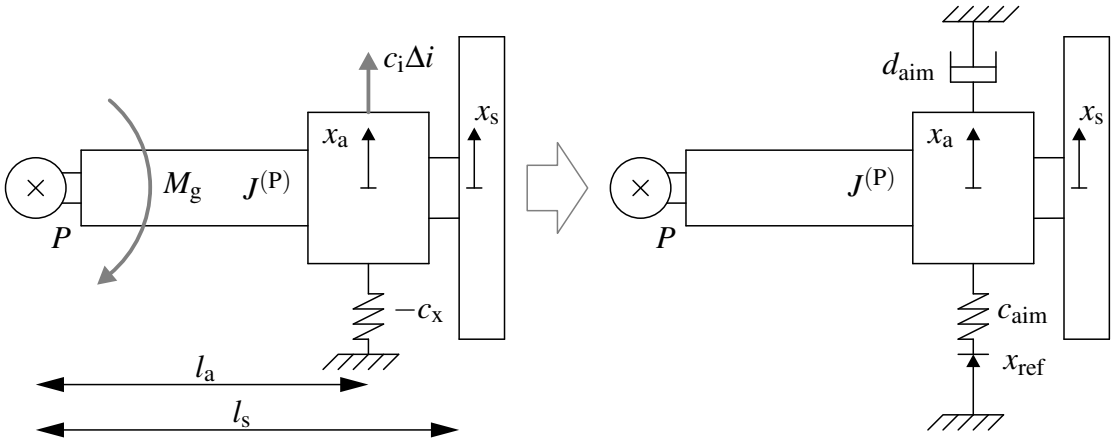

Figure 4.9: Simplified schematic of AMB prototype with inherent unstable characteristics (left) and intended properties with control (right)

Refer to equation (2.8) for c_x at the point $x = 0$. c_{aim} should be in the same range, as explained before. c_{i} results directly from equation (2.7). Both constants depend on the bias current, which has to be optimised in experiments.

The only quantity that is not yet defined is the damping d_{aim}. An expression in terms of the Lehr's damping ratio would allow a more intuitive adjustment and it would avoid a number of trial experiments. With $x_{\text{ref}} = 0$ equation (4.3) can be converted into a homogeneous differential equation of order 2 with undamped angular frequency ω_0 and Lehr's damping ratio D:

$$\frac{J^{(\text{P})}}{l_{\text{a}}^2 c_{\text{aim}}}\ddot{x}_{\text{a}} + \frac{d_{\text{aim}}}{c_{\text{aim}}}\dot{x}_{\text{a}} + x_{\text{a}} = 0 = \frac{1}{\omega_0^2}\ddot{x} + \frac{2D}{\omega_0}\dot{x} + x. \tag{4.5}$$

Comparing the coefficients leads to

$$d_{\text{aim}} = \frac{2D}{l_{\text{a}}}\sqrt{J^{(\text{P})} c_{\text{aim}}} \quad \text{and} \quad \omega_0 = l_{\text{a}}\sqrt{\frac{c_{\text{aim}}}{J^{(\text{P})}}} \tag{4.6}$$

with $l_{\text{a}} = 0.492\,\text{m}$, $l_{\text{s}} = 0.610\,\text{m}$ and $J^{(\text{P})} = 5.042\,\text{kg}\cdot\text{m}^2$. Figure 4.10 shows the resulting

closed loop control circuit diagram for the x_a movement and the orthogonal y_a diagram would look similar. The mass compensation is replaced by an integrator as a more universal and accurate solution and the differentiation is terminated by a pole at 600 Hz.

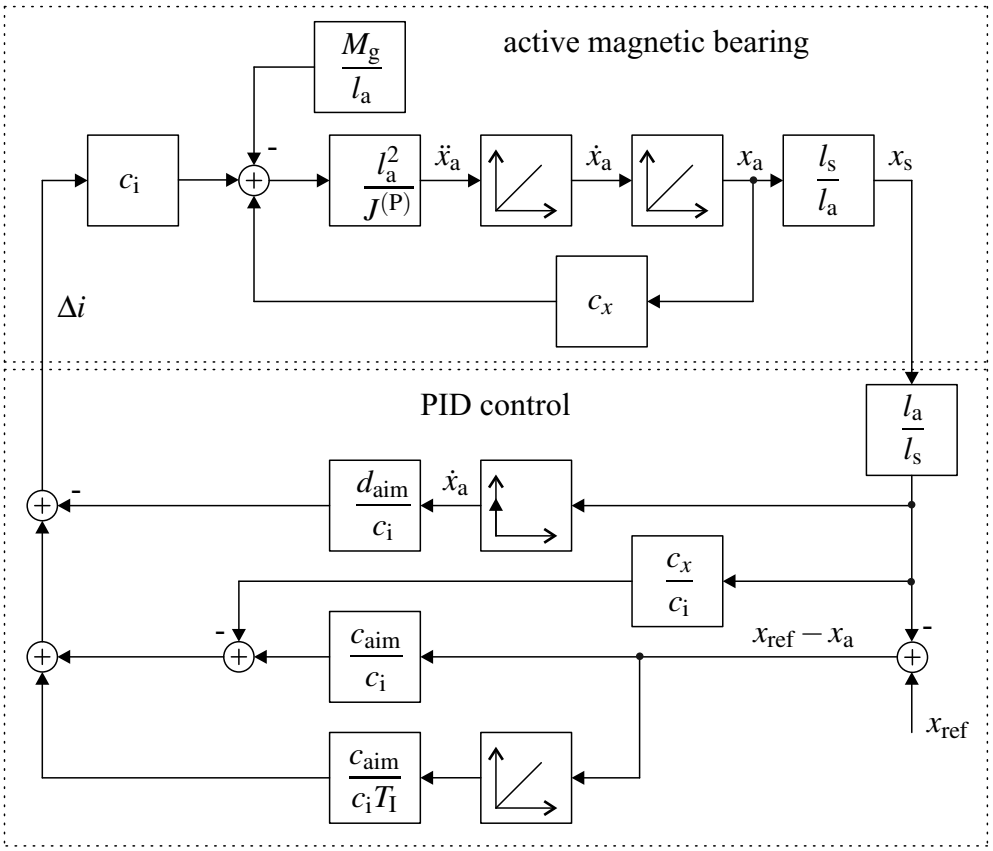

Figure 4.10: Block diagram of AMB prototype and PID control

Chapter 5

Results

In chapter 4 universal arrangements and procedures are described briefly. Further explanations of the experiments build up on them. Throughout this chapter sensor noise levels and closed loop position uncertainties play an important role. Common phrases are also jitter [32], accuracy [125], positioning accuracy [100] resolution [70], positioning resolution [43] or asynchronous radial error motion (AREM) [50]. Here, these words are used interchangeably.

5.1 Encoder scale grating results

Following the branching procedure described in section 4.1.3 the first set of experiments deals with the 200 µm profile (c) in figure 4.5 (p. 89). The subsequent experimental procedure depends on the results of these experiments.

5.1.1 Scale for LIDA 28 scanning head

Profile (c) has been machined as described in section 4.1.2 and an image produced on an optical microscope is shown in figure 5.1. The left image shows part of the surface

and a scale bar. It can be seen that the black and bright lines are clearly visible, but the aluminium looks dirty and has scratches in the direction of the grooves. Chippings of the black paint may have been smeared over the surface in the last cutting run. Because the inhomogeneities in the black fields are not visible in image a, image b has been recorded with higher illumination. The two images also show that the ratio of dark and bright is not exactly 1:1, but with 87 µm : 113 µm close to the target. Straightness errors of the bright to dark transitions are bounded between the two green lines in image b, which are 3.2 µm apart.

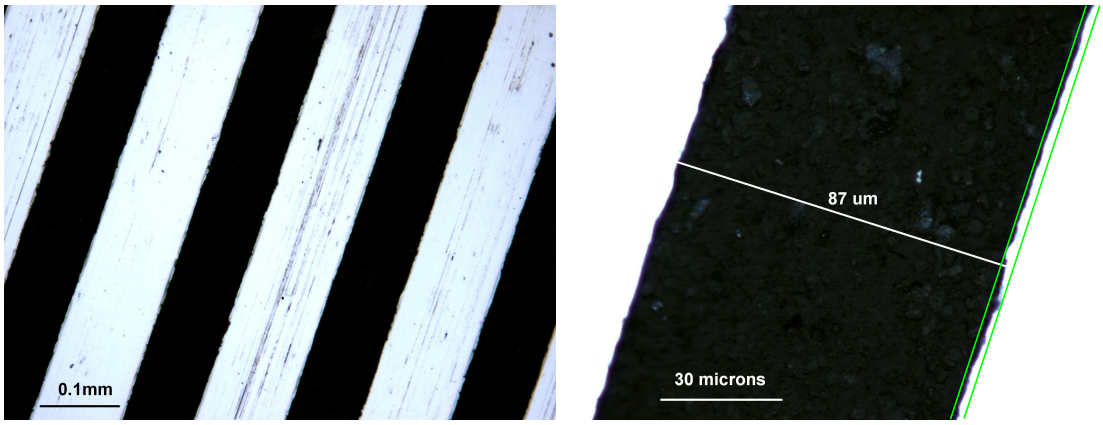

(a) Impurities on aluminium surfaces, 10x lens (b) Black line only, 50x lens

Figure 5.1: Microscope images of the machined grating of type (c) in figure 4.5

Next, the scale is tested with the LIDA 28 scanning head as explained in section 4.1.2. From the two analogue output signals of the encoder a Lissajous figure is created for one scale rotation at 60 rpm and 300 µm run-out, see figure 5.2. The mean diameter over one rotation is 0.976 V when the alignment is optimal. The status indicator LED of the LIDA 28 shows that the amplitude is in the valid range of 0.75 V to 1.25 V [24]. This range is not exceeded at any scale angle. Because the 300 µm movement is more than the grating period of 200 µm, functionality over the entire signal period is also proven. An ideal circle is displayed as a reference that has been optimized by means of nonlinear least-squares

curve-fitting (function lsqnonlin in Matlab) with variable radius and centre point. The centre point of the circle is $(-0.011\,\mathrm{V}, -0.0021\,\mathrm{V})$, which is close enough to the origin to be neglected. Signal *b* seems to be a bit larger in average, but that is not compensated either.

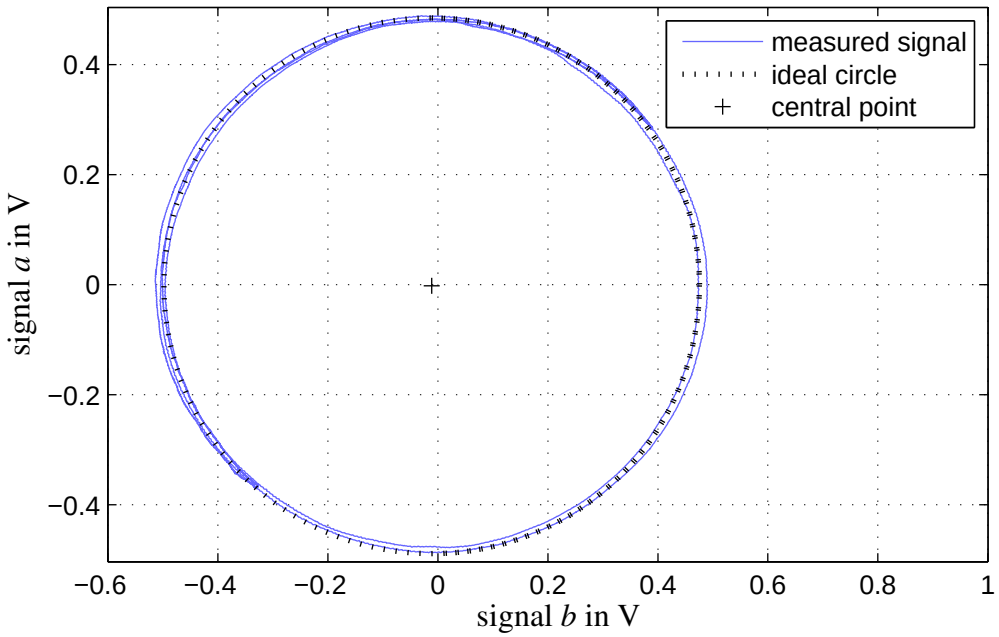

Figure 5.2: Lissajous recorded with grating (c)

As a next step the measurement noise propagation is analysed. The noise of the Speedgoat IO106 ADCs is specified as 500 µV RMS in single-ended operation for all ranges and 1 mV RMS for differential operation [109], which means 128 µV RMS, respectively 255 µV RMS when the sensor amplifier with a gain of 3.92 is considered. Measurements with grounded analogue inputs have confirmed 481 µV RMS single-ended and 630 µV RMS in differential mode. Because the noise is lower in single-ended operation and it occupies less input pins, all the subsequent experiments of section 5.1 are conducted in single-ended fashion.

Table 5.1 lists the noise of different components working in a chain. For the first two rows the RMS position value is calculated with equation (3.13) (p. 59) and the known peak-to-peak signal amplitude of 0.976 V and the peak-to-peak value with equation (3.15). For the signal angle the worst case is assumed. The standard deviations refer to the RMS values and result from five subsequent measurements over 7 s each. For the peak-to-peak values five separate values have been averaged, also recorded over 7 s. Without the sensor amplifier (figure 4.4) the ADC noise would be 3.92 times more, which proves the efficacy of this circuit. Sensor amplifier and encoder reading head together constitute only a minor influence on the noise. Engaging the scale as shown in figure 4.2 raises the noise, which could be related to vibrations of the encoder fixture and the machine bearings and to non-linearities in the reading head.

Table 5.1: Measured noise development in encoder measurements with 200 µm grating period, unit nm

Components	RMS	Peak-to-peak	Standard deviation of RMS
ADC only, single-ended	7.83	91	0.031
+ amplifier + encoder, no scale, dark room	9.90	136	0.08
+ scale (c), no rotation	13.8	139	0.036

It is also of interest how much noise is caused by scale roundness errors when the spindle is rotating. However, experiments with rotating scale are more difficult to evaluate because it cannot be distinguished between run-out and deviations from roundness easily, when the experiment is done as in figure 4.3. It is virtually impossible to rotate a scale on the machine chuck without run-out. If the standard deviation of the position measurement was used as an indicator for the sensor resolution without further signal processing, the result would be highly dependent on this run-out. As a more universal

procedure a run-out of 2 µm is allowed and a sinusoidal curve[1] is matched with the measurements to identify and subtract the exact run-out of the disc (eccentricity separation). The parameters optimized by the Matlab function lsqnonlin are amplitude, frequency, phase and offset.

An exemplary result of the curve fitting at 60 rpm speed is shown in figure 5.3. The difference between the two lines can be attributed to scale imperfections. For each revolution an independent curve is fitted, so that the variability can be evaluated. The errors show a highly repeatable pattern, which means that they are caused by scale imperfections or synchronous errors of the machine bearing, but not by electrical interference. It is time-consuming to adjust a tight run-out of 2 µm but with a higher eccentricity the subdivisional error of the encoder and the rotary speed control would play a more significant role. The deviation in RMS between the sinusoidal curve and the measurement is plotted for different rotational velocities in appendix D, figure D.1. Speed dependent fluctuations are regarded as measurement errors, presumably related to the speed control.

In order to eliminate the effect of imperfections in the rotary speed control completely, the scale roundness error is measured in static experiments, too. The spindle is rotated in steps of 10° and at each step the position is averaged over 1 s. Then the measurements are processed as described above. This experiment is repeated five times in different radial positions with 200 µm step between adjacent positions. The result for profile (c) and encoder LIDA 28 is shown in figure 5.4. An error bar has the length of two times the sample standard deviation at that point. From this experiment a median roundness error of 98.3 nm RMS results and the standard deviation over five experiments is 10.9 nm.

[1] The vertical undulation of a perfectly round groove with run-out is not exactly sinusoidal, but that is neglected here.

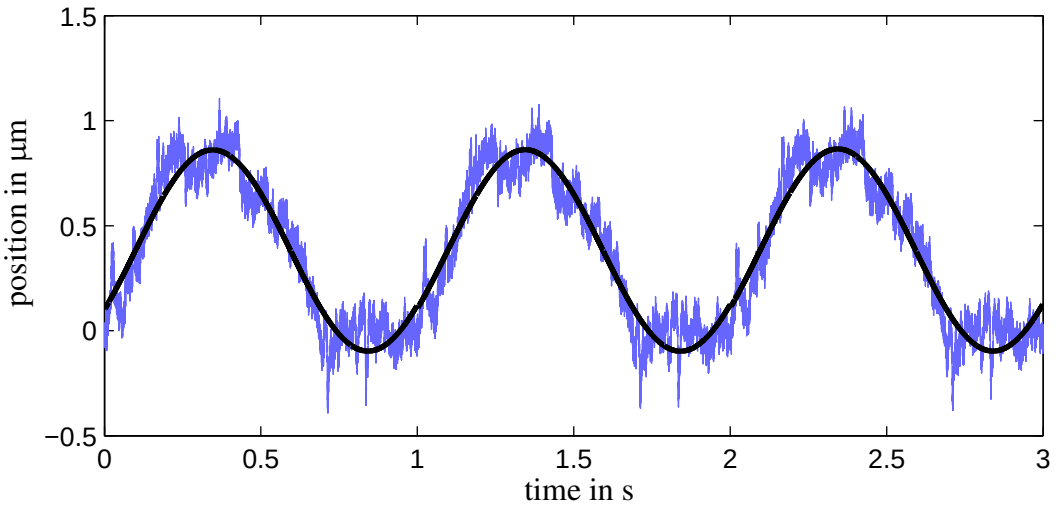

Figure 5.3: Position measurement with LIDA 28 and sinusoidal approximation of real movement

Together with the noise at non-rotating spindle the total noise can be calculated [50]:

$$\sqrt{13.8^2 + 98.3^2}\,\mathrm{nm_{RMS}} = 99.3\,\mathrm{nm_{RMS}} \tag{5.1}$$

Comparing this result to the experiments with actually rotating scale in figure D.1 it can be judged that the agreement is satisfactory.

In conclusion, a procedure has been found to fabricate amplitude gratings for the LIDA 28 with high contrast in spite of the microscopic imperfections of the scale. The contrast is high enough to meet the encoder specifications and it seems superfluous to produce profiles (a) and (b), which would be very time-consuming. Instead it has been decided to proceed with the 20 µm scales, i.e. the second row in figure 4.5 (p. 89).

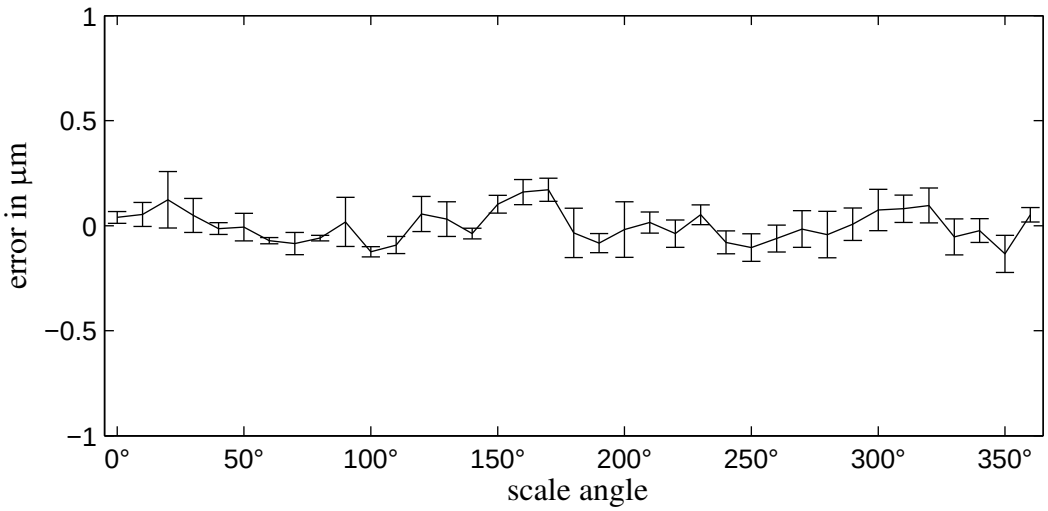

Figure 5.4: Scale roundness error of profile (c)

5.1.2 Scales for LIDA 48 scanning head

Scales complying with procedures (d), (e) and (f) have been cut. Microscope pictures of scale (d) are shown in figure 5.5. The microscope is a XL30SFEG field emission scanning electron microscope (FESEM) from Philips. Pictures taken with optical microscopes looked unfocussed because of the shallow depth of field of the microscope. The pointed tool has cut triangular grooves with bright slopes into the reflective surface that appears dark in the images. Straightness errors of the tool tip are not visible, but burr has piled up on the margins leaving only narrow lines of the original surface. The grooves are not 10 µm wide as intended, but approximately 3 µm wider as can be seen from the dimensions in figure 5.5, a.

Figure 5.6 shows the turning results of profiles (e) and (f). The left image is captured with the same FESEM and shows the inner groove of profile (e) at the bottom of the image. This is the smallest groove and it has been cut last. The bottom of this groove appears dark in the image and it looks plain and straight. The other grooves are visible

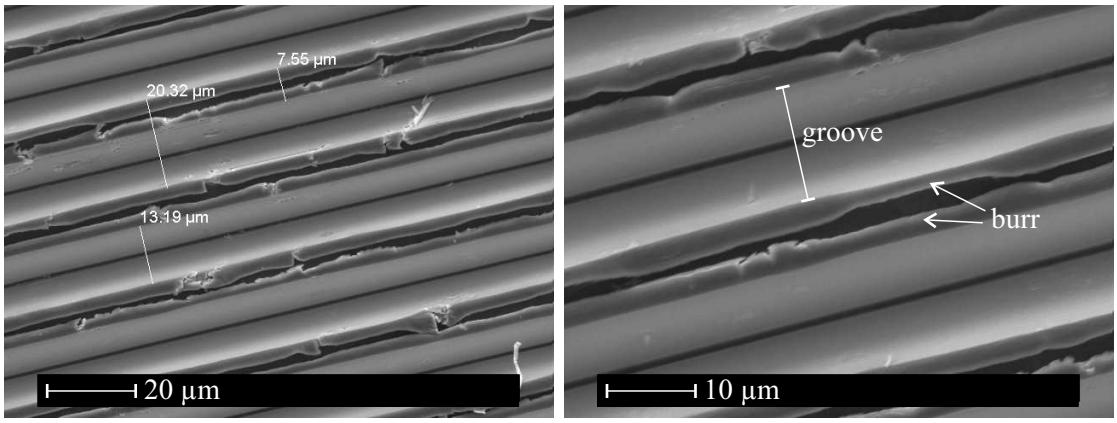

(a) Magnification 1,000 (b) Magnification 2,000

Figure 5.5: FESEM images of the machined grating of type (d) in figure 4.5

but they don't look as intended. It seems that the walls between the grooves are pushed aside by the machining force and while cutting one groove they are squeezed into the previous one. The expectation is a low contrast in the imaging scanning principle.

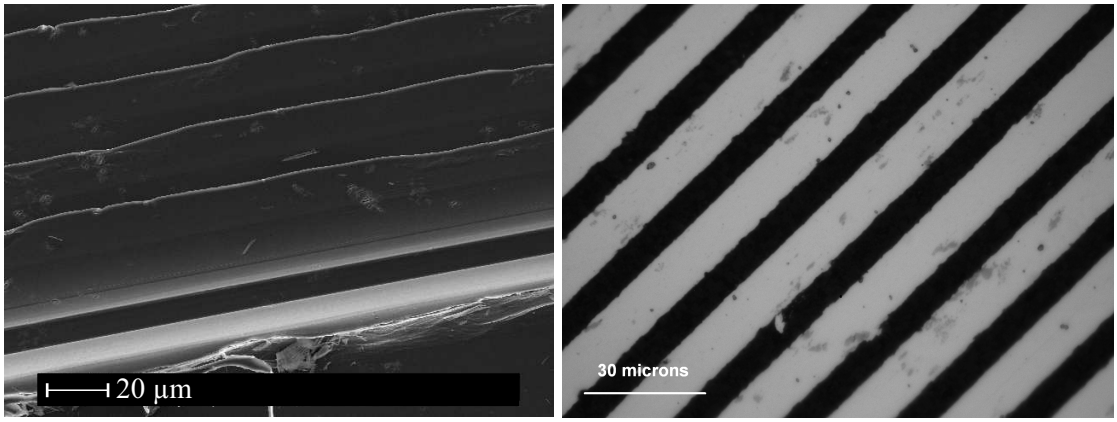

(a) FESEM image of profile (e), inner edge (b) Microscope image of profile (f)

Figure 5.6: Images of machined gratings (e) and (f)

The picture of profile (f) in figure 5.6 is taken in the middle of the featured band with an optical microscope. It can be seen that the cutting procedure has worked and that clear dark and bright lines with only minor defects have been created. The bright lines are 1 µm

too wide.

In table 5.2 the output voltages are compared. Profile (c) is also listed. For these numbers five rotations at $1.5 \cdot p$ run-out have been recorded and the rotations are evaluated individually. Minimum, average and maximum are averaged over the five rotations and the differences between the measurements are represented in the last column (only for the average). The diameter is calculated for each time step by multiplying the distance of a measured point in the $a-b$ plane from the origin by two.

Table 5.2: Comparison of the Lissajous diameter M in V for different scales

Profile identifier	Min	Average	Max	Standard deviation of average
(c)	0.927	0.977	1.028	26.7µ
(d)	0.379	0.413	0.442	45.5µ
(e)	0.052	0.054	0.056	119.0µ
(f)	0.723	0.765	0.818	127.0µ

As can be expected from figure 5.6, a, profile (e) shows almost no contrast, evident in the small average Lissajous diameter in table 5.2. Profile (d) does not meet the specifications of the encoder system, but 0.413 V is close to the minimum of 0.75 V. The two scales with paint meet the specification.

Figure 5.7 shows the Lissajous figure recorded with profile (f) and the LIDA 48 reading head, because it is the best one with 20 µm grating period. The speed of rotation of the scale is 60 rpm and the run-out is 30 µm. With 30 µm run-out more than one whole signal period is captured. Analogously to figure 5.2 an ideal circle with the mean diameter is plotted as a reference. Its centre point is close to the origin and the signals are evaluated without bias compensation.

Table 5.3 is the counterpart to table 5.1. It shows the influence of noise of the instruments that are involved in the measurement. Profile (d) works reliably and allows low noise measurements, but the signal amplitude is not high enough to fulfil the require-

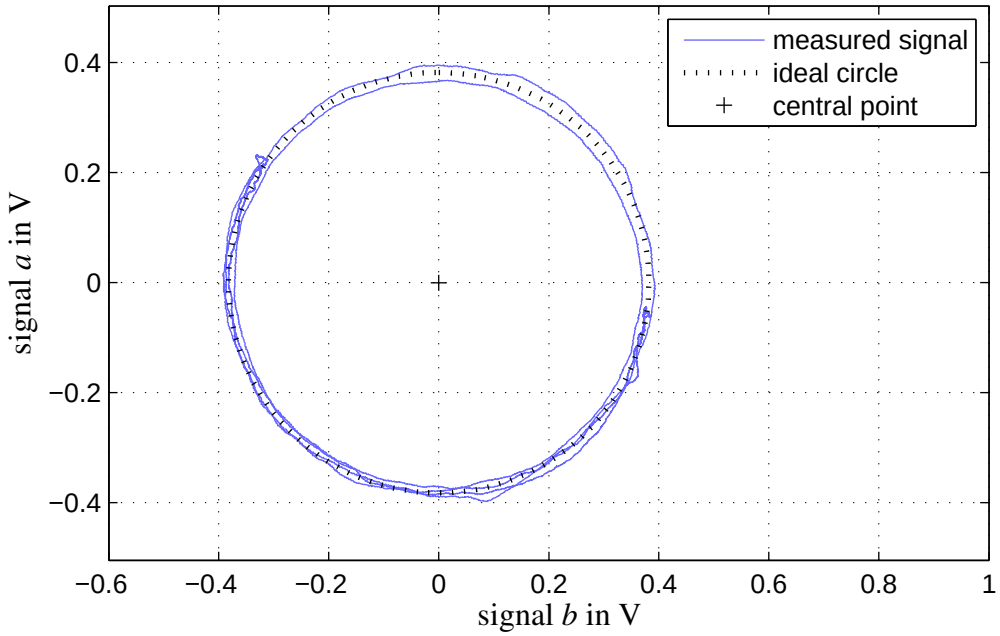

Figure 5.7: Lissajous figure for profile (f) and best fit of circle with variable radius and centre point

ments. Also, the noise is approximately two times higher than that of (f). Profile (e) simply does not work, as can be derived from table 5.2. The Lissajous does not even surround the origin and position measurements are not possible without bias compensation. Profile (f) shows the lowest noise of 3.37 nm in the static experiment and the highest peak-to-peak amplitude. Hence, it has the highest merit of the 20 µm scales and the following experiments deal with (c) and (f) only. They are the best achievements for each grating period.

For profile (f) the position measurement during three rotations of the scale is displayed in figure 5.8. In comparison with figure 5.3 the signal looks less noisy. In order to give a quantitative estimate for the scale roundness error, static measurements are performed in figure 5.9. It has been recorded in the same way as explained above, i.e. static measurements in 10° steps around the circumference and five repetitions of the experiment in five

Table 5.3: Comparison of sensor noise for the three 20 µm scales, unit: nm. The three values are RMS over 7 s, standard deviation of the RMS over five experiments and the peak-to-peak value over 7 s.

Components	Profile (d)	Profile (e)	Profile (f)
ADC only, single-ended	1.90; 0.0075; 21.9	14.5; 0.057; 167	1.02; 0.004; 11.8
+amplifier+encoder, no scale, dark room	3.47; 0.043; 43.8	26.6; 0.332; 335	1.87; 0.023; 23.6
+ scale, no rotation	6.37; 0.081; 58.9	19.6; 0.185; 189	3.37; 0.148; 29.9

different radial positions (200 µm appart). The spindle run-out is accounted for by a sine curve fitting.

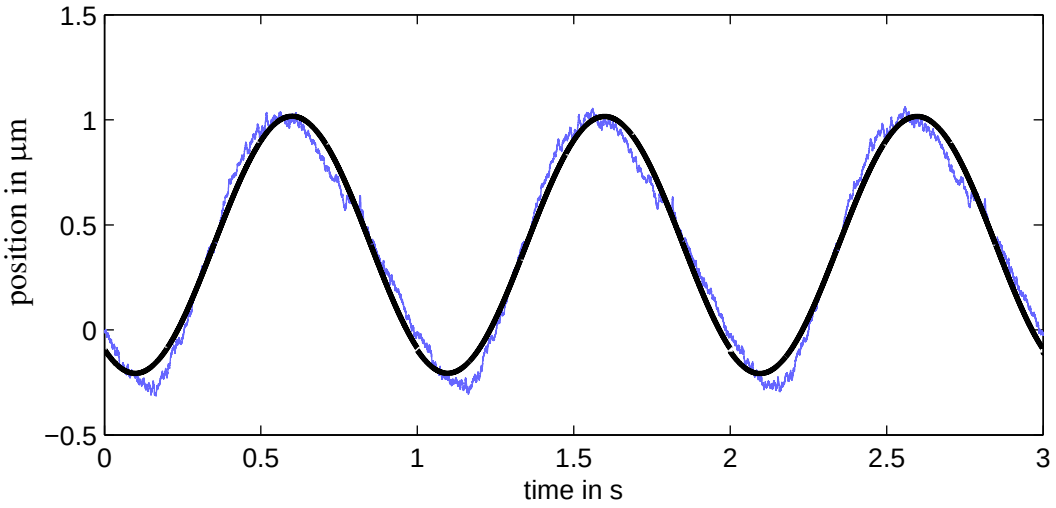

Figure 5.8: Position measurement with LIDA 48 and sinusoidal approximation of real movement

From these experiments an estimate of 76 nm RMS, standard deviation 1.55 nm can be calculated for the roundness error. Results with actually rotating spindle look similar, see figure D.2. There is a striking undulation at two times the rotational speed in figure 5.9, or in other words an ellipse has been measured and not a circle. This could be related to cylindricity errors in the machine bearing. These can be magnified depending on the

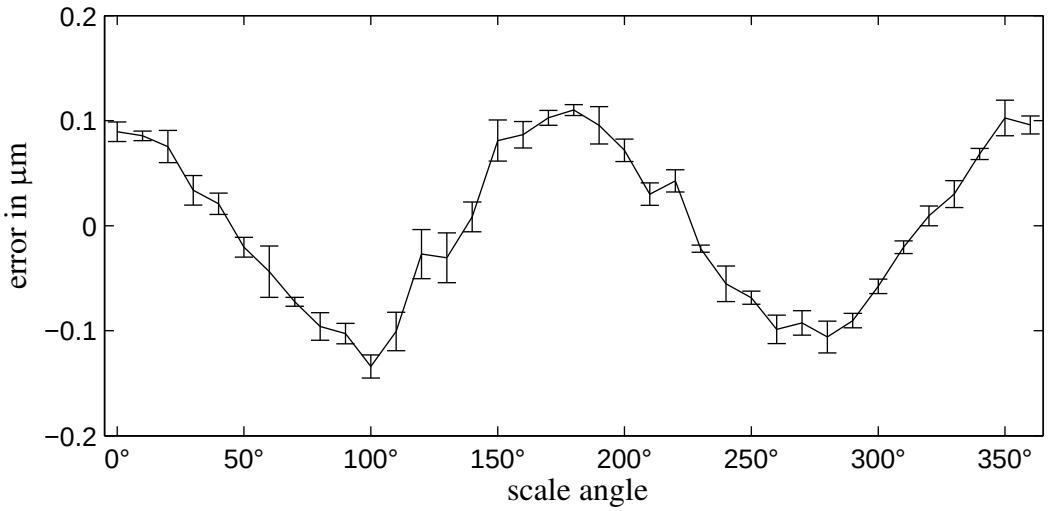

Figure 5.9: Scale roundness error of profile (f)

clamping orientation of the disc for cutting and later for testing.

As the error bars in figure 5.9 are short and the roundness errors seem highly repeatable it is obvious to compensate them. This is done in figure 5.10 by subtracting the position that is measured in a sixth static experiment from each of the other measurements. With this procedure no curve fitting is required and the sixth experiment acts as a calibration measurement. The remaining error is 15.8 nm RMS and its standard deviation is 9.3 nm. The peak-to-peak value is 120.5 nm. If the measurement had been undertaken five times at the same radial position, the calibration error and the length of the error bars would be much shorter. However, this experiment demonstrates what can practically be achieved by a simple calibration procedure in spite of radial movements that are not explicitly calibrated.

5.1.3 Deviations per signal period

Following this separate treatment of 20 µm and 200 µm grating period, some chosen characteristics are now demonstrated for both together. For the deviations per signal period

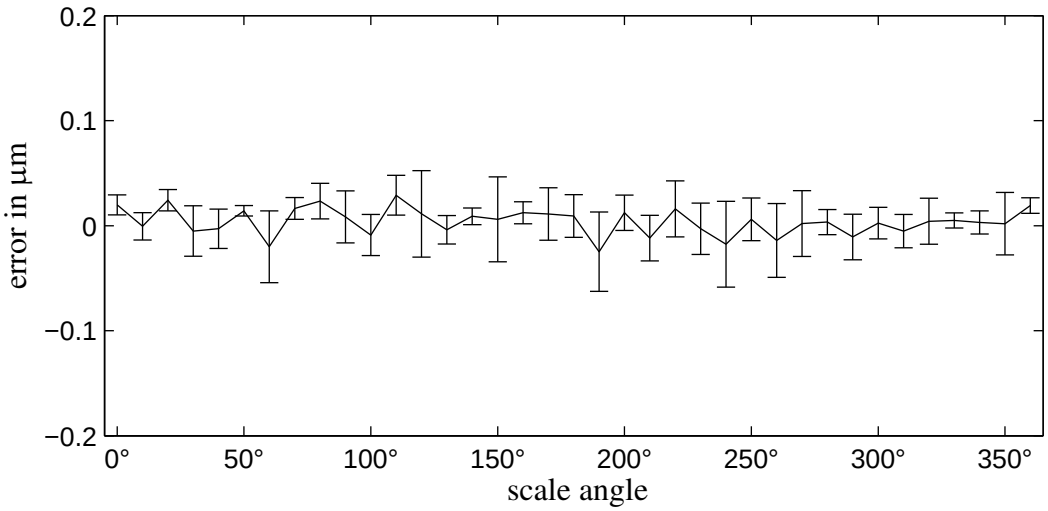

Figure 5.10: Scale straightness error of profile (f) after subtraction of known roundness error

or also called sub-divisional error the reading head is mounted as shown in figure 4.3. It is moved in 20 steps in radial direction and at each step the position is averaged over $10,000$ measurements. The overall movement is one signal period, which equals 360°. This procedure is repeated for five randomly chosen angles of the scale to analyse the repeatability.

The result is shown in figure 5.11 for LIDA 28 (200 µm) and for LIDA 48 (20 µm). For LIDA 28 the measured range of the error is $-0.60\,\mu\text{m}...1.27\,\mu\text{m}$ and for LIDA 48 it is $-35\,\text{nm}...44.8\,\text{nm}$. Thus, they both fulfil the specification of $1\,\% \cdot p$ as guaranteed by the company Heidenhain [24]. Because of the high repeatability even at different angles the sub-divisional error could possibly be improved by means of calibration measurements.

5.1.4 The influence of a lateral shaft movement

As explained before the output signal of the encoders should degrade when the encoder reading head is moved in lateral direction, refer to figure 3.6. In this experiment the

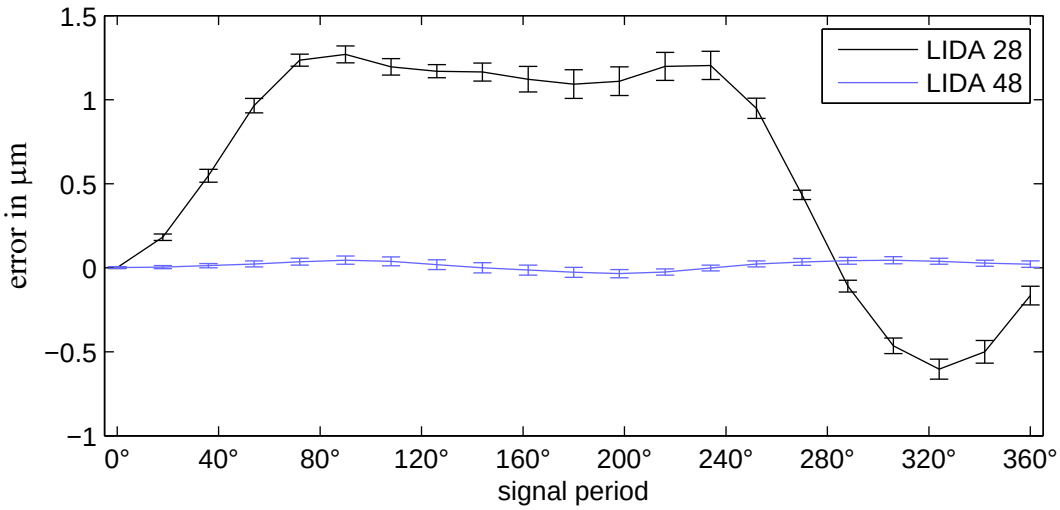

Figure 5.11: Deviations per signal period measured for LIDA 28 and profile (c) and for LIDA 48 and profile (f), recorded at five different scale angles

encoder is mounted as in figure 4.2 and it is moved more than 4 mm in lateral direction along the scale while the signal amplitude is recorded. The machine spindle rotates at 1,000 rpm. After each rotation the signal amplitude is averaged over the last 360°, so that material inhomogeneities do not influence the result.

Figure 5.12 comprises measurements for LIDA 28 and profile (c) as a 200 µm system and LIDA 48 together with profile (f) representing the 20 µm encoders. It is believed that the effect will be the same for other cutting profiles as long as the reading head is the same.

Apart from the fact that the amplitude of profile (f) is lower than that of profile (c) it can be seen that the 20 µm scale is more sensitive to angular misalignment errors. The analytical model described by equation (3.18) is also plotted for both grating periods. Appendix E describes how the width of the reticle window has been measured. From this width and the known grating period the unknown constant m can be determined. It is approximately 55 for LIDA 28 and 375 for LIDA 48. The window length is optimized

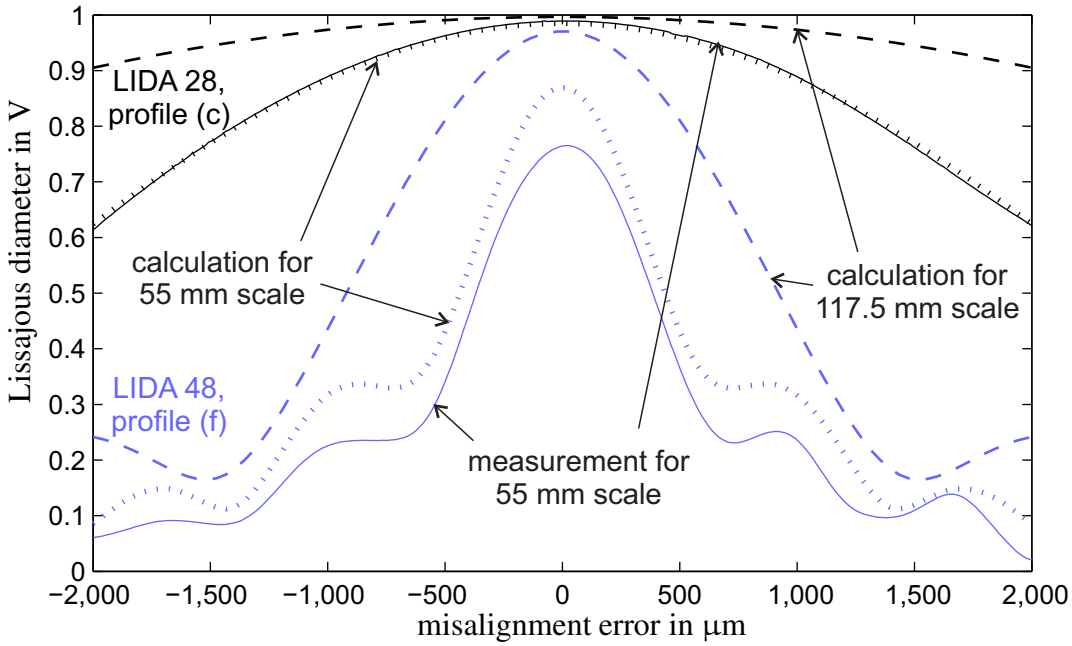

Figure 5.12: Comparison of the misalignment effect for profiles (c) and (f). (c) with LIDA 28: black; (f) with LIDA 48: blue. The scale size refers to the medium scale radius, which is 55 mm in the case of the test discs and 117.5 mm in the magnetic bearing prototype.

on the basis of the experimental data and the contrast of the ideal, straight scale is set to $1V_{PP}$. Especially for LIDA 28 there is a good agreement of theory and measurement. The difference in amplitude at the smaller grating period could be related to the non-ideal division ratio, see figure 5.6, b.

For the magnetic bearing the observed effect is important and it is a disadvantage of the smaller grating period that the alignment shows a stronger influence. The dashed lines are estimates for the behaviour of the larger scale in the magnetic bearing prototype based on calculation (3.18) (p. 61). Because of the wider radius of curvature in the magnetic bearing scale the range of movement is extended.

5.1.5 Which type is to be favoured for the magnetic bearing?

Comparing 20 µm scales and 200 µm scales the following statements can be made:

- Within the scope of the experiments reported here more precise results were obtained with the best one of the 20 µm scales than with the 200 µm one.
- The highest contrast could be achieved for 200 µm.
- The LIDA 28 is more robust against angular alignment errors that determine the admissible range of movement in the AMB.
- Regarding the distance between reading head and scale wider mounting tolerances are specified for the LIDA 28, see table 3.1 (p. 57)
- The LIDA 48 is more expensive, see table 3.1

In conclusion the LIDA 28 is more robust but the LIDA 48 is more precise. Profiles (c), (d) and (f) seem precise enough to meet the requirements from section 1.2, but the assumption has to be confirmed in closed loop magnetic bearing experiments. Because the sensor resolution is the most important criterion, is has been decided to apply the smaller grating period to the magnetic bearing. It is also more interesting to find out if stable and save operation can be established in spite of the challenging tolerances. A 20 µm scale is more ambitious and a successful performance demonstration would have the higher merit. For time reasons profile (d) is employed and not profile (f).

5.2 Magnetic bearing performance evaluation

With the magnetic bearing prototype it is possible to stabilize the rotor completely with gap sensors or alternatively with encoders. Some general observations and efforts to

improve the performance are summarized first before the performance data are compared in detail.

5.2.1 Gap sensor control

For all these experiments the encoder disc and the encoders are mounted although they are not deployed. The bias current is $I_0 = 1.3\,\mathrm{A}$, which does not result in the desired stiffness but at bias currents of more than 2.1 A the magnetic bearing shows stability problems. It was necessary to support the bridge under the AMB in two points to achieve stable operation. Without these additional supports the bridge vibrates at a frequency of 103.5 Hz. The controlled stiffness always equals the inherent bearing stiffness, which is $0.41\,\mathrm{N}/\mu\mathrm{m}$ according to equation (2.8) (p. 23). With $I_0 = 1.3\,\mathrm{A}$ a range of $0.2 \leq D \leq 0.8$ shows stable operation and if not otherwise specified the experiments have been conducted with $D = 0.5$. The integrating feedback is set to $T_\mathrm{I} = 0.1\,\mathrm{s}$ and for some experiments it is disabled. Extending the integrator action to higher frequencies would increase the sensitivity to sensor noise at high frequencies [81].

The closed loop frequency response functions (FRFs) of the magnetic bearing recorded with gap sensors are shown in figure 5.13 for both directions. For the FRFs a sinusoidal excitation has been added to the reference signal, while the integrator is disabled. The excitation frequency is raised in small steps.

At low frequencies the gain is close to one in both directions although the integrator is disabled. This indicates that the magnetic circuit parameters have been identified correctly. The FRFs also show that even with the two support points there are flexible modes at 200 Hz and above. If the bandwidth is defined as the frequency where the gain is reduced to 71 % of the static gain, then the magnetic bearing has a bandwidth of 35 Hz in both directions. The bandwidth can be raised if the damper in figure 4.9 (p. 95) between

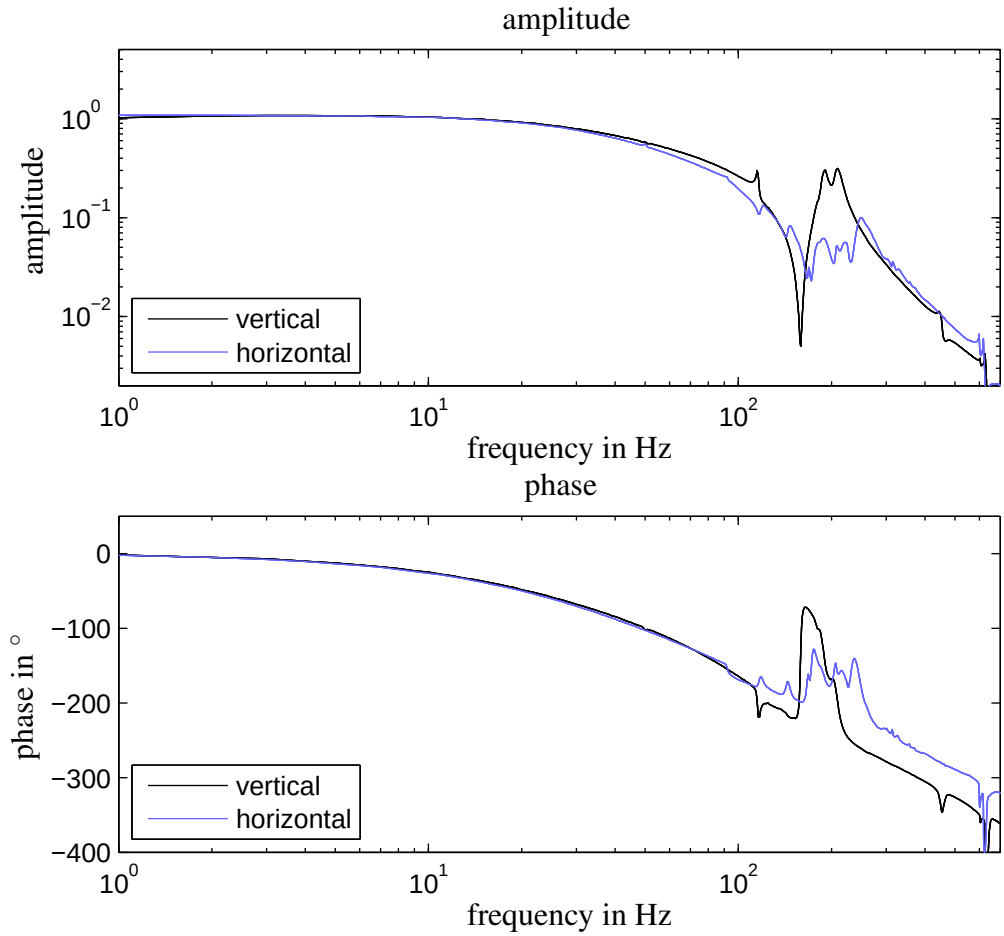

Figure 5.13: Measured closed loop frequency response function of the AMB prototype from the excitation at the reference signal to the actuator position.

the armature and the virtual frame is replaced by a damper of the same viscosity between the armature and the reference signal. With this changed control design a bandwidth of 120 Hz can be achieved in both directions as exhibited in figure 5.14. All the remaining experiments have been done as shown in figure 4.10, but for most of the experiments there is no difference because the reference signal is constant.

The left graph of figure 5.15 shows the radial error motion plot of the AMB controlled with gap sensors and without integrating feedback. x is measured with one eddy current

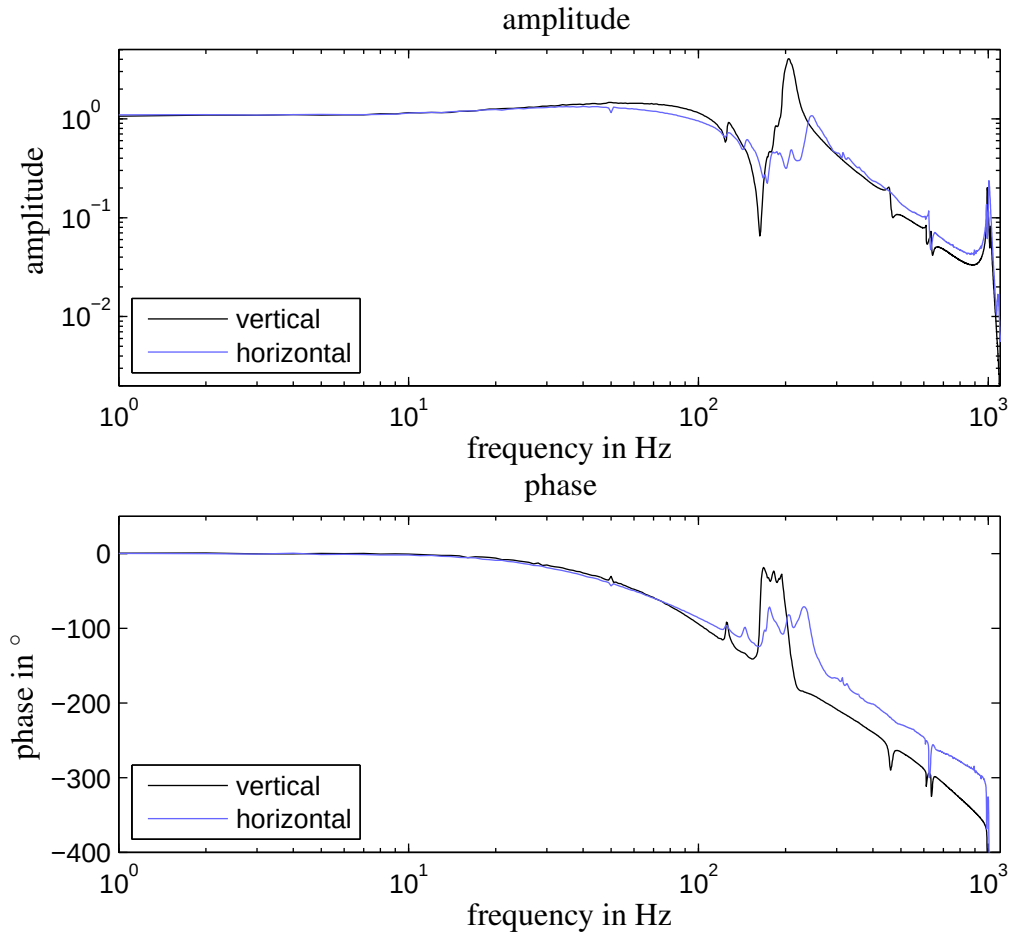

Figure 5.14: Measured closed loop frequency response function. The bandwidth is raised by the measure described in section 5.2.1.

sensor and y with one capacitive sensor. The shaft is slowly rotated by hand so that unbalance has no effect. As the integrator is disabled the resulting whirl figure does not depend visibly on the exact speed as long as it is slow. The recording starts with the shaft resting in its touch-down bearing. It rises as the stiffness and the bias current are slowly increased and then performs five rotations. Finally it returns back to the resting position. The reference value is $(-50\,\mu\text{m}, 0)^{\text{T}}$ instead of $(0,0)^{\text{T}}$ because the range of the eddy current sensor restricts the permissible vertical movement. Instead of rotating in

one point a repeatable shape with approximately 104 µm width and 105 µm height can be observed. This could be caused by misalignment errors and imperfections of the sensor target surface and the bearing rotor.

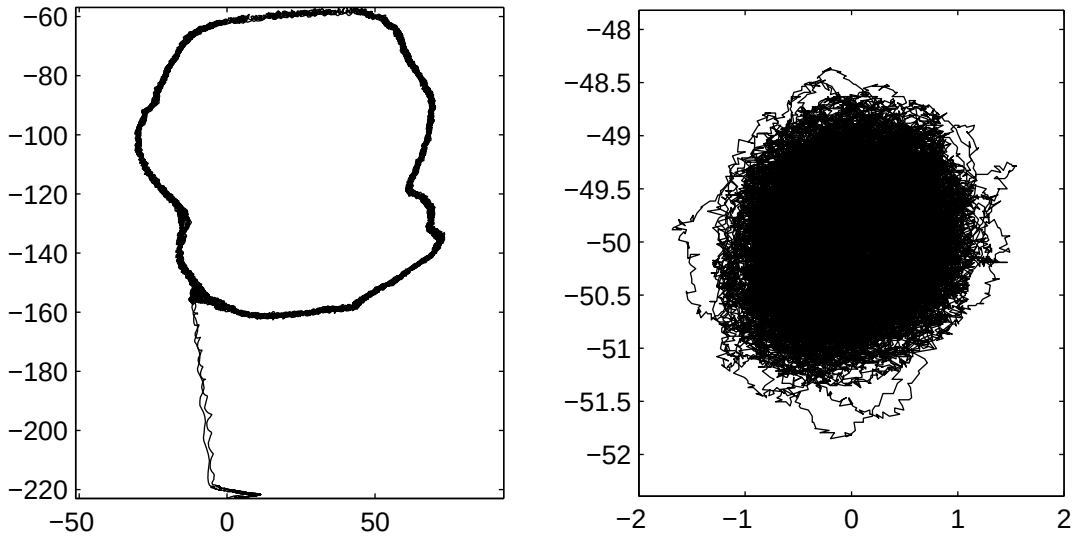

(a) Rotating

(b) Not rotating, with integrator

Figure 5.15: Whirl motion of rotating and non-rotating AMB, x and y in µm, controlled with gap sensors.

On the right of figure 5.15 seven seconds of the orbital plot for control with integrating feedback and constant orientation are shown. Under these conditions the mean position value equals the reference value, but there is still a considerable asynchronous error. Quantitative results are presented together with the encoder experiments later.

In figure 5.16 the frequency spectrum of the controlled vertical position is shown for the two different gap sensors. It has been recorded by averaging 1,000 FFTs of subsequent, overlapping time sections with active integrator. The only obvious difference between the two gap sensors is the noise level at high frequencies. There are two major peaks at 50 Hz and 226 Hz. The 226 Hz peak could be a bending mode, but the 50 Hz

peak is not related to the structure, because the frequency response function (FRF) of the AMB does not show a significant peak at this frequency, see figure 5.13. It is assumed that the 50 Hz vibration is either related to line interference on the signal paths or to the current control of the amplifiers. The exact frequency is not affected by changes to the experimental setup. Appendix F shows the spectrum of the measured shaft position while the power amplifiers are driven with a constant reference signal. The spectrum resembles figure 5.16 and the 50 Hz peak is present, too. It seems that the power amplifiers are responsible for most of the closed loop positioning noise.

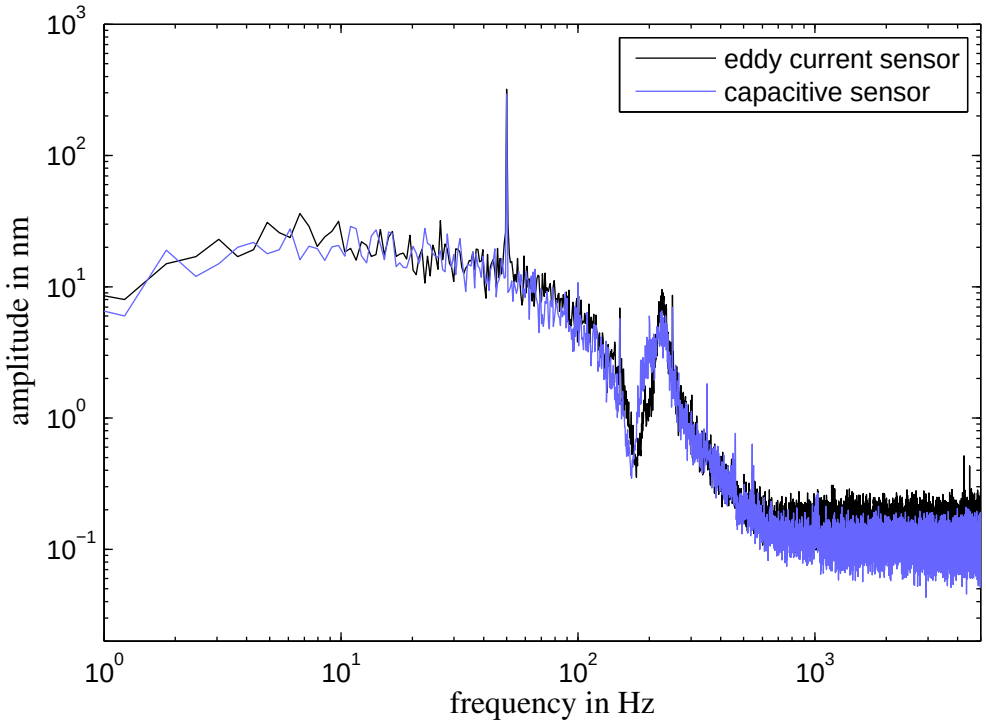

Figure 5.16: FFT of the positioning noise controlled with gap sensors

Because the 50 Hz undulation rises the resulting positioning noise significantly, the signal lines for sensors and power amplifiers have been changed to differential and the shielding inside and outside the cabinet has been treated with special care, but these mea-

sures have not changed the results. The experiments from above have been conducted after these changes had been applied.

5.2.2 Adaptive compensation of line interference

In order to reduce the 50 Hz undulation, a simple adaptive feed-forward vibration compensation (AFVC) algorithm is applied. It has been described by Shi [103] for unbalance induced vibrations and an augmentation to the multidimensional case can be found in [6]. In this thesis the derivation is not repeated and the procedure of compensating the line interference is explained only briefly.

Synchronous disturbances are to be rejected by the function $\boldsymbol{\nu}(t) = [\nu_x, \nu_y]$, which is added to the reference signal $\boldsymbol{x}_{\text{ref}}$. All signals are treated as vectors with one entry for x and one for y. This compensation function is a superposition of a sine wave and a cosine wave with the known frequency of the disturbance, here $\Omega = 2\pi \cdot 50\,\text{Hz}$. The function $\boldsymbol{\nu}$ is calculated in each step k:

$$\boldsymbol{\nu}(k) = (\boldsymbol{\Phi}(k, \varphi_x = 0, \varphi_y = 0))^{\mathrm{T}} \cdot \boldsymbol{\Theta}_{\mathrm{c}}(k). \tag{5.2}$$

$\boldsymbol{\Theta}_{\mathrm{c}}(k) \in \Re^{4\times 1}$ comprises the estimated amplitudes and $\boldsymbol{\Phi}(k, \varphi_x, \varphi_y)$ is defined as:

$$\boldsymbol{\Phi}(k, \varphi_x, \varphi_y) = \begin{pmatrix} \sin(k\Omega T + \varphi_x) & 0 \\ \cos(k\Omega T + \varphi_x) & 0 \\ 0 & \sin(k\Omega T + \varphi_y) \\ 0 & \cos(k\Omega T + \varphi_y) \end{pmatrix} \tag{5.3}$$

with the sampling time T. $\boldsymbol{\Theta}_{\mathrm{c}}(k)$ is updated in each step according to the position feed-

back $\boldsymbol{x}_\mathrm{a} - \boldsymbol{x}_\mathrm{ref}$, also with x and y component:

$$\boldsymbol{\Theta}_\mathrm{c}(k) = \boldsymbol{\Theta}_\mathrm{c}(k-1) - \boldsymbol{\gamma} \cdot \boldsymbol{\Phi}(k, \varphi_x, \varphi_y)(\boldsymbol{x}_\mathrm{a}(k) - \boldsymbol{x}_\mathrm{ref}(k)). \tag{5.4}$$

The parameter γ must be small enough not to influence the dynamics of the system considerably [103, 6].

φ_x and φ_y constitute the phase of the closed loop transfer function from the reference signal to the position at 50 Hz. Often they are neglected [103, 6], but initial experiments without consideration of the phase lag showed stability problems of the adaptation in this case. From figure 5.13 they can be determined for $D = 0.5$ and the same can be done for other damping ratios, see table 5.4.

Table 5.4: Phase of the frequency response function at 50 Hz for x and y with respect to the damping

	$D = 0.3$	$D = 0.5$	$D = 0.7$
φ_x	$-111°$	$-100°$	$-95°$
φ_y	$-114°$	$-101°$	$-97°$

Figure 5.17 shows how the adaptation parameters, which represent $\boldsymbol{\Theta}_\mathrm{c}$, converge, after they have been initialized to 0. At the beginning they are unsteady because the rotor is far away from the reference position. As soon as the integrator has established the steady state of the armature they stabilize. Remaining undulations of the parameters at a low frequency can be related to inaccuracies of the net frequency and consequently binaural beat. Repetitions of the experiment differ in the exact beat frequency.

The resulting spectrum of the positioning noise is shown in figure 5.18, again with active integrator. It can be seen that the peak at 50 Hz has been reduced, but it does not always work as good as in this recording. In each time step a maximum of 22 µs out of 100 µs sampling interval is needed for data acquisition, calculation and analogue output

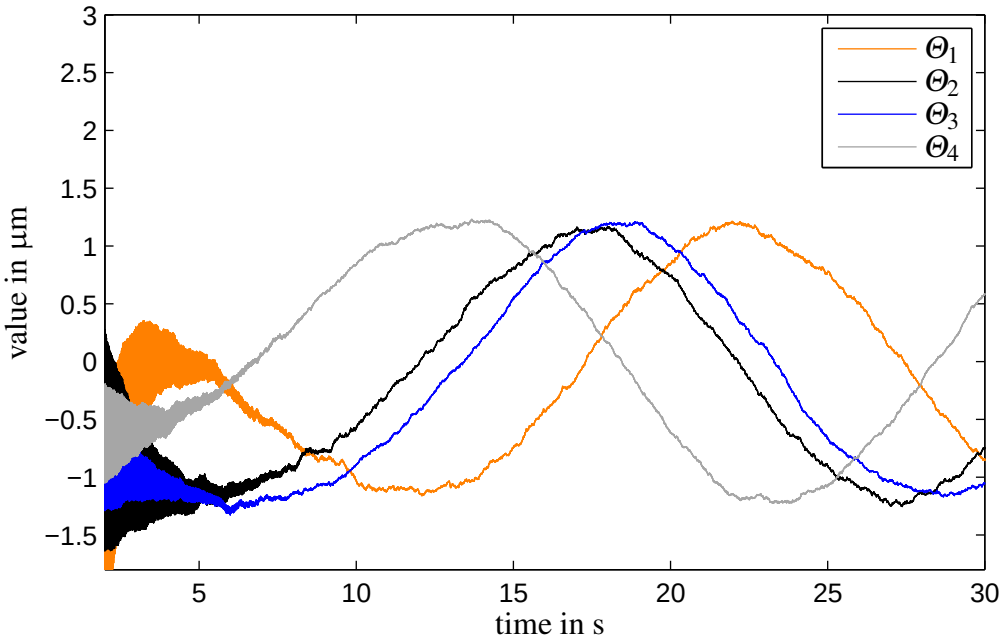

Figure 5.17: Transients of the AFVC adaptation parameters

for two degrees of freedom.

Figure 5.19 shows the whirl motion with AFVC and non-rotating shaft for different damping ratios. It has been recorded over seven seconds with the eddy current sensor measuring the vertical position and the capacitive sensor measuring the horizontal position. The left graph can be compared directly to the right graph of figure 5.15 to evaluate the efficacy of the AFVC. It works and reduces the overall positioning uncertainty. For $D = 0.7$ the result is even better. Quantitative figures are stated below.

5.2.3 Magnetic bearing controlled with encoders

For the large scale encoder disc, profile (d) has been cut into an aluminium disc with 300 mm diameter. The surface of interest had to be sandblasted and then coated with 100 µm electroless nickel, because it was not possible to replicate the features in alu-

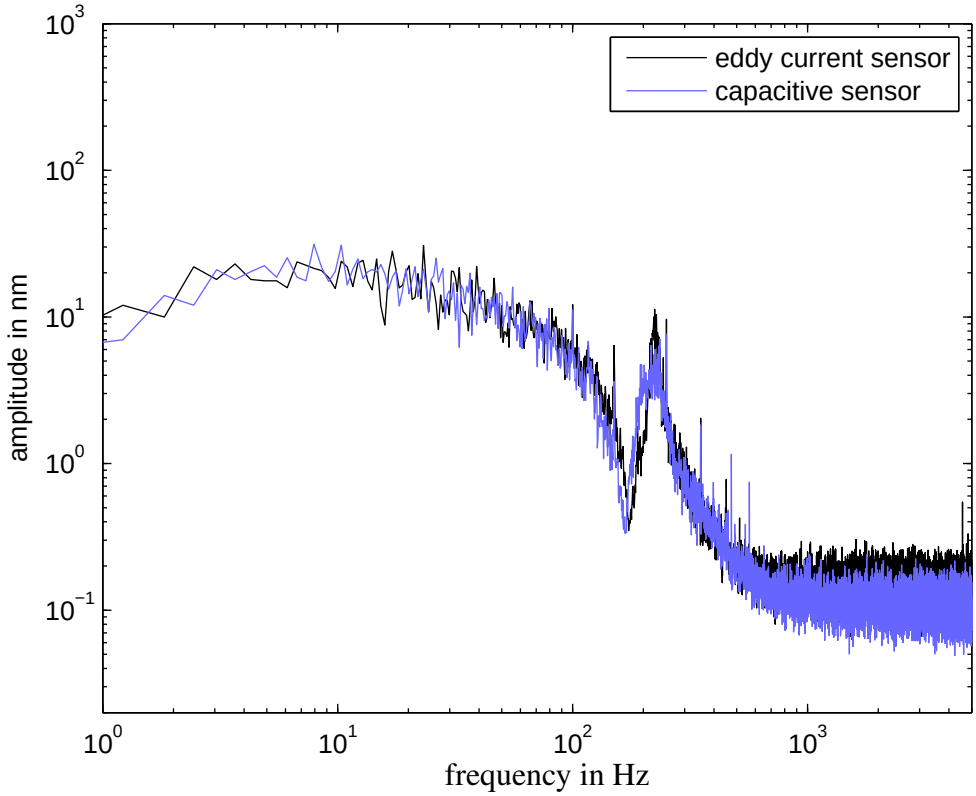

Figure 5.18: FFT of position noise with gap sensors and active AFVC

minium. While this worked with the smaller test disc, there were problems with the grain structure of the bigger disc (not with the tool mileage). 53° has been chosen for the included angle of the tool and the other parameters are unchanged. The resulting signal contrast is 0.37 V_{PP} in average and it varies during one rotation of the shaft between 0.34 and 0.39 V_{PP}. Because of the size of the disc it was impossible to take scanning electron microscope pictures of the gratings, but in appendix G profile measurements with a Talysurf CCI are presented. The low signal contrast can be related to defects and the general roughness of the mirror surface.

At the first glance encoders and gap sensors are both equally easy to operate in closed loop position control. It makes no difference that the absolute position can't be measured

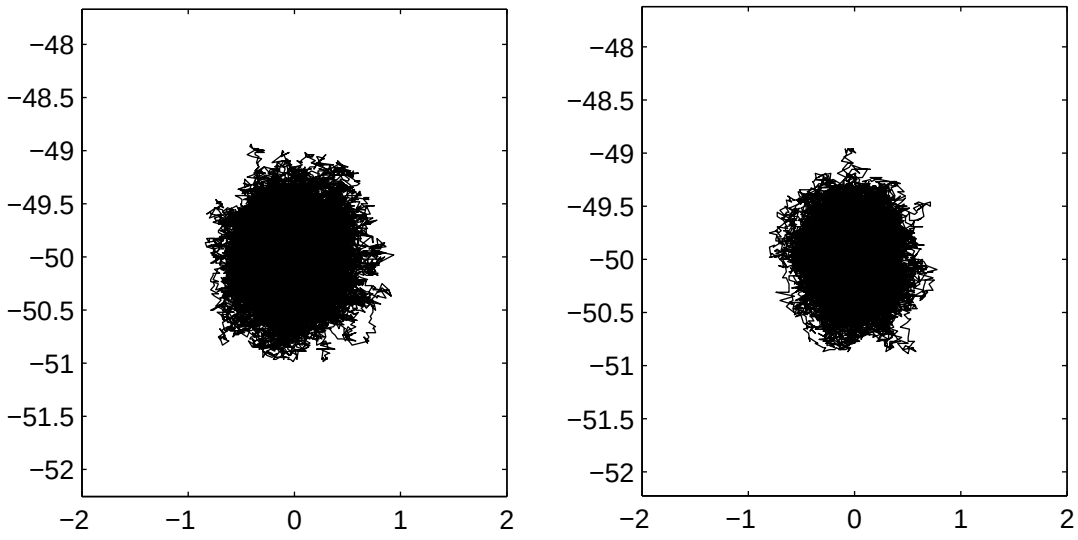

(a) $D = 0.5$ (b) $D = 0.7$

Figure 5.19: Whirl motion plots of gap sensor controlled AMB with AFVC algorithm and different damping ratios, both directions in µm

directly with incremental encoders. The initial position is referenced to the known touch-down bearing position. This approach has been used for the gap sensors, too, because it is safe and works in spite of thermal drift and changing conditions. Problems with the speed limit of encoders have not been encountered. It is for example possible to record frequency response functions where the armature moves rapidly. This is proven in appendix H for the open loop FRF and the plant FRF. It can be seen that up to a frequency of 333 Hz a positive phase can be maintained with the stated control parameters. Higher speeds of rotation than required in the R2R printing application are possible, see appendix I. When the frequency of the FRF identification passes 600 Hz, a loud tone testifies the vibration of the encoder disc. It can't be related to a shaft bending mode because there is no peak in the FRF at this frequency.

In figure 5.20 measured spectra of the gap sensors and the encoder are plotted. Ob-

viously, the eddy current sensor has more noise than the capacitive sensor. The encoder shows less noise than both the capacitive sensor and the eddy current sensor from 5 Hz upwards.

For derivative feedback control the velocity is calculated from the difference quotient of adjacent position samples and high frequency noise is amplified. Figure 5.21 shows the velocity signal that has been calculated in this way from position measurements of the stationary rotor. The sampling rate is 10 kHz. Comparing the sensors it can be said that encoders generate less noise for the position feedback.

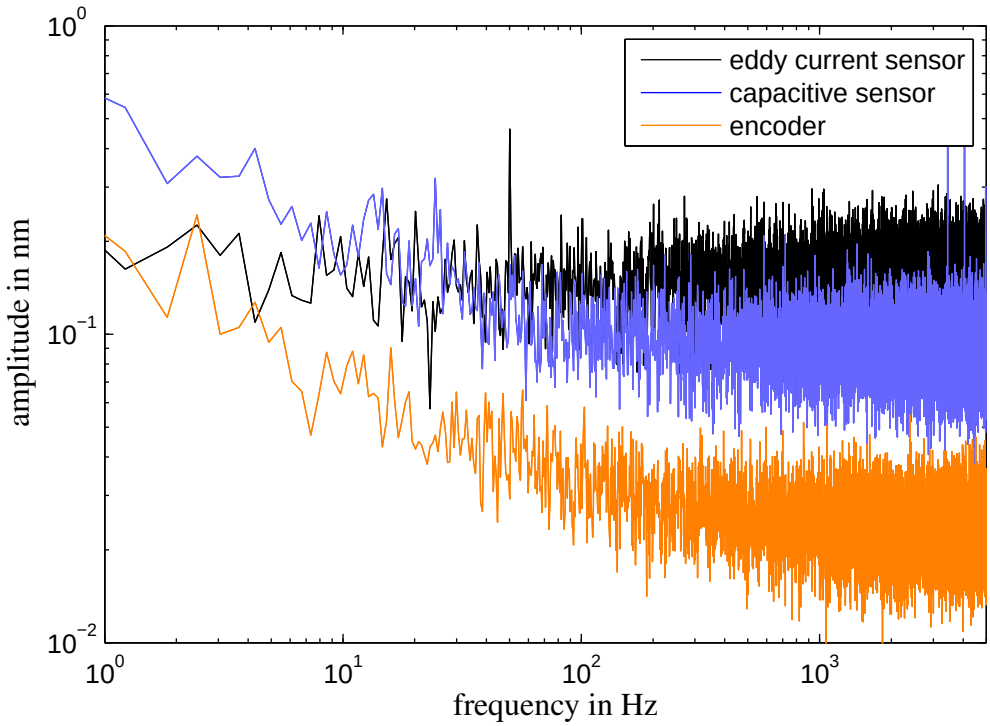

Figure 5.20: Sensor noise comparison of three different position sensors at standstill

The error motion plots in figure 5.22 have been recorded with a reference value of $(0,0)$. With encoders it is not necessary to restrict the range of movement. On the left five rotations without integrator and the machine spindle turned by hand are shown. The

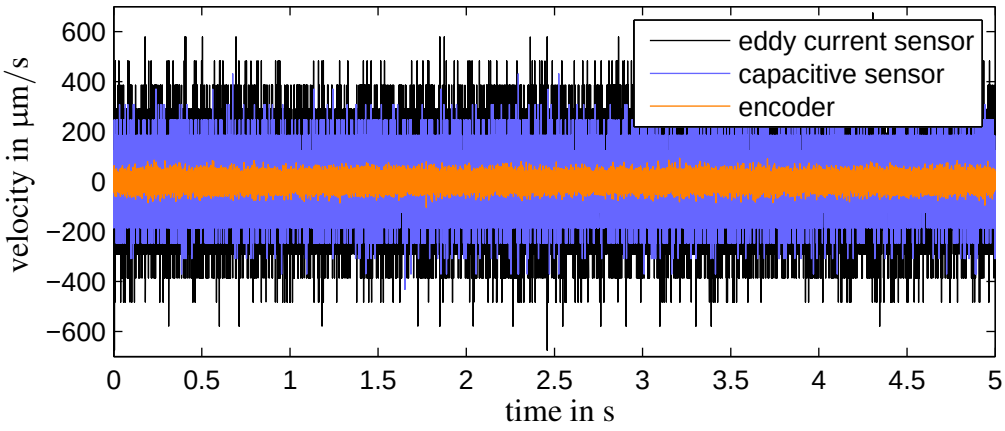

Figure 5.21: Velocity signal derived from position measurement for gap sensors and encoders

resulting error motion is 85 µm wide and 84 µm high. It has approximately the same size as the one in figure 5.15, but a different shape. The five rotations at low speed show the high repeatability of the motion if the sensor technology is not changed. On the right seven seconds without rotation, but with integrator and AFVC are displayed. The damping is 0.5 so that this figure can be compared to figure 5.19, a excepting that the sensors are different.

Analogously to figure 5.18 the FFT of the position control with encoders is shown in figure 5.23. The vertical direction x can be compared with the horizontal direction y. There is no obvious difference except for the structure induced vibration at ≈ 220 Hz with a differing shape. This difference can also be seen in figure 5.13. Comparing figures 5.18 and 5.23 it can be deduced that the noise at low frequencies looks similar independent of the employed position sensor. Only at frequencies beyond 800 Hz the noise is lower with encoders, which does not necessarily mean that the actual mechanical vibration is reduced at these frequencies. As can be derived from figure 5.20 the measured vibration is in the range of the sensor noise and it is impossible to distinguish between measurement error

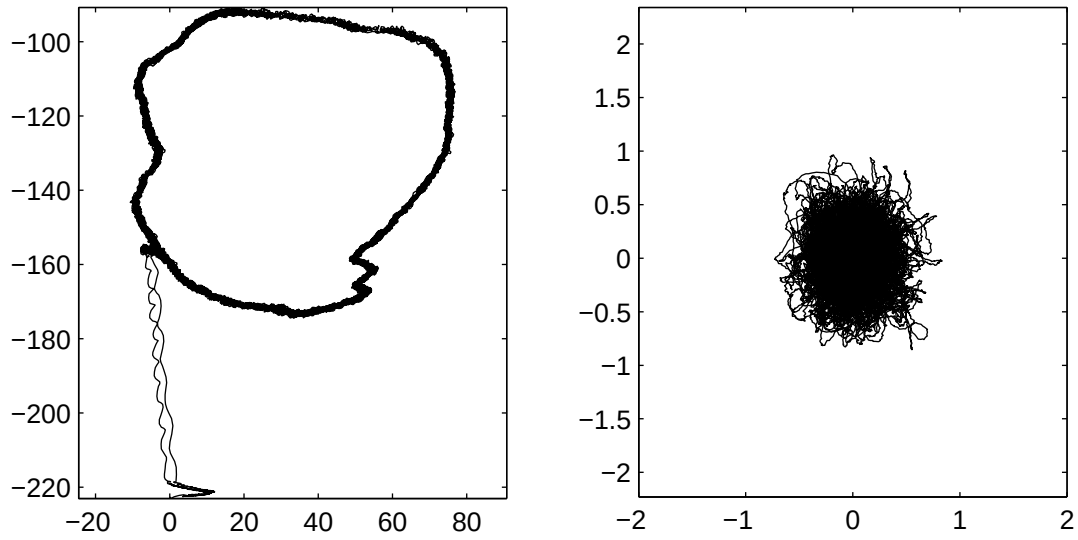

(a) Rotating

(b) Not rotating, with integrator and AFVC

Figure 5.22: Whirl motion of rotating and non-rotating AMB, x and y in µm, controlled with encoders.

and real movement.

There are two peaks at approximately $1,000\,\text{Hz}$ and $2,145\,\text{Hz}$, which are less pronounced in gap sensor control, see 5.18. They could be related to bending modes of the encoder disc and the shaft. The first one is more likely to be a flexible mode of the shaft because it is also visible in the FRFs recorded with gap sensors in figures 5.13 and 5.14. As the encoder disc is 9 mm further away from the actuators, the problem of non-collocation is more severe here.

After this visual performance demonstration a quantitative summary of the achievable performance shall now be attempted. Table 5.5 enlists the noise levels achieved with the three different sensors in RMS and the 7 s peak-to-peak values. Solely vertical measurements are stated so that potential differences in the structure between the axes are excluded. The sampling rate is 10 kHz. The first row of table 5.5 reflects the noise floor

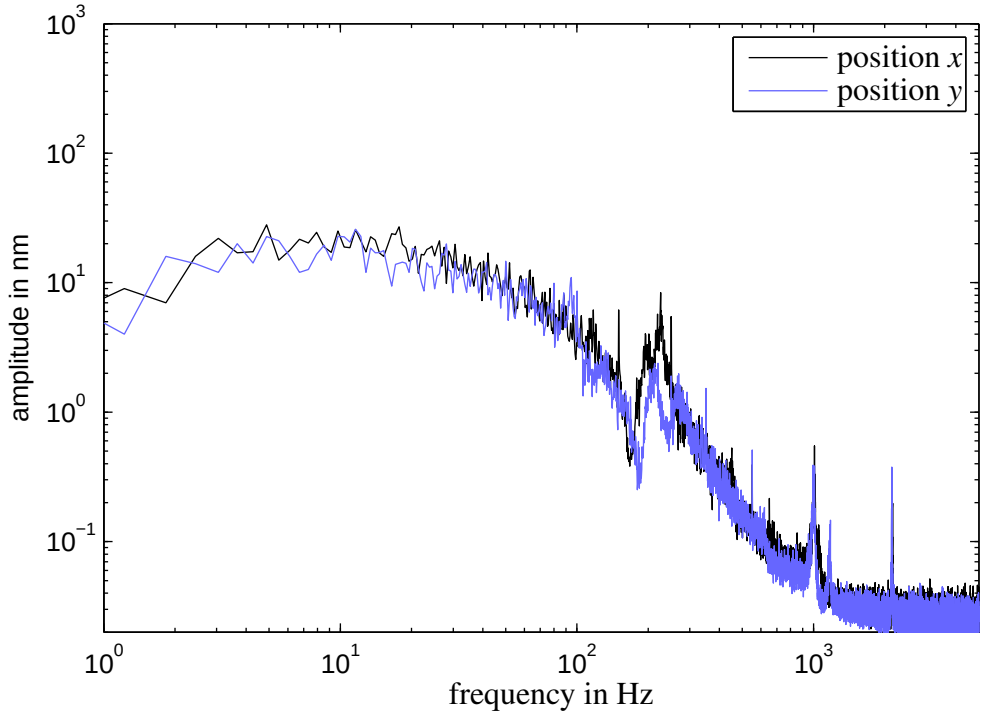

Figure 5.23: FFT of position noise with encoders for position measurement and active AFVC

of the respective sensor while it measures the stationary and non-rotating rotor. Only for these recordings the machine is turned off and there is no lubricant in the bearings. All the other numbers represent position control , either with or without AFVC and for three different dampling ratios.

As a result, the measured capacitive sensor is better than the eddy current sensor. With encoder there is a further reduction of the noise by a factor of approximately four when nothing is moving: 3.5 nm RMS and 51 pm standard deviation over five experiments. This shows the superiority of encoders. In closed loop the numbers with active AFVC are consistently better than those without AFVC. It is also unambiguous that under all conditions the results with higher damping are better. The difference between the sensors is not significant and not consistent. Often the values with encoders are slightly better,

Table 5.5: Comparison of sensor noise and AMB positioning noise for different sensors in x direction, unit: μm. No control means no levitation, only the sensor noise.

Control	D	Eddy current sensor		Capacitive sensor		Encoder	
		RMS	Peak-to-peak	RMS	Peak-to-peak	RMS	Peak-to-peak
No	-	0.023	0.19	0.014	0.12	0.0035	0.03
Yes,	0.3	1.02	5.03	0.89	4.52	0.89	4.49
without	0.5	0.55	3.10	0.51	3.13	0.51	2.82
AFVC	0.7	0.40	2.74	0.41	2.57	0.37	2.19
Yes,	0.3	0.40	2.89	0.38	2.96	0.37	2.91
with	0.5	0.30	2.24	0.29	2.35	0.26	1.92
AFVC	0.7	0.26	2.02	0.25	2.07	0.24	1.66

but that could be related to the lower sensor noise at high frequencies rather than to a difference in the actual motion of the shaft.

Chapter 6

Discussion

After presenting and interpreting the experimental results, a more general discussion of results and methods is attempted in this chapter. Apart from discussing the validity of results, the discussion deals with performance limitations to the position sensor and the magnetic bearing demonstrator.

6.1 Encoder experiments on the Nanotech 350UPL

Following the procedure in section 4.1.3 different gratings have been cut and viewed under the microscope as well as tested as encoder scale. These two comparatively quick ways of evaluation allow a clear judgement of success or failure. They complement each other as the encoders deliver quantitative performance measures, which are directly relevant in the application, while the microscope images reveal the reasons for contingently unsatisfactory results. However, it is also obvious that the level of satisfaction is closely related to a number of input parameters that have not been optimized like exact material composition, grain structure, tool angles, cutting speed, feed rates, lubrication and diamond quality. The validity of a conclusion such as one profile is superior to another is

strictly speaking restricted to the chosen set of process parameters. Especially if the performance is stunted by burr formation, the result can be highly non-repeatable. In order to get a thorough understanding more endeavour would be necessary than only one swatch of each type. This was limited by time and resources.

Noise measurements of the sensor have been done under various conditions to facilitate the discussion about critical noise sources. At both grating periods it can be seen that the ADCs have a considerable contribution to the noise although their noise has successfully been reduced by a self-made amplifier circuit.

What is missing in this noise analysis is an experiment with engaged scale but without machine to separate the noise of the machine from that of the encoder. It was practically not possible to align the setup precisely and with little drift without the machine. This has partly been made up for in the magnetic bearing itself where the encoder has been tested without any machine noise for one profile. Furthermore, only the vertical fixture (figure 4.2) has been used where the horizontal position control of the linear slideway should not play a role.

When the scale is rotating the noise is not only related to the ADCs and the reading head but mainly to scale defects. Accordingly the value is higher. An error influence in this experiment is the radial error motion of the machine spindle. The Nanotech 350UPL has a synchronous radial error motion of 15 nm, an asynchronous error of 10 nm and 19 nm total error at 500 rpm as to the documentation supplied with the machine. This falsifies the result. Other axes and bearings of the machine can be characterised by the fact that the motion accuracy is better than 50 nm and that components can be machined with a few nanometres surface finish [76]. With a measured roundness error of 80 nm or 100 nm RMS the error motions of the machine are below these values but still relevant. A more precise spindle was not available and it is questionable if it exists at all because air bearings are a good choice for high precision, see section 2.1.

Two procedures have been followed for the roundness measurement: One makes use of static experiments to eliminate the influence of the rotary speed control, the other captures the position at 10 kHz sampling rate while the disc is actually rotating. The disadvantage of the static experiment is that the error motion is only sampled in 37 points per revolution. The error of the rotational experiment is evident in the fact that slightly different results are obtained at different velocities. Both versions output approximately the same value so that a small residual error can be assumed, but for more certain results a rotary encoder would be required. With easy means it was not possible to read the encoder of the machine, nor to attach an additional rotary encoder to the spindle.

Without separate, more precise reference measurement it was not possible to measure the scale accuracy[1] over a longer distance. Using the machine encoder for this measurement would impose a traceability problem. The accuracy of the machine encoder also influences the sub-divisional error measurement (section 5.1.3). It has not been attempted to measure the accuracy in a different configuration, because the exact value is less important in this application with less than one millimetre stroke and it can be assumed that the encoder is accurate enough [32].

The last comment deals with the reduced size of the test samples. When the decision to use 120 mm aluminium samples for the trial cuts was made in section 4.1.2, the associated risks were pointed out. However, it was not expected that a difference in grain orientation and workpiece size could make the fabrication in aluminium completely impossible. This lack of repeatable conditions was paid for by a delay of eight weeks in the project.

[1] Here accuracy means the deviation of the measurand from the true value, not the noise.

6.2 Performance of encoders as position sensors

That encoders are more suitable for the radial position measurement in active magnetic bearings under certain conditions is evident from tables 5.1, 5.3, 5.5 and figures 5.20, 5.21. Model LIDA 48 has less noise than LIDA 28, as predicted in section 3.3.4 but both of them are an improvement over capacitive sensors. Especially the first row of table 5.5 allows the direct comparison of different sensors under good conditions and sampled at 10 kHz as required for the R2R AMB, see 3.4.2. In figure 5.20 it can be seen that from 5 Hz upwards encoders have less noise. Capacitive sensors with 508 µm range were readily available. In the final magnetic bearing sensors with wider range would be required, which are expected to have more noise (section 2.4.2).

With (c) and (f) profiles for both encoder types were found that fulfil the specifications of the supplier [24], namely position error per signal period and signal contrast. In section 5.1.4, however, it has been shown how the signal quality declines when the rotor in the AMB departs from the centre. This restricts the measurement range (more strictly with LIDA 48) and it means that at the air gap margin the measurement noise is higher than in the centre. The magnetic bearing demonstrator has shown that safe and reliable operation can be ensured in spite of this "soft" range restriction, even if the Lissajous diameter is only 0.37 V in the centre, which means the scale is not ideal, see section 5.2.3.

In experiments with rotating shaft it has been shown that the speed requirement of section 1.2 can be fulfilled with encoders as position sensors. Even if the rotary speed is two times as high as specified, no problems occur. Higher numbers of revolutions have not been checked out because the machine is not balanced for more than 600 rpm. It can be expected that at high speed the exact sensor noise is less important: Firstly, unbalance effects and gyroscopic couplings play an increasing role [128, 69]. These effects will outweigh the contribution of the position sensor to the error motion. Secondly, a certain

run-out in combination with a high rotational velocity will eventually exceed the lateral speed limit of $100\,\mathrm{mm/s}$ or $1,000\,\mathrm{mm/s}$ as explained in section 3.3.4. Thirdly, the noise spectrum caused by scale roundness errors shifts with speed of rotation. At low speed disturbances have a low frequency, too, so that they are not much amplified because the sensitivity function has a low gain at low frequencies [81]. At high speed they should be more critical. These three effects suggest using the proposed position sensor preferably at low speed.

It has also been shown that roundness errors can be calibrated and thereby reduced (section 5.1.2 and figure 5.10). This technique is limited by the effort to measure and store compensation values for a high number of angles. For optimal results the radial position had to be considered, too, not only the angle, resulting in a 2D look-up table. In the experiment only one value has been saved for each angle to save time. This 1D look-up-table was then applied to compensate measurements in different radial positions. Depending on the actual radial position the compensation was more or less exact and the average error is $15.8\,\mathrm{nm}$. This experiment shows what can be expected from a calibration measurement with tenable effort.

One last limitation is related to the vibration of the encoder disc at $600\,\mathrm{Hz}$. Although the frequency response functions are only hardly affected by this peak at $600\,\mathrm{Hz}$, see for instance figure 5.14, the thin disc is still an additional complication in the design. It also makes the integrability into a housing more difficult (section 3.5).

6.3 Positioning uncertainty of the AMB demonstrator

In closed loop position control it was possible to stabilize the magnetic bearing with a positioning uncertainty of $\approx \pm 1\,\mu\mathrm{m}$ and $\approx 0.25\,\mu\mathrm{m}$ RMS in the best configuration, see table 5.5. To achieve this, different measures like additional cable screening, rewiring and

AFVC (section 5.2.2) have been applied. The performance capability is still not sufficient for a printing machine bearing in this respect, see section 1.2.

The performance is comparable to other magnetic bearings of similar size but not better. Examples are the magnetic bearings in [100], [91] and [43], already cited above. The magnetic bearings in [100] with 250 kg and 25 kg rotor mass, respectively, have a positioning accuracy of 2 µm peak-to-peak with PID_{T1} control and approximately 1 µm peak-to-peak with extended Kalman filter. The AMB built by Petzold [91] with 1,864 kg rotor mass has approximately 3 µm peak-to-peak noise when not rotating. The third example has 0.35 kg rotor mass and approximately 1 µm peak-to-peak error motion in radial direction and a bit more in axial direction [43]. The mass and the design are not directly comparable, though.

The question is why the magnetic bearing controlled with encoders is not better although the sensor resolution is superior. There is also no significant difference between control with gap sensors and encoders of the same magnetic bearing, see section 5.2.3 and table 5.5. From the analysis of sensor noise and power amplifier current control fidelity it can be inferred that the current ripple of the power amplifier is the performance limitation. This shows that low-quality amplifiers do not only cause sensor interference but directly position undulations. Because of budget and time limitations it was not possible to replace them. There are for example switching type amplifiers with synchronisation between the current control channels and also between current and position control to avoid mutual interference, but the BA30 amplifiers do not support this option [94, 3]. Often amplifiers are made by the researchers themselves but the time scale did not allow that either [50, 22].

As soon as the shaft rotates, its centre point describes a whirl motion, see figures 5.15, a and 5.22, a. For tracking control and feed-forward compensation of this whirl motion a rotary encoder would be necessary. Since this piece of work is not part of the objectives, there is no rotary encoder in the design and no compensation has been attempted.

Experiments with rotating shaft could be used to calculate the synchronous error, asynchronous error and total radial error motion. Instead, experiments with non-rotating shaft have been evaluated to get an estimate for the asynchronous radial error motion at low speed. This is because the machine cannot run at very low speed like 2.39 rpm, at which the asynchronous error would be of interest, see section 1.2.

6.4 Stiffness, bandwidth

Stable operation has been achieved with the same positive stiffness as the bearing's negative stiffness, which was expectable. Also the stability range for the damping $(0.2 \leq D \leq 0.8)$, which equals $-0.204 \leq \sigma/\omega \leq -1.33$, is close to literature values [10, 81]. What is not satisfactory is the stiffness of $0.41\,\mathrm{N/\mu m}$ as opposed to approximately $15\,\mathrm{N/\mu m}$, which was predicted in section 3.2. The explanation is as follows: Flexible modes at 220 Hz limit the bandwidth to a maximum of 120 Hz (figure 5.14). Because of the low rotor mass of 23 kg the stiffness that leads to 120 Hz bandwidth is also low. In the R2R machine the rotor mass is much higher, approximately 200 kg on two radial bearings so that a higher stiffness is permissible for the same bandwidth [81, 50]. It will still be necessary to determine and optimize the dynamic behaviour before the design can be considered valid.

The bandwidth of the AMB demonstrator could possibly be extended by adding notch filters, but this effort is not justified in the temporary design. The demonstrator has entirely different structural properties and it has not been designed to make predictions about the stiffness of the final design. These predictions are still limited to the estimates of section 3.2.

Notwithstanding the fact that the value of the bandwidth has a limited general expressiveness, its value is comparable to those achieved on other magnetic bearing test stands,

see table 6.1. The achieved bandwidth of 120 Hz for one radial bearing and 23 kg rotor

Table 6.1: Examples of magnetic bearing bandwidths found in literature

Bandwidth	Reference	Comment
30 Hz	[103]	Especially long and thin: 600 mm long and 10 mm thin with a total mass of 2.84 kg
46 Hz...72 Hz	[22]	Depending on direction
85 Hz	[17]	Linear positioning stage with flexures
100 Hz	[94]	391 kg flotor mass, linear stage, lateral direction
130 Hz	[94]	45.6 kg flotor mass, linear stage, lateral direction
150 Hz	[50]	2.69 kg rotor mass
163 Hz	[91]	1,864 kg rotor mass
200 Hz	[124]	Radial bearing, first flexible mode at 700 Hz
215 Hz	[43]	0.35 kg rotor mass, radial direction
255 Hz	[43]	0.35 kg rotor mass, axial direction
282 Hz	[77]	Radial bearing
318 Hz	[124]	Thrust bearing
450 Hz	[60]	0.18 kg rotor mass, radial bearing

mass is neither particularly low nor especially high. In order to improve the bandwidth it would be advisable to replace the aluminium bridge by a steel part. In any case the expectable resonant modes should be calculated and interpreted on the basis of the target bandwidth, which has not been done in this thesis because the effect of flexible modes has been underestimated.

Chapter 7

Conclusion and future work

The last chapter summarizes the findings and contributions and reflects upon the satisfaction of objectives. Finally some suggestions for further work are made.

7.1 Conclusion

The quest for high precision in spite of geometric imperfections in the R2R flexible electronics industry has been addressed by designing a magnetic bearing for a large-scale printing machine. Magnetic bearing, control hardware and power amplifiers have been specified and purchased. An innovative position sensor based on conventional linear optical encoders has been proposed and demonstrated in a number of experiments. The special scale for these encoders was made by micro-machining. Different versions of the scale have been machined and analysed in experiments. Finally a magnetic bearing has been built to demonstrate the performance of the position sensor and the other purchased components in closed loop. In addition, the magnetic bearing was equipped with ordinary gap sensors to compare the performance.

Contributions to knowledge have been made

- by providing an innovative method to measure the position of radial AMBs,
- by characterising this method analytically and in experiments,
- by definition and empirical investigation of procedures to create amplitude gratings for commercial optical encoders by micro-machining,
- by designing magnetic bearings for flexible electronics R2R production systems.

The resulting radial magnetic bearings have a nominal load capacity of 5.3 kN each and the nominal load capacity of the axial magnetic bearing is 4.8 kN (table B.1). This is below the load capacity of the hydrostatic bearing that is currently incorporated in the machine (9.09 kN radially and 5.28 kN axially) [129]. Suitable rolling element bearings have been found with 20 kN load capacity (section 2.1.1). The magnetic bearing requires more installation space than the other two bearing types (sections 3.5 and 2.1) and at the same time it has the lowest load capacity, but the specifications for the load capacity are still fulfilled, see section 1.2.

Although the magnetic bearing stiffness could not be scrutinized in experiments, an estimate could be calculated for medium load frequencies: $12.7\,\mathrm{N/\mu m}$ in vertical direction, $15.7\,\mathrm{N/\mu m}$ in radial, horizontal direction and $15.5\,\mathrm{N/\mu m}$ for the thrust bearing, see section 3.2. These values are also below those of hydrostatic bearings ($80-100\,\mathrm{N/\mu m}$ radially and $21.2-84.8\,\mathrm{N/\mu m}$ axially). The stiffness of the rolling element bearing would be even higher: $1,429\,\mathrm{N/\mu m}$. On the other hand magnetic bearings have an infinite stiffness at 0 Hz and since the application requires low speed of rotation and rapidly changing process forces are not expectable this special application makes advantage of the high static stiffness of magnetic bearings.

The experiments with encoders for radial position measurement have borne suitable micro-machining procedures for both 20 µm encoders and 200 µm encoders. The noise

with 20 µm grating period is 3.5 nm RMS at 10 kHz sampling rate with the best scale type and with 200 µm grating period it is 13.8 nm RMS. Both types are an improvement over capacitive sensors with 20 nm RMS nominal noise, which are usually used in magnetic bearings. There are capacitive sensors with less noise, but their range is not wide enough for this magnetic bearing. Other gap sensors have more noise than capacitive sensors (section 2.4). It can be concluded that the proposed sensor has better characteristics than gap sensors under static conditions. Practically speaking, encoders are also easier to use because their grating period is exactly known and a non-linearity calibration is not always required as it is for gap sensors and curved targets.

When the shaft rotates, there are other noise sources so that it is more difficult to quantify the noise. Electrical noise of eddy current sensors and target imperfections of capacitive sensors have the same effect, but these have not been measured so that a direct comparison cannot be made.

Another effect is the deterioration of the signal quality when the shaft departs from the air gap centre. This effect has been analysed analytically (section 3.3.4) as well as in experiments (section 5.1.4). A good correlation of calculated and measured behaviour can be observed. In the magnetic bearing it has been shown that reliable position tracking is possible in spite of this deterioration effect.

An aluminium substrate and blackboard paint have been used as workpiece materials for micro-machining of the encoder scales. These are cheap and easily available so that this sensor can be used by other research centres where low noise at high sampling rate and low speed of rotation is required. However, the procedure is time-consuming and in institutions where this work must be paid, process optimisations will be necessary. Companies that produce encoders could be inspired by this work and decide to manufacture magnetic bearing scales with conventional photolithography techniques. It should be analysed if other, e.g. finer or absolute encoders can work, too, see section 7.2.

In experiments on the active magnetic bearing prototype a positioning uncertainty of $\approx \pm 1\,\mu m$ and $\approx 0.25\,\mu m$ RMS was the best result that could be achieved with different optimisations. The size of the AMB is large enough for the R2R machine so that the achieved accuracy is directly relevant. It is a typical value for a large magnetic bearing with heavy rotor, as discussed in section 6.3, but it is not better than other examples and does not meet the specifications of section 1.2. The power amplifiers have been identified as the main reason for this problem. Adaptive feed-forward vibration compensation has successfully been applied to reduce 50 Hz line interference.

Except from the amplifiers the purchased components work together well. Up to a frequency of 333 Hz phase lead can be maintained. The real-time target machine from Speedgoat seems to be a good and reliable choice for the control hardware although it is not a typical platform for magnetic bearing control. In fact, no reference has been found where it is used. Even with adaptive feed-forward vibration compensation algorithm only about 22 % CPU workload occurred. The remaining work to get the designed R2R magnetic bearing working should be easier, now that the control equipment is available.

The objectives from section 2.7 have all been achieved, which is a contribution to the aim. In order to answer the question more exhaustively if magnetic bearings are applicable to printing machines a lot of further work will be required as proposed below. Especially the critical issue of the stiffness needs further investigation and the synchronous error motion of the rotating magnetic bearings has to be reduced. These steps are necessary before the magnetic bearing can really supersede roller bearings or hydrostatic bearings. As far as the statement is already possible, all the specifications from table 1.1 have been met, expect for the housing length and the positioning accuracy. The fact that the housing length is exceeded has to be countenanced, but the positioning accuracy should be improved.

All in all, the thesis at hand constitutes groundwork on the way of realizing a flexible

electronics R2R machine with magnetically suspended printing roller. The experimental results were in agreement with the predicted outcome from theory. Only a few initial steps have been made but the most critical limitation of magnetic bearings in the R2R application has been addressed and promising results have been achieved. It should be possible to improve the performance of magnetic bearings in the future.

7.2 Future work

The following points of future work in the field of encoder and grating experiments shall be recommended:

- Optimize the machining parameters for micro-machining.
- Grating experiments in electroless nickel or chrome instead of aluminium
- Wider tool angle for profile (e); the tool on-hand did not work, but a wider included angle might help.
- New test rig for function analysis with rotary encoder
- Investigate the tilt tolerance of encoders with factor ten finer grating period and undiminished ride height tolerance, e.g. the product LIP 200 from Heidenhain with 2.048 µm grating period, 31.25 pm resolution and ± 1 nm sub-divisional error [24].
- Investigate gratings for absolute encoders based on the principle of pseudo random line spacings [24].

The 2-DOF magnetic bearing demonstrator could be used for a few further experiments:

- New amplifiers, probably linear instead of PWM, or linear fine control in addition to the existing PWM coarse control

- Add a metrology frame to the AMB demonstrator. As the first flexible modes are clearly related to the structure this might extend the stiffness and bandwidth [50].
- Compensation of measurement errors due to measurement on curved target

The main part of future work deals with the magnetic bearings for the R2R machine:

- Complement the design including water cooling for the printing drum and optimize the dynamic behaviour.
- Possibly second radial encoder, 200 µm axially offset to extend the axial tolerance
- Assembly and commissioning of the R2R AMB, optimisation of the stiffness
- High precision tracking control in radial direction and rotation about geometric centre at low speed [41, 64, 68]
- Identify a prescription for the position reference.

Appendix A

Derivation of the reluctance actuator force

The following calculation is the derivation of the force of a reluctance actuator with respect to the input current. It is adopted from [81] and shortened.

The electrical input power P_{in} that drives an electric actuator with a coil arises from the known current and three voltage drops: the voltage over the ohmic resistor R, the voltage over the self-inductance L due to changes in the current over time and the voltage induced, when the flux Φ through the coil changes:

$$P_{\text{in}} = i^2 R + iL\frac{\mathrm{d}i}{\mathrm{d}t} + ni\frac{\partial \Phi}{\partial x}\frac{\mathrm{d}x}{\mathrm{d}t}. \tag{A.1}$$

x represents the position of the moving part, for instance the magnetic bearing rotor, see figure 2.3.

Independent of that the input energy is split into three types: Part of the input energy is stored in the coil $P_{\text{storage}} = P_{\text{L}}$ and the output energy comprises thermal dissipation P_{diss}

and mechanically useful power P_{mech}:

$$P_{\mathrm{in}} = P_{\mathrm{storage}} + P_{\mathrm{out}} = P_{\mathrm{L}} + P_{\mathrm{diss}} + P_{\mathrm{mech}}. \tag{A.2}$$

If it is assumed that the inductance of the coil does not change with the current, the energy in a coil is $E_{\mathrm{L}} = \frac{1}{2}L(x)i^2$ and the power necessary to "charge" this coil becomes

$$P_{\mathrm{L}} = \frac{\mathrm{d}}{\mathrm{d}t}E_{\mathrm{L}} = iL(x)\frac{\mathrm{d}i}{\mathrm{d}t} + \frac{1}{2}i^2\frac{\mathrm{d}L(x)}{\mathrm{d}t}. \tag{A.3}$$

The dissipated energy is $P_{\mathrm{diss}} = Ri^2$. The combination of the equations (A.1), (A.2) and (A.3) yields the mechanically useful power:

$$P_{\mathrm{mech}} = ni\frac{\partial\Phi}{\partial x}\frac{\mathrm{d}x}{\mathrm{d}t} - \frac{1}{2}i^2\frac{\mathrm{d}L(x)}{\mathrm{d}t}. \tag{A.4}$$

The relationship between force and mechanical power is

$$P_{\mathrm{mech}} = \frac{\mathrm{d}x}{\mathrm{d}t}\cdot f_x \Leftrightarrow f_x = P_{\mathrm{mech}}\cdot\frac{\mathrm{d}t}{\mathrm{d}x}, \tag{A.5}$$

which allows the calculation of the force from equations (A.4) and (A.5):

$$f_x = ni\cdot\frac{\partial\Phi}{\partial x} - \frac{1}{2}i^2\frac{\mathrm{d}L(x)}{\mathrm{d}x}. \tag{A.6}$$

For an electrodynamic actuator based on Lorentz force the subtrahend in equation A.6 is often zero, because the moving part is not necessarily made from ferromagnetic materials so that the inductance $L(x)$ is independent of x. In case of typical reluctance actuators, however, the self-inductance changes with x, because the magnetic reluctance $R_{\mathrm{m}}(x)$

varies. With the known correlation $n\Phi = iL$, the subtrahend of equation A.6 is exactly half of the minuend and only

$$f_x = \frac{1}{2} i^2 \frac{\mathrm{d}L(x)}{\mathrm{d}x} \tag{A.7}$$

remains. To further calculate the force of a specific actuator, the position dependent inductance must be calculated as a function of the magnetic reluctance [81].

Appendix B

Specifications of the AMB actuators

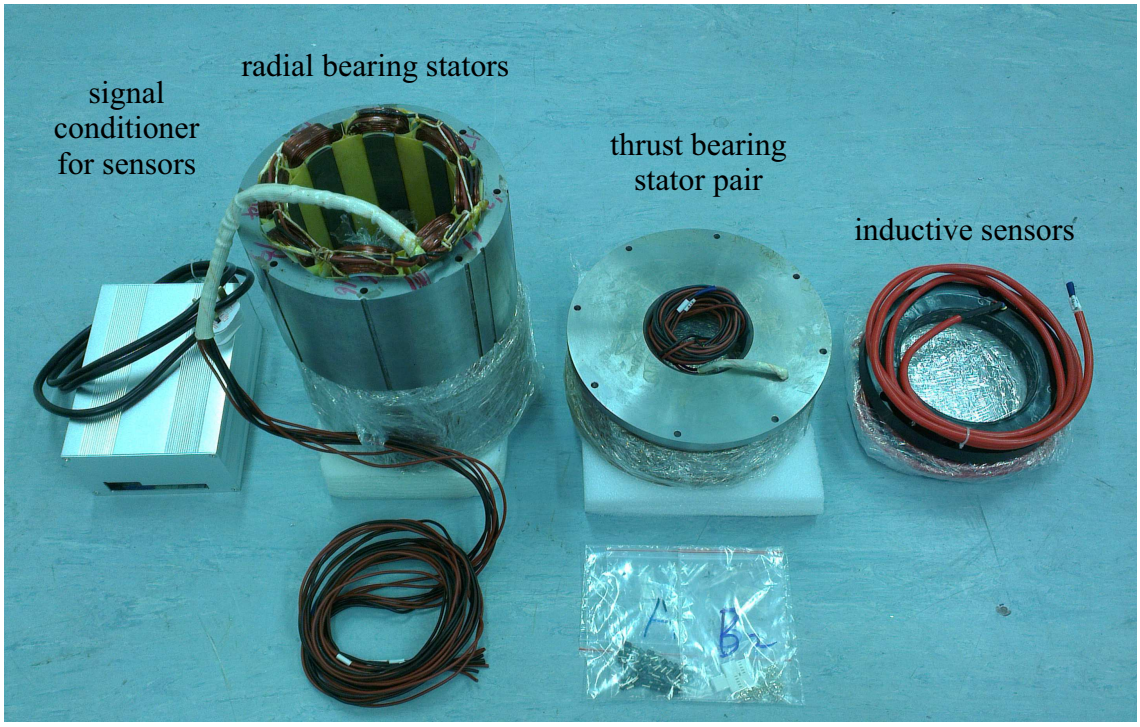

Figure B.1: Photo of the magnetic bearing order from Foshan Genesis, partially unwrapped

Table B.1: Details on the magnetic bearing core from Foshan Genesis according to the product documentation from the company [31]

Feature	Value	Unit	Note
Length radial bearing	160	mm	-
Length axial bearing pair	$2 \times 42 + 16$	mm	Two opposing coils with rotor disc in between
Length inductive sensor	21	mm	-
Diameter inductive sensor	210	mm	-
Diameter radial bearing	220	mm	-
Diameter axial bearing	256	mm	-
Air gap area A_r radial	0.00312	m^2	-
Air gap area A_a axial	0.00866	m^2	-
Load capacity radial bearing	2×5.3	kN	Only with cooling or for a short time
Load capacity axial bearing	4.8	kN	Only with cooling or for a short time
Number of windings, radial	130	-	
Number of windings, axial	150	-	
Max. continuous current, radial	7	A	
Max. continuous current, axial	11	A	
Resolution inductive sensor	1	µm	Only for radial position measurement

Table B.2: Characteristics of the power amplifier BA30 from Aerotech according to the product datasheet [3]

Feature	Value	Unit	Note
Input voltage	230	VAC	Single phase
DC circuit voltage	320	V	$320\,\mathrm{V} \approx \sqrt{2} \cdot 230\,\mathrm{V}$
Continuous output current	15	A	-
Peak output current	30	A	-
Min. load inductance	1	mH	-
Analogue control voltage	± 10	V	For positive and negative output current
Bandwidth	2	kHz	current control
Max. efficiency	97	%	-

Appendix C

Transfer function of the encoder interface

The encoder interface is based on operational amplifiers as sketched in figure C.1. Z_1 summarizes R_2 and C_2. Assuming and ideal transfer characteristic of the operational amplifier ($U_1 = U_2$, the current of the inputs is zero, the gain is infinite, ideal common mode rejection) the transfer function of the circuit can be calculated as follows. Dependencies of the circular frequency ω are not indicated explicitly for simplification reasons. Start

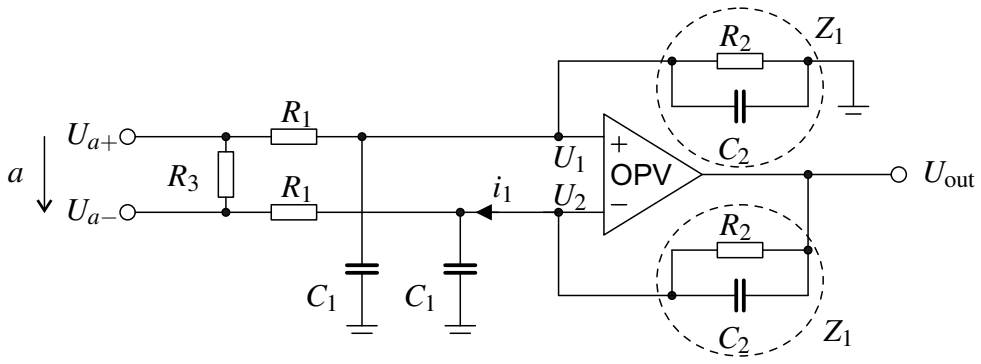

Figure C.1: OP-AMP circuit diagram for encoder interface

with

$$U_1 = \frac{(Z^{-1} + \mathrm{j}\omega C_1)^{-1}}{R_1 + (Z^{-1} + \mathrm{j}\omega C_1)^{-1}} U_{a+}, \tag{C.1}$$

$$i_1 = \frac{U_1 - U_{a-}}{R_1} + \mathrm{j}\omega C_1 U_1, \tag{C.2}$$

$$U_{\mathrm{out}} = U_1 + i_1 Z_1. \tag{C.3}$$

Equation C.2 is plugged into equation C.3:

$$U_{\mathrm{out}} = U_1 \left(1 + \frac{Z_1}{R_1} + \mathrm{j}\omega C_1 Z_1\right) - \frac{Z_1}{R_1} U_{a-}. \tag{C.4}$$

Then equation C.1 is also plugged into the term for U_{out} and Z_1 is finally written in terms of R_2 and C_2:

$$\begin{aligned} U_{\mathrm{out}} &= U_{a+} \cdot \frac{Z_1}{R_1 + \mathrm{j}\omega C_1 R_1 \cdot Z_1 + Z_1} \frac{R_1 + \mathrm{j}\omega C_1 R_1 \cdot Z_1 + Z_1}{R_1} - \frac{Z_1}{R_1} U_{a-} \\ &= U_{a+} \cdot \frac{Z_1}{R_1} - \frac{Z_1}{R_1} U_{a-} \\ &= \frac{R_2}{R_1} \frac{1}{\mathrm{j}\omega R_2 C_2 + 1} (U_{a+} - U_{a-}) = \frac{R_2}{R_1} \frac{1}{\mathrm{j}\omega R_2 C_2 + 1} a \end{aligned} \tag{C.5}$$

.

A first order low-pass filter with a cut-off frequency of

$$f_{\mathrm{g}} = \frac{1}{2\pi R_2 C_2} = 18.45\,\mathrm{kHz} \tag{C.6}$$

results. R_1 and R_2 determine the static gain, which is $3.92 \approx 4$ for the resistor values $R_1 = 10\,\text{kHz}$ and $R_2 = 39.2\,\text{kHz}$. R_3 acts as a line terminator for the connection to the encoder reading head.

Appendix D

Roundness measurement on the rotating scale

The RMS of the encoder output is measured while the encoder disc rotates at a number of different speeds. With the technique described in section 5.1.1 an estimate of the spindle run-out is calculated in every rotation and subtracted from the measurement. For each speed step ten rotations are evaluated. The error bars refer to these ten repetitions and they have a length of two times the sample standard deviation, see figures D.1 and D.2. For $0\,\text{rpm}$ the RMS value is based on simple noise measurements over $5,000$ samples. The results are comparable to static measurements in sections 5.1.1 and 5.1.2.

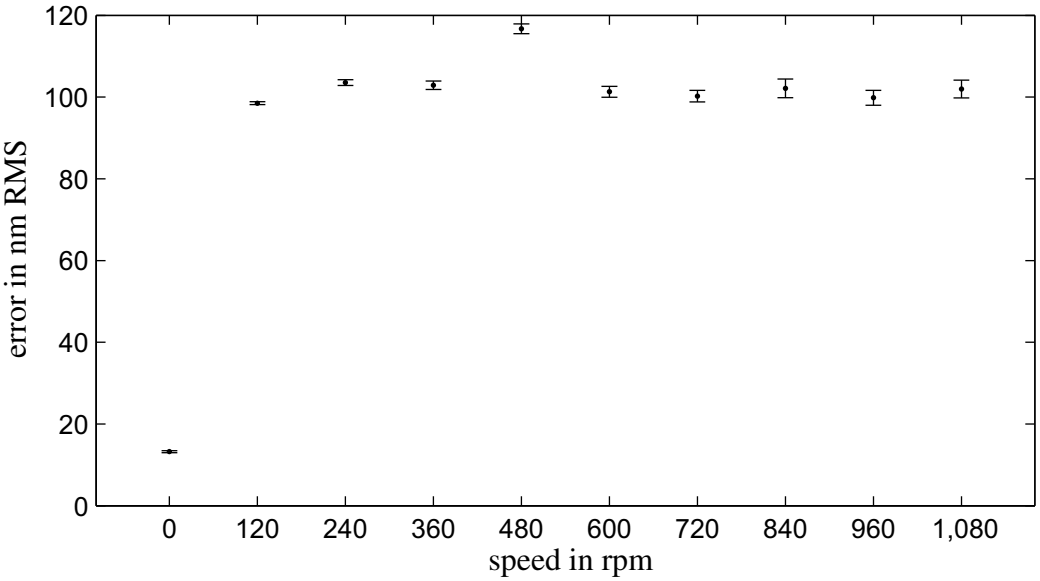

Figure D.1: LIDA 28 measurement error for different rotational velocities

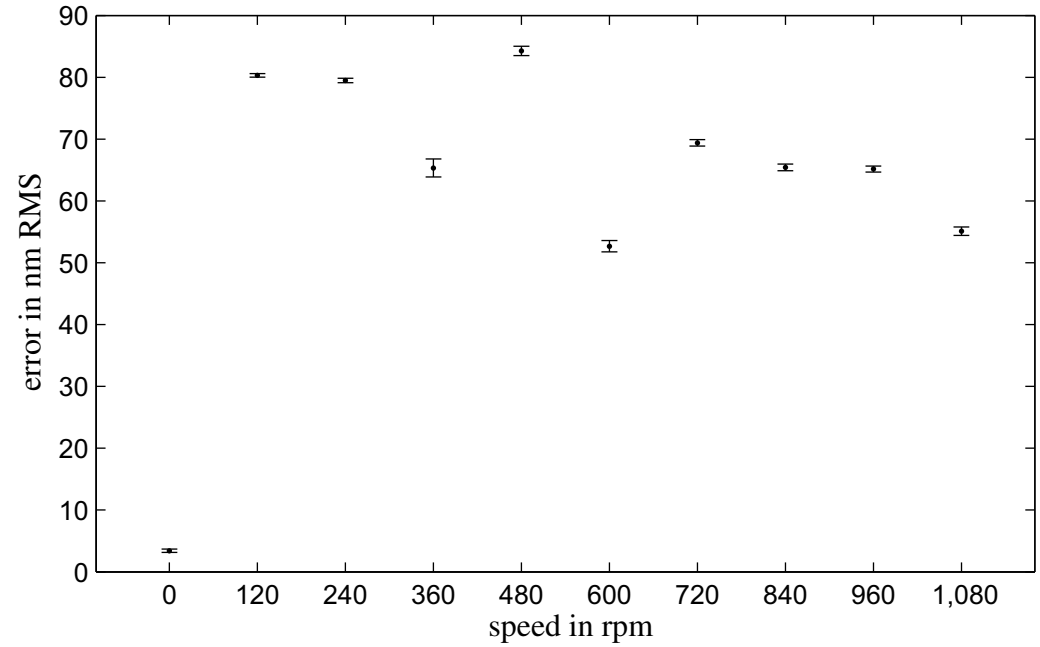

Figure D.2: LIDA 48 measurement error for different rotational velocities

Appendix E

Scale length requirement

The minimum scale length defines the amount of grooves that have to be cut and is therefore an important characteristic, but it is not specified in the catalogue. It is also necessary to know the scale length seen by the reading head ($m \cdot p$) to apply equation 3.18. In linear position measurements with conventional scales it is not of interest for the user. However, this is different in the magnetic bearing where the range of movement is short and the price for machining the grooves is proportional to their amount.

The encoder reading head is mounted horizontally as shown in figure 4.3. It moves 20 mm radially while passing the raster area on the scale. The later is not rotating. While moving the output signal amplitude changes as shown in figure E.1.

In a small band around 0 the amplitude is almost constant and the operation is not adversely affected by the movement. For LIDA 28 this range is 5 mm long and for LIDA 48 it is 8.5 mm long. At larger strokes the measurement shows abnormalities and the valid range is obviously exceeded. As all scales are 16 mm long the minimum lengths can be calculated: For LIDA 28 it is 11 mm plus desired range of movement and for LIDA 48 it is 7.5 mm plus range of movement. To facilitate the alignment, it is advisable to extend this length by a few millimetres.

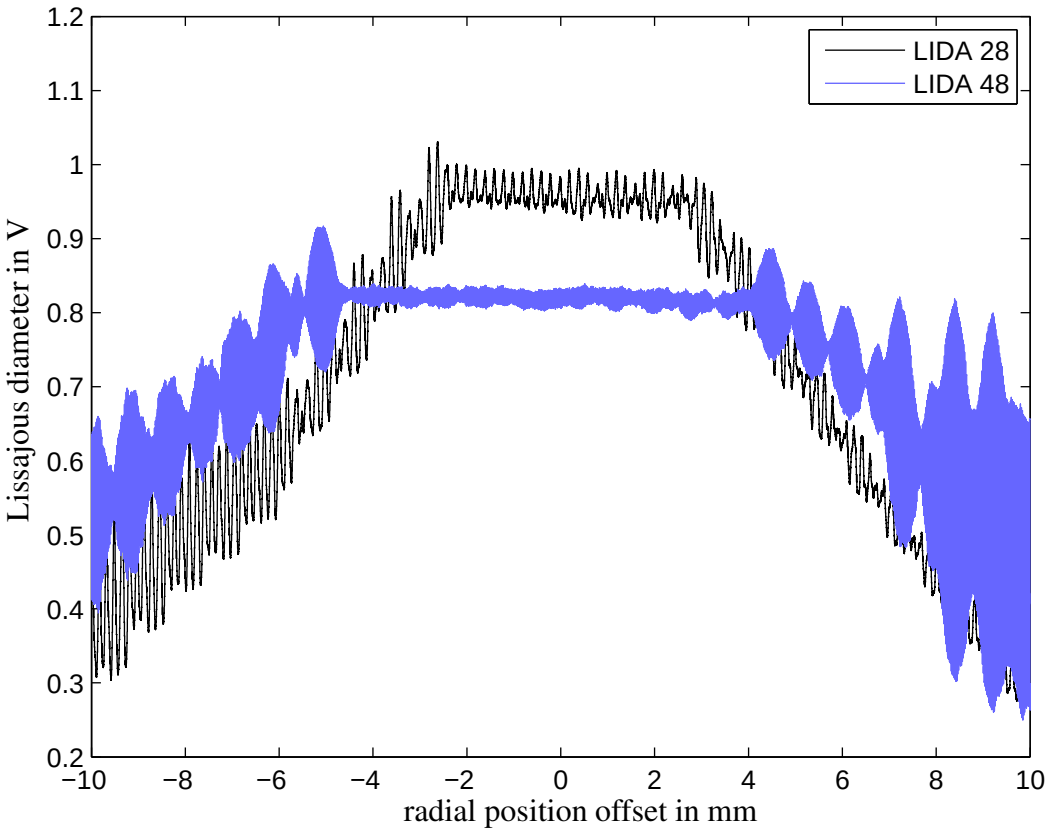

Figure E.1: Signal contrast against radial position along the scale for both grating periods

Appendix F

Noise spectrum of power amplifiers

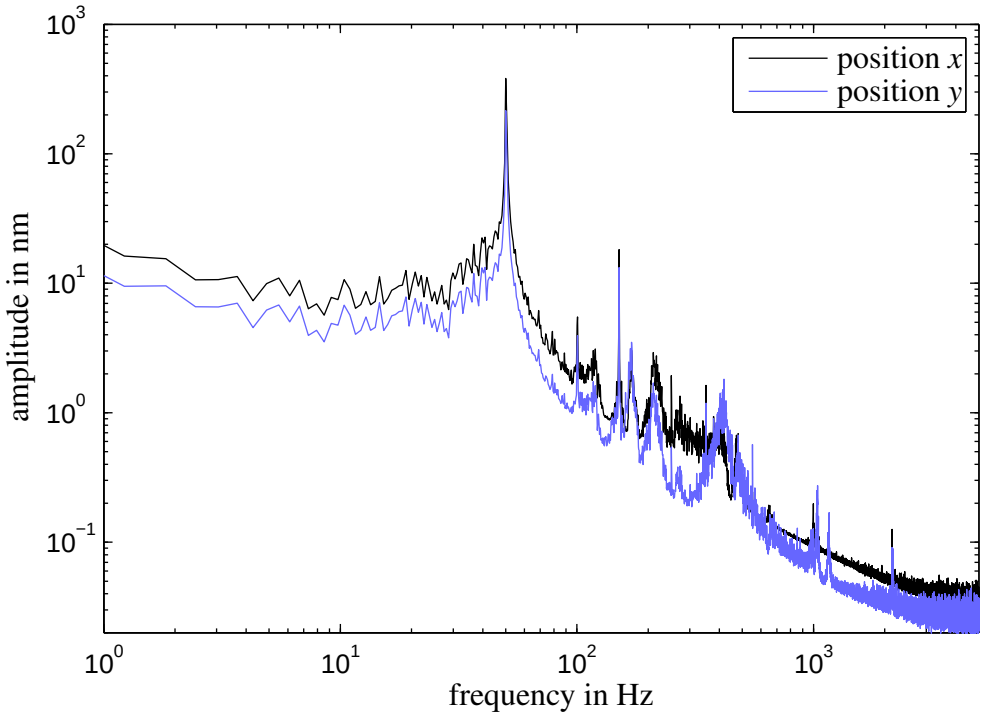

Figure F.1: FFT of position measurement with encoders while the amplifiers for the horizontal coils have a constant reference signal of 1 A. The reference signal for the other amplifiers is 0.

Appendix G

Coherence correlation interferometry images of AMB encoder disc

This appendix shows surface measurements taken with a Talysurf CCI from Taylor Hobson, a division of the company AMETEK Inc. Figure G.1 shows the nickel plated surface of the encoder disc in the magnetic bearing. It has been diamond turned after coating but no gratings have been cut. The arithmetic mean deviation of the roughness as displayed by the instrument is $R_a = 7.12\,\text{nm}$, the total height of the roughness profile is $R_t = 74.2\,\text{nm}$. Visually the surface looks streaky and shows defects.

Figure G.2 displays the outer edge of the structured surface (profile (d) in figure 4.5). Areas with steep slopes cannot be detected by the optics and are displayed in grey. Figure G.3 is the corresponding profile in radial direction. The slopes are missing, too, but the intended profile consisting of V-grooves can be identified. There seems to be no burr and the cutting depth is uniform across the structured band. The ridges are 7 µm wide.

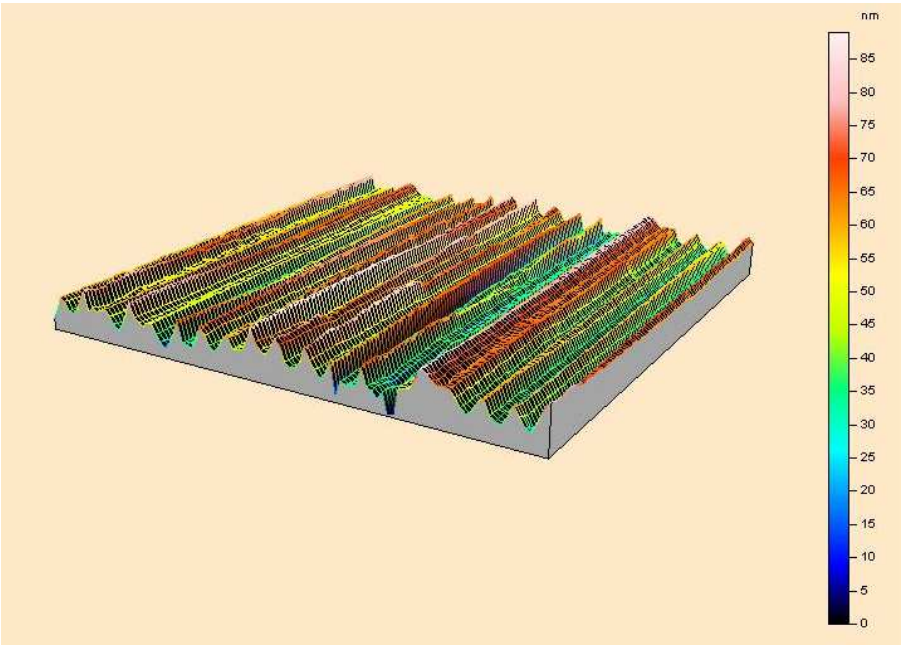

Figure G.1: Diamond turned electroless nickel surface of encoder disc without gratings

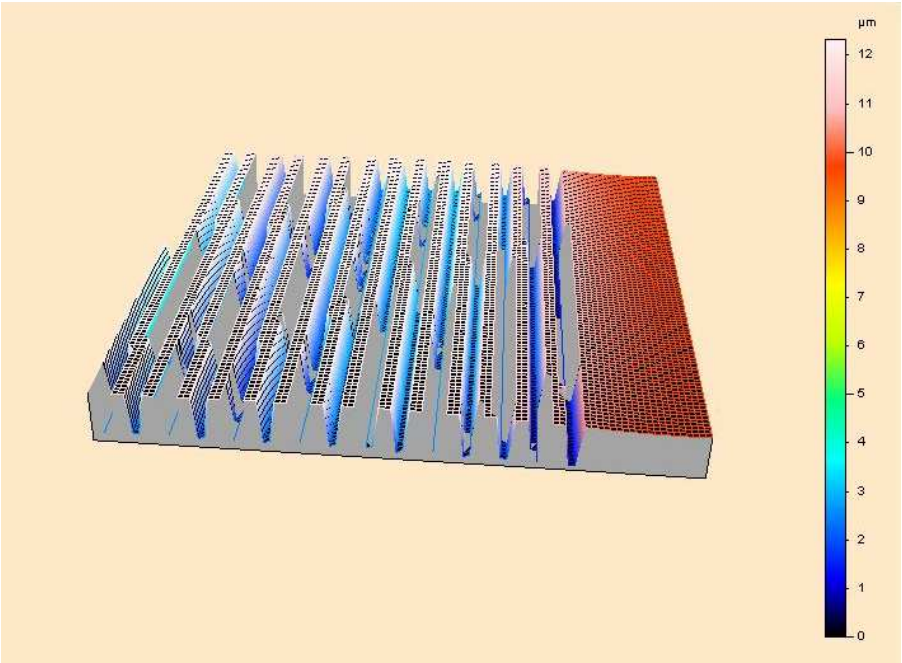

Figure G.2: Gratings in electroless nickel surface of encoder disc. The outer edge of the patterned area is just visible.

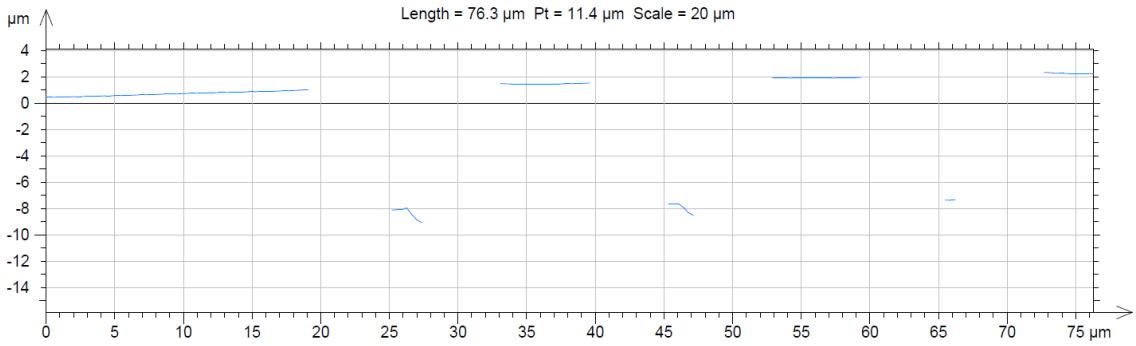

(a) Inner edge of structured area

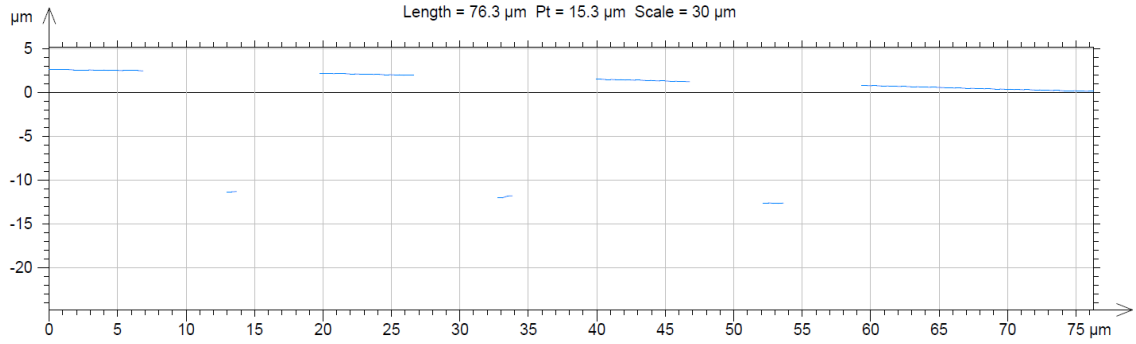

(b) Outer edge of structured area

Figure G.3: Profile of electroless nickel gratings, inner and outer edge

Appendix H

Encoder controlled AMB, locus plots

Figures H.1 and H.2 have been recorded by adding a sinusoidal excitation to the control current while the controller with a bias current of 1.3 A and a damping of 0.5 maintains stable hovering. Both figures show movements in horizontal direction. According to the Nyquist criterion the closed loop could be stabilized with an additional gain of 0.52 through 2.94, as can be seen in figure H.1. The phase margin is 42°. Figure H.2 indicates once more that this plant can only be stabilized if the controller incorporates phase lead because the phase of the plant is below -180° over a wide frequency range.

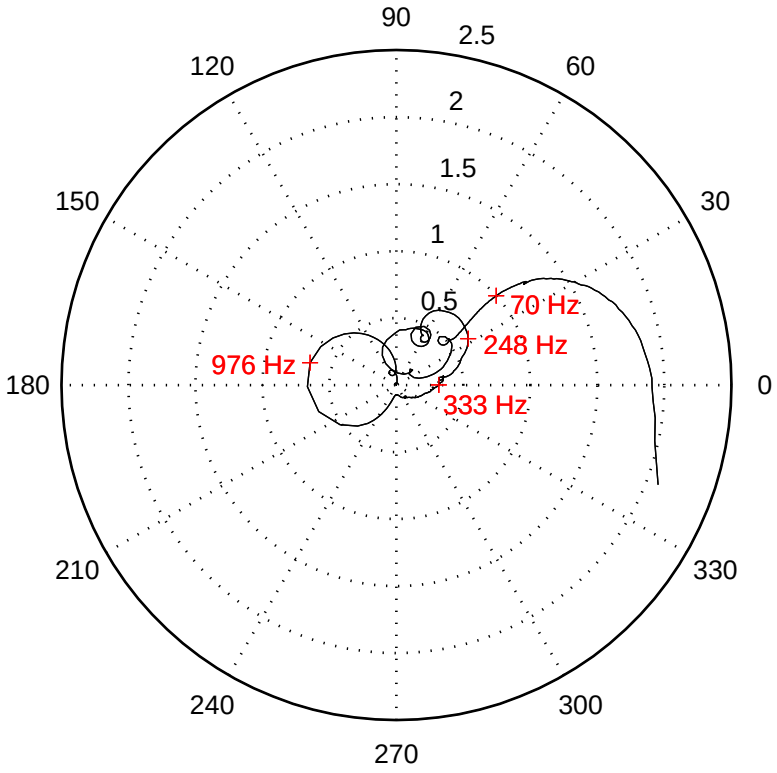

Figure H.1: AMB locus of open loop frequency response function recorded with encoders.

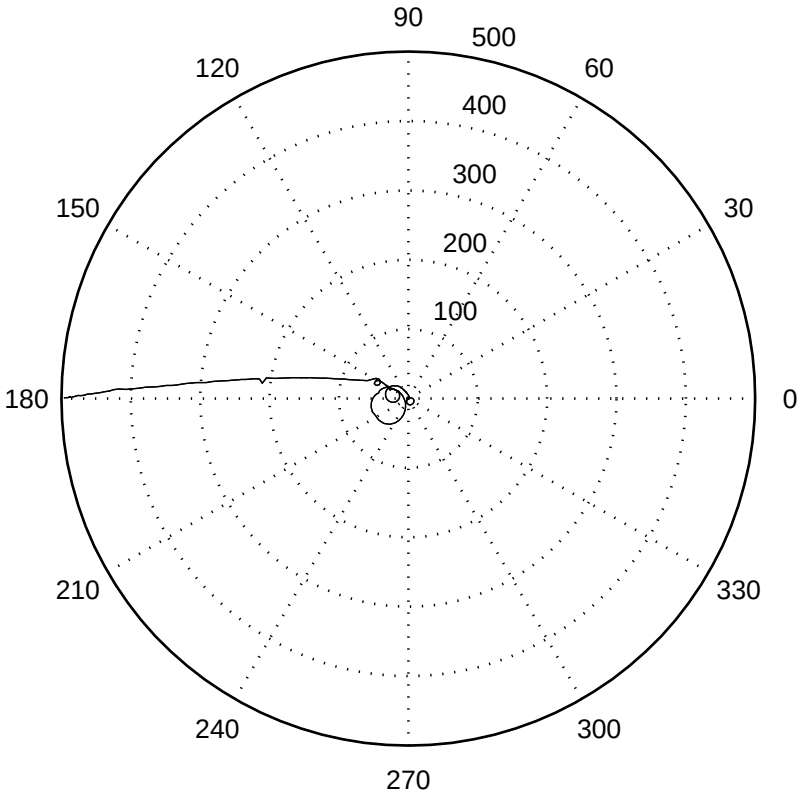

Figure H.2: Locus of plant frequency response function recorded with encoders. The unit is $\mu m/A$.

Appendix I

AMB experiments at higher speed of rotation

For the six experiments of figure I.1 the machine runs at three different rotational velocities, while the reference value of the magnetic bearing is $(0,0)$. It is controlled with encoders. 300 rpm represents the maximum required for the application and higher speeds have only been run to demonstrate the capabilities of the magnetic bearing. At $t = 0$ the machine accelerates the rotor and the magnetic bearing is started simultaneously. It takes a few seconds until the motor has reached its final speed. During this acceleration time the diameter of the error motion slowly increases on the right because the integrator reduces it at low speed. The experiments with PD control do not show this speed dependency.

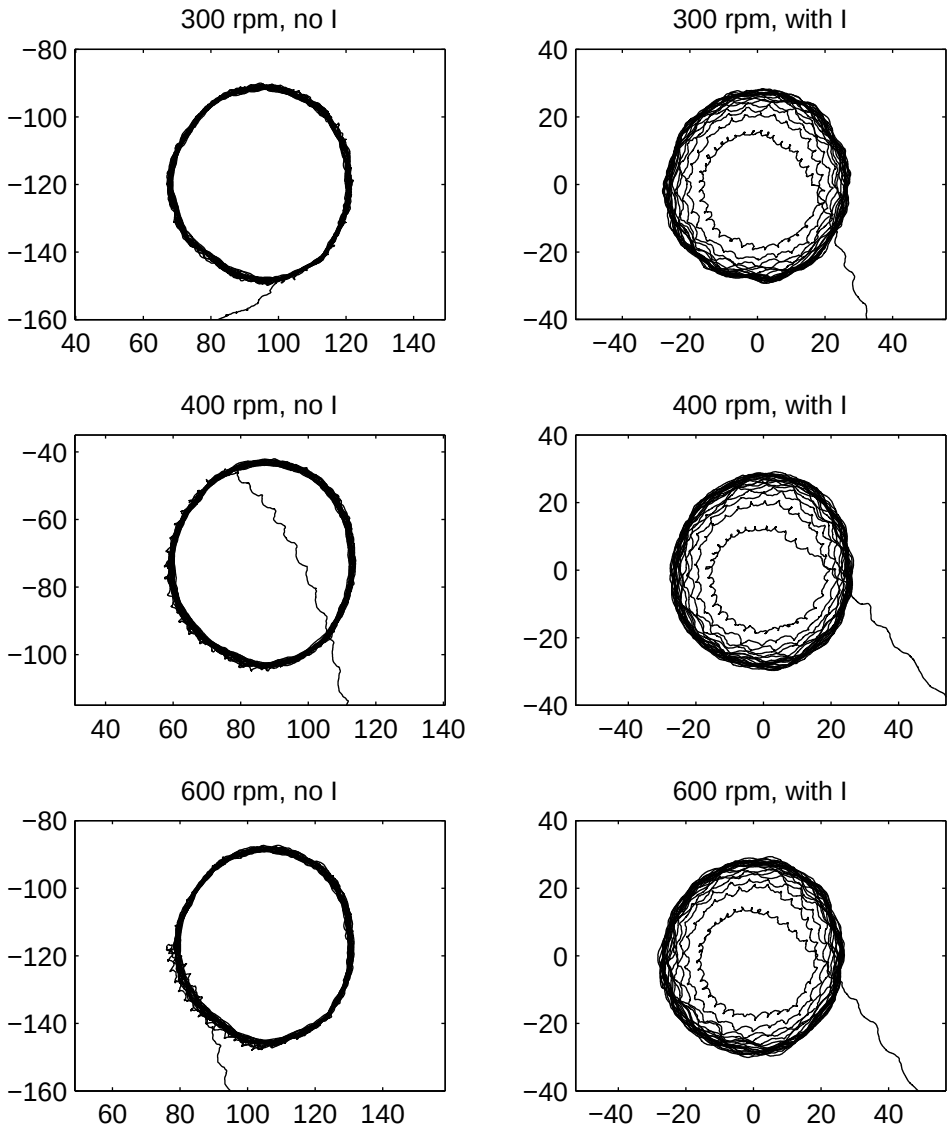

Figure I.1: Whirl motions at different rotational velocities recorded with encoders. Only the right column has been recorded with integrator. Units: μm

Bibliography

[1] ABEL, D. *Rapid Control Prototyping - Methoden und Anwendungen*. Springer, Berlin Heidelberg, Germany, 2006.

[2] AENIS, M., AND NORDMANN, R. Fault diagnosis in rotating machinery using active magnetic bearings. In *Proceedings of the Eighth International Symposium on Magnetic Bearings* (Mito, Japan, 26-28 August 2002), Dynamics and Control Lab., Dept. of Mechanical Eng., Ibaraki University, Hitachi, Japan, pp. 125–132.

[3] AEROTECH, INC. Ba10/20/30 series user's manual, 2002. `http://www.aerotechmotioncontrol.com/ftp/pwpsoftware/manuals_helpfiles/ControllerAccessories/BA%20Series%20Amplifiers/BA10_20_30.pdf` (accessed 4th April 2015).

[4] AESCHLIMANN, B. Control aspects of high precision active magnetic bearings, January 2001. MECOS AG, Lausanne, Switzerland, `http://www.mecos.com/pdf/PhDAeschlimann.pdf` (accessed 6th April 2015).

[5] ALTERA CORPORATION. Altera - measurable advantage, 2015. `https://www.altera.com/en/` (accessed 21st January 2015).

[6] ARREDONDO, I., AND JUGO, J. 2-dof controller design for precise positioning a spindle levitated with active magnetic bearings. *European Journal of Control 18*, 2 (2012), pp. 194–206.

[7] BARBARACI, G., MARIOTTI, G. V., AND PISCOPO, A. Active magnetic bearing design study. *Journal of Vibration and Control 19*, 16 (2012), pp. 2491–2505.

[8] BECHTLER, J., AND SPILGER, R. Positioning method for printing machine roller using control or regulation of roller magnetic bearing devices, 2002. patent DE10152839 A1, German Patent and Trade Mark Office - DPMA, Munich, Germany.

[9] BECK MASCHINENBAU. Linear guides and bearings, September 2014. `http://www.beck-maschinenbau.com/en/explanations.html` (accessed 1st November 2014).

[10] BLEULER, H., COLE, M. O. T., KEOGH, P. S., LARSONNEUR, R., MASLEN, E. H., NORDMANN, R., OKADA, Y., SCHWEITZER, G., AND TRAXLER, A. *Magnetic Bearings*. Springer, Berlin Heidelberg, Germany, 2009.

[11] BLEULER, H., GÄHLER, C., HERZOG, R., LARSONNEUR, R., MIZUNO, T., SIEGWART, R., AND WOO, S.-J. Application of digital signal processors for industrial magnetic bearings. *IEEE Transactions on Control Systems Technology 2*, 4 (1994), pp. 280–289.

[12] BROWN, C. N. Ruling engines, diffraction gratings and wavelength measurements before the rowland era. *Annuals of Science 72*, 1 (2015), pp. 28–74.

[13] BÜHLER, P. *Hochintegrierte Magnetlager-Systeme*. PhD thesis, Eidgenössische technische Hochschule Zürich, Zürich, Germany, 1995.

[14] CEN, J., KITSOMBOONLOHA, R., AND SUBRAMANIAN, V. Cell filling in gravure printing for printed electronics. *Langmuir 30*, 45 (2014), pp. 13716–13726.

[15] CHANG, J., LEE, S., LEE, K. B., LEE, S., CHO, Y. T., SEO, J., LEE, S., JO, G., YONG LEE, K., KONG, H.-S., AND KWON, S. Overlay accuracy on a flexible web with a roll printing process based on a roll-to-roll system. *Review of Scientific Instruments 86*, 5 (2015), pp. 1–8.

[16] CHEN, C. K., AND CHU, T. D. Nonlinear modeling and control of active magnetic bearings for a flywheel energy storage system. In *Proceedings of the Sixth International Conference on Intelligent Human-Machine Systems and Cybernetics, IHMSC* (Hangzhou, China, 26-27 August 2014), vol. 1, IEEE, Piscataway, NJ, USA, pp. 284–287.

[17] CHEN, K.-S., TRUMPER, D., AND SMITH, S. Design and control for an electromagnetically driven x-y-θ stage. *Precision Engineering 26*, 4 (2002), pp. 355–369.

[18] COLE, M. O. T., KEOGH, P. S., AND BURROWS, C. R. Robust control of multiple discrete frequency vibration components in rotor - magnetic bearing systems. *JSME International Journal, Series C: Mechanical Systems, Machine Elements and Manufacturing 46*, 3 (2003), pp. 891–899.

[19] CRAWFORD, G. P. *Flexible Flat Panel Displays*. J. Wiley & Sons, Chichester, UK, 2005.

[20] CULLITY, B. D. *Introduction to Magnetic Materials*. Addison-Wisley Publishing Company, London, UK, 1972.

[21] DAVIES, M. A., DUTTERER, B. S., SULESKI, T. J., SILNY, J. F., AND KIM, E. D. Diamond machining of diffraction gratings for imaging spectrometers. *Precision Engineering 36*, 2 (2012), pp. 334–338.

[22] DENKENA, B., GUEMMER, O., AND FLOETER, F. Evaluation of electromagnetic guides in machine tools. *CIRP Annals - Manufacturing Technology 63*, 1 (2014), 357–360.

[23] DR. JOHANNES HEIDENHAIN GMBH. Encoders for servo drives, November 2014. Traunreut, Germany, http://www.heidenhain.de/de_EN/php/documentation-information/brochures/popup/media/media/file/view/file-0040/file.pdf (accessed 30th November 2014).

[24] DR. JOHANNES HEIDENHAIN GMBH. Exposed linear encoders, November 2014. Traunreut, Germany, http://www.heidenhain.de/de_EN/php/documentation-information/brochures/popup/media/media/file/view/file-0436/file.pdf#page= (accessed 1st December 2014).

[25] DR. JOHANNES HEIDENHAIN GMBH. Interfaces of heidenhain encoders, March 2015. Traunreut, Germany, https://www.heidenhain.de/de_EN/php/documentation-information/brochures/popup/media/media/file/view/file-0668/file.pdf (accessed 1st May 2015).

[26] DSPACE. dspace hardware, 2015. http://www.dspace.com/en/ltd/home/products/hw.cfm (accessed 15th March 2015).

[27] EPSRC CENTRE FOR INNOVATIVE MANUFACTURING IN ULTRA PRECISION. Annual report 2012/13, June 2014. Cranfield, Bedfordshire, UK, http://www.ultraprecision.org/wp-content/uploads/2014/06/EPSRC-Centre-in-UP-Annual-Report-12-13.pdf (accessed 10th November 2014).

[28] EPSRC CENTRE FOR INNOVATIVE MANUFACTURING IN ULTRA PRECISION. Report on the roadmapping workshop for the epsrc centre for innovative manufacturing in ultra precision, May 2014. Cranfield, Bedfordshire, UK, http://www.ultraprecision.org/wp-content/uploads/2014/07/CIM-UP-R2R-Roadmap-Report-May-20141.pdf (accessed 5th January 2015).

[29] EPSRC CENTRE FOR INNOVEATIVE MANUFACTURING IN ULTRA PRECISION. Mid-term report 2014, May 2014. Cranfield, Bedfordshire, UK, http://www.ultraprecision.org/wp-content/uploads/2014/06/EPSRC-Centre-in-UP-Mid-Term-Report.pdf (accessed 2nd Januar 2015).

[30] ERNST, A. *Digital Linear and Angular Metrology*, 3rd ed. verlag moderne industrie, Landsberg/Lech, Germany, 1998.

[31] FG-AMB FOSHAN GENESIS. Homepage, 2015. http://www.fgamb.com/ (accessed 12th May 2015).

[32] FLEMING, A. J. A review of nanometer resolution position sensors: Operation and performance. *Sensors and Actuators A: Physical 190* (2013), pp. 106–126.

[33] FOURKA, M., AND BONIS, M. Comparison between externally pressurized gas thrust bearings with different orifice and porous feeding systems. *Wear 210*, 1-2 (1997), pp. 311–317.

[34] FUJIMAKI, K., AND MITSUI, K. Development of an optical measuring device for rotation accuracy of micro-spindle. In *Proceedings of the Eleventh International Conference on Precision Engineering (ICPE)* (Norfolk, VA, 9-14 October 2006), no. 5, ASPE, Raleigh, NC, USA, pp. 83–88.

[35] FUJIWARA, H., EBINA, K., ITO, M., TAKAHASHI, N., AND MATSUSHITA, O. Control of flexible rotors supported by active magnetic bearings. In *Proceedings of the Eighth International Symposium on Magnetic Bearings* (Mito, Japan, 26-28 August 2002), Dynamics and Control Lab., Dept. of Mechanical Eng., Ibaraki University, Hitachi, Japan, pp. 145–150.

[36] FÖRCH, P., AND HENN, A. Method and device for aligning flat copies in sheet-processing machines, 2003. patent US 6604739 B2, United States Patent and Trademark Office, Alexandria, Virginia, USA.

[37] GAO, W., ARAKI, T., KIYONO, S., OKAZAKI, Y., AND YAMANAKA, M. Precision nano-fabrication and evaluation of a large area sinusoidal grid surface for a surface encoder. *Precision Engineering 27*, 3 (2003), pp. 289–298.

[38] GAO, W., TANO, M., ARAKI, T., KIYONO, S., AND PARK, C. H. Measurement and compensation of error motions of a diamond turning machine. *Precision Engineering 31*, 3 (2007), pp. 310–316.

[39] GOLDMAN, A. *Handbook of Modern Ferromagnetic Materials*. Kluwer Academic Publishers, Norwell, Massachusetts, USA, 1999.

[40] GOMWE, T. Reel to reel film positioning of plastic substrates. Master's thesis, Cranfield University, Cranfield, Bedfordshire, UK, 2014.

[41] GROCHMAL, T., AND LYNCH, A. Experimental comparison of nonlinear tracking controllers for active magnetic bearings. *Control Engineering Practice 15*, 1 (2007), pp. 95–107.

[42] HARRIS, T. A. *Rolling Bearing Analysis*, 2nd ed. John Wiley & Sons, New York, USA, 1984.

[43] HE, D., MORITA, H., ZHANG, X., SHINSHIC, T., NAKAGAWA, T., SATO, T., AND MIYAKE, H. Development of a novel 5-dof controlled maglev local actuator for high-speed electrical discharge machining. *Precision Engineering 34*, 3 (2010), pp. 453–460.

[44] HERZOG, R., AND BÜHLER, P. Unbalance compensation using generalized notch filters in the multivariable feedback of magnetic bearings. *IEEE Transactions on Control Systems Technology 4*, 5 (1996), pp. 580–586.

[45] HOFFMANN, K.-J. *Integrierte aktive Magnetlager*. PhD thesis, Technische Universität Darmstadt, Darmstadt, Germany, 1999.

[46] HOFFMANN, K.-J., LAIER, D., AND MARKERT, R. Non-linear control of magnetically supported rotors, 1997. Technische Universität Darmstadt, Darmstadt, Germany, `http://www.sdy.tu-darmstadt.de/media/fachgebiet_sdy/dokumente_6/verffentlichungen/mag_al97.pdf` (accessed 24th January 2015).

[47] HOLMES, M., HOCKEN, R., AND TRUMPER, D. The long-range scanning stage: a novel platform for scanned-probe microscopy. *Precision Engineering 24*, 3 (2000), pp. 191–209.

[48] HUMPHREY, M., HILTON, E., AND ALLAIRE, P. Experiences using rt-linux to implement a controller for a high speed magnetic bearing system. In *Proceedings of the Fifth IEEE Real-Time Technology and Applications Symposium* (Vancouver, Canada, 02 - 04 June 1999), IEEE, Los Alamitos, USA, pp. 121–130.

[49] INNOVATIVE INTEGRATION. X3-servo framework logic user guide, March 2014. `http://www.innovative-dsp.com/cgi-bin/dlDocs.cgi?product=X3-Servo` (accessed 2nd February 2014).

[50] JABBEN, L. *Mechatronic Design of a Magnetically Suspended Rotating Platform*. PhD thesis, Technical University Delft, Delft, Netherlands, 2007.

[51] JAYANTH, V. Identification and control of a flexible rotor supported on active magnetic bearings. In *Proceedings of the IEEE SoutheastCon* (North Carolina, USA, 05-07 April 2002), IEEE, New York, USA, pp. 273–278.

[52] JEON, S., AHN, H.-J., HAN, D.-C., AND CHANG, I.-B. New design of cylindrical capacitive sensor for on-line precision control of amb spindle. *IEEE Transactions on Instrumentation and Measurement 50*, 3 (2001), pp. 757–763.

[53] JING, Y., XIANG, H. Q., AND KAI, W. Effects of amb power amplifier structure upon the system performance. In *Proceedings of the Eighth International Symposium on Magnetic Bearings* (Mito, Japan, 26-28 August 2002), Dynamics and Control Lab., Dept. of Mechanical Eng., Ibaraki University, Hitachi, Japan, pp. 97–100.

[54] JIRIGALANTU, Z. F. The design of chisel-edge ruling tool for diffraction gratings. In *Proceedings of the International Conference on Mechatronic Science, Electric*

Engineering and Computer, MEC (Jilin, China, 19-22 August 2011), IEEE, Piscataway, NJ, pp. 699–702.

[55] KEMPER, H. Schwebebahn mit raederlosen fahrzeugen, die an eisernen fahrschienen mittels magnetischer felder schwebend entlang gefuehrt werden, 1937. patent DE643316 C, German Patent and Trade Mark Office - DPMA, Munich, Germany.

[56] KHANFIR, H., BONIS, M., AND REVEL, P. Improving waviness in ultra precision turning by optimizing the dynamic behavior of a spindle with magnetic bearings. *International Journal of Machine Tools and Manufacturing 45*, 7-8 (2005), pp. 841–848.

[57] KIM, D. G., AND KIM, K. W. The influence of the machining and assembling errors on the performance of the shaft supported by active magnetic bearings. *JSME International Journal Series C-mechanical Systems Machine Elements and Manufacturing 41*, 2 (1998), pp. 313–320.

[58] KIM, H.-S., AND KIM, E.-J. Feed-forward control of fast tool servo for real-time correction of spindle error in diamond turning of flat surfaces. *International Journal of Machine Tools and Manufacturing 43*, 12 (2003), pp. 1177–1183.

[59] KIM, O.-S., LEE, S.-H., AND HAN, D.-C. Positioning performance and straightness error compensation of the magnetic levitation stage supported by the linear magnetic bearing. *IEEE Transactions on Industrial Electronics 50*, 2 (2003), pp. 374–378.

[60] KIMMAN, M. H., LANGEN, H. H., AND MUNNIG SCHMIDT, R. H. A miniature milling spindle with active magnetic bearings. *Mechatronics 20*, 2 (2010), pp. 224–235.

[61] KNAPP, B. R., ARNESON, D. A., LIEBERS, M. J., OSS, D. D., AND MARSH, E. R. Design and testing of a step compensated bi-conic hydrostatic spindle. In *Proceedings of the 24th Annual Meeting of the American Society for Precision Engineering, ASPE* (Monterey, CA, United States, 4-9 October 2009), ASPE, Raleigh, NC, USA, pp. 1–4.

[62] KOSMYNIN, A. V., AND SHCHETININ, V. S. Carrying capacity of gas-magnetic bearings for high-speed spindles. *Russian Engineering Research 30*, 12 (2010), pp. 1252–1253.

[63] KOSMYNIN, A. V., SHCHETININ, V. S., IVANOVA, N. A., KHVOSTIKOV, A. V., AND BLINKOV, S. S. Test bench for determining the output characteristics of a spindle on gas-magnetic bearings. *Russian Engineering Research 30*, 8 (2010), pp. 816–817.

[64] LEE, C.-W., YOON, Y.-K., AND JEONG, H.-S. Compensation of tool axis misalignment in active magnetic bearing spindle system. *KSME International Journal 11*, 2 (1997), pp. 155–163.

[65] LEE, J., SEONG, J., PARK, J., PARK, S., LEE, D., AND SHIN, K.-H. Register control algorithm for high resolution multilayer printing in the roll-to-roll process. *Mechanical Systems and Signal Processing 60*, 1 (2015), 706–714.

[66] LEMBKE, T. A. *Design and Analysis of a Novel Low Loss Homopolar Electrodynamic Bearing*. PhD thesis, Royal Institute of Technology, Sweden, Stockholm, Sweden, 2005.

[67] LI, G., XU, Z., FANG, F., WUA, W., XING, X., LI, W., AND LIU, H. Micro cutting of v-shaped cylindrical grating template for roller nano-imprint. *Journal of Materials Processing Technology 213*, 6 (2013), pp. 895–904.

[68] LI, L., SHINISHI, T., IIJIMA, C., ZHANG, X., AND SHIMOKOHBE, A. Compensation of rotor imbalance for precision rotation of a planar magnetic bearing rotor. *Precision Engineering 27*, 2 (2003), pp. 140–150.

[69] LI, L., SHINSHI, T., ZHANG, X., AND SHIMOKOHBE, A. A simple method for rotation about the inertial axis of a rigid amb rotor. In *Proceedings of the Eighth International Symposium on Magnetic Bearings* (Mito, Japan, 26-28 August 2002), Dynamics and Control Lab., Dept. of Mechanical Eng., Ibaraki University, Hitachi, Japan, pp. 405–410.

[70] LION PRECISION. Noncontact displacement sensors, 2015. `http://www.lionprecision.com/eddy-current-sensors/ecl150.html` (accessed 12th December 2014).

[71] LIU, C.-H., SUNG, C.-K., CHANG, E.-C., LO, C.-Y., AND FU, C.-C. Fabricating a silver soft mold on a flexible substrate for roll-to-roll nanoimprinting. *IEEE Transactions on Nanotechnology 13*, 1 (2014), pp. 80–84.

[72] LIU, S., XU, F., LU, C., AND BIAN, Z. Design of experiments for the feedback circuit of power amplifier with magnetic bearings. In *Proceedings of the Eighth International Symposium on Magnetic Bearings* (Mito, Japan, 26-28 August 2002), Dynamics and Control Lab., Dept. of Mechanical Eng., Ibaraki University, Hitachi, Japan, pp. 107–112.

[73] LOCKE, D. H., SWANSON, E. S., WALTON, J. F., WILLIS, J. P., AND HESHMAT, H. Testing of a centrifugal blood pump with a high efficiency hybrid magnetic bearing. *ASAIO Journal 49*, 6 (2003), pp. 737–743.

[74] LOEWEN, E. G., AND POPOV, E. *Diffraction Gratings and Applications*. Marcel Decker, Inc. New York, USA, 1997.

[75] LU, X., DYCK, M., AND ALTINTAS, Y. Magnetically levitated six degree of freedom rotary table. *CIRP Annals - Manufacturing Technology 1*, 64 (2015), pp. 353–356.

[76] LUO, X., CHENG, K., WEBB, D., AND WARDLE, F. Design of ultraprecision machine tools with applications to manufacture of miniature and micro components. *Journal of Materials Processing Technology 167*, 2-3 (2005), pp. 515–528.

[77] MARESCA, R. L. An integrated magnetic actuator and sensor for use in linear or rotary magnetic bearings. *IEEE Transactions on Magnetics 19*, 5 (1983), pp. 2094–2096.

[78] MICRO-EPSILON. Sensors & measurement systems, 2015. `http://www.micro-epsilon.com/index.html` (accessed 22th June 2015).

[79] MITENKOV, P. M., KODOCHIGOV, N. G., LEBEDEV, S. V., AND HODYKIN, A. V. Comparing the quality of a controlling rotor with active magnetic bearings for linear and non-linear system structures. *Journal of Machinery Manufacture and Reliability 40*, 6 (2011), pp. 561–564.

[80] MORO, M., AND TANIGUCHI, J. Removal of residual layer by liquid transfer imprint lithography using roll-to-roll uv-nil. *Microelectronic Engineering 141*, 15 (2015), pp. 112–116.

[81] MUNNIG SCHMIDT, R. H., SCHITTER, G., AND EIJK, J. *The Design of High Performance Mechatronics*. Technical University Delft, Delft, Netherlands, 2011.

[82] MÜLLER, S., SCHAUDT, H., AND TRAJKOVIC, D. Flat multilayer commodity punching device for use in printing machine, has punching and counter punching cylinders, in which one is held in radially shiftable magnetic bearing to adjust breadth of punching gap between cylinders, 2005. patent DE 102005016779 A1, German Patent and Trade Mark Office - DPMA, Munich, Germany.

[83] NIPPON STEEL & SUMITOMO METAL. Electrical steel sheets, 2015. `http://www.nssmc.com/product/catalog_download/pdf/D003jec.pdf` (accessed 12th February 2015).

[84] NOH, J. Scalability of roll-to-roll gravure-printed electrodes on plastic foils. *IEEE Transactions on Electronics Packaging Manufacturing 33*, 4 (2010), pp. 275–283.

[85] NOH, J. Key issues with printed flexible thin film transistors and their application in disposable rf sensors. *Proceedings of the IEEE 103*, 4 (2015), pp. 554–566.

[86] NOH, J., KIM, S., JUNG, K., KIM, J., CHO, S., AND CHO, G. Fully gravure printed half adder on plastic foils. *IEEE Electron Device Letters 32*, 11 (2011), pp. 1555–1557.

[87] NOH, M. D., JEONG, M.-K., AND PARK, B.-C. Development of a low cost inductive sensor unsing switching noise demodulation. In *Proceedings of the Eighth International Symposium on Magnetic Bearings* (Mito, Japan, 26-28 August 2002), Dynamics and Control Lab., Dept. of Mechanical Eng., Ibaraki University, Hitachi, Japan, pp. 311–314.

[88] OBERBECK, C., AND ULBRICH, H. Investigations in a software-based design of linear electromagnetic actuators. In *Proceedings of the Eighth International Symposium on Magnetic Bearings* (Mito, Japan, 26-28 August 2002), Dynamics and Control Lab., Dept. of Mechanical Eng., Ibaraki University, Hitachi, Japan, pp. 157–162.

[89] OKADA, Y., SAITOH, T., AND SHINODA, Y. Vibration control of flexible rotor supported by inclination control magnetic bearings. *IEEE/ASME International Conference on Advanced Intelligent Mechatronics, AIM* (19-23 September, 1999 1999), pp. 788–793.

[90] PARK, Y. H., HAN, D. C., PARK, I. H., AHN, H. J., AND JANG, D. Y. A self-sensing technology of active magnetic bearings using a phase modulation algorithm based on a high frequency voltage injection method. *Journal of Mechanical Science and Technology 22*, 9 (2008), pp. 1757–1764.

[91] PETZOLD, O. *Modellbildung und Untersuchung eines magnetisch gelagerten Rundtisches*. PhD thesis, Otto-von-Guericke-Universität Magdeburg, Magdeburg, Germany, December 2006.

[92] POLAJZER, B., RITONJA, J., STUMBERGER, G., DOLINAR, D., AND LECOINTE, J.-P. Decentralized pi/pd position control for active magnetic bearings. *Electrical Engineering 89*, 1 (2006), pp. 53–59.

[93] POWELL, J. W. *Design of Aerostatic Bearings*. The Machinery Publishing Co, Ltd, London Tonbridge, UK, 1970.

[94] RUSKOWSKI, M. *Aufbau und Regelung aktiver Magnetführungen*. PhD thesis, Leibniz University Hanover, Hanover, Germany, 2004.

[95] RUSKOWSKI, M., AND POPP, K. Improved position control of a magnetic guide using acceleration measurement and a laser position reference. In *Proceedings of the Eighth International Symposium on Magnetic Bearings* (Mito, Japan, 26-28 August 2002), Dynamics and Control Lab., Dept. of Mechanical Eng., Ibaraki University, Hitachi, Japan, pp. 305–310.

[96] SAKET, F. Y., SAHINKAYA, M. N., AND KEOGH, P. S. Touchdown bearing contact forces in magnetic bearing systems. In *Proceedings of the ASME Turbo Expo* (San Antonio, Texas, USA, 3-7 June 2013 2013), ASME, pp. 1–7.

[97] SANCHEZ-BREA, L. M., AND MORLANES, T. Metrological errors in optical encoders. *Measurement Science & Technology 19*, 11 (2008), pp. 1–8.

[98] SAWICKI, J. T., MASLEN, E. H., AND BISCHOF, K. R. Modeling and performance evaluation of machining spindle with active magnetic bearings. *Journal of Mechanical Science and Technology 21*, 6 (2007), pp. 847–850.

[99] SCHAEFFLER. Printing machines, 2014. `http://www.schaeffler.com/content.schaeffler.de/en/branches/industry/printing_machines/index.jsp` (accessed 1st December 2014).

[100] SCHUHMANN, T., HOFMANN, W., AND WERNER, R. Improving operational performance of active magnetic bearings using kalman filter and state feedback control. *IEEE Transactions on Industrial Electronics 59*, 2 (2012).

[101] SCHWEITZER, G., TRAXLER, A., AND BLEULER, H. *Magnetlager - Grundlagen, Eigenschaften und Anwendungen berührungsfreier, elektromagnetischer Lager*. Springer, Berlin Heidelberg, Germany, 1993.

[102] SETIAWAN, J. D., MUKHERJEE, R., MASLEN, E. H., AND SONG, G. Adaptive compensation of sensor runout and mass unbalance in magnetic bearing systems. In *Proceedings of the IEEE/ASME International Conference on Advanced Intelligent Mechatronics* (Atlanta, USA, 19-23 September 1999), IEEE, Piscataway, NJ, USA, pp. 800–805.

[103] SHI, J., ZMOOD, R., AND QIN, L. Synchronous disturbance attenuation in magnetic bearing systems using adaptive compensating signals. *Control Engineering Practice 12*, 3 (2004), pp. 283–290.

[104] SHIN, D., AND KIM, J. Design and implementation of pcb-type capacitance displacement sensor collocated with magnetic bearings. *Sensors and Actuators A:Physical 71*, 3 (1998), pp. 223–229.

[105] SHINSHI, T., IIJIMA, C., ZHANG, X., CHOI, K.-B., SATO, K., AND SHIMOKOHBE, A. Precision radial magnetic bearing. In *Proceedings of the Fifteenth Annual Meeting of the American Society for Precision Engineering* (Scottsdale, Arizona, USA, 22-27 October 2000), American Society of Precision Engineering, Raleigh, USA, pp. 240–243.

[106] SKF GROUP. Super-precision axial-radial cylindrical roller bearings, February 2012. `http://www.skf.com/binary/21-57509/Super-precision-axial-radial-cylindrical-roller-bearings-06318_3_EN.pdf` (accessed 22nd December 2014).

[107] SKOGESTAD, S., AND POSTLETHWAITE, I. *Multivariable Feedback Control - Analysis and design*. John Wiley & Sons, Chichester, UK, 1992.

[108] SLOCUM, A. H. *Precision Machine Design*. Prentice-Hall, New Jersey, USA, 1992.

[109] SPEEDGOAT. speedgoat - real-time simulation and testing, 2015. `https://www.speedgoat.ch/Products.aspx` (accessed 16th Mai 2015).

[110] SRIDHARAN, G. Electro-optical position measurement for active magnetic bearing. *Review of Scientific Instruments 56*, 1 (1985), pp. 142–145.

[111] STANSFIELD, F. M. *Hydrostatic Bearings*. The Machinery Publishing Co, Ltd, Chicago, IL, USA, 1970.

[112] STÖLTING, H.-D., KALLENBACH, E., AND AMRHEIN, W. *Handbook of Fractional - Horsepower Drives*. Springer, Berlin Heidelberg, Germany, 2008.

[113] SU, W., ZHENG, K., LIU, H., AND YU, L. Time delay effects on amb systems. In *Proceedings of the IEEE International Conference on Mechatronics and Automation, ICMA* (Changchun, China, 9-12 August 2009), S. Guo, T. Fukuda, Y. Yo, and H. Yu, Eds., vol. 1-7, IEEE, Piscataway, NJ, USA, pp. 4682–4686.

[114] SZE-WEI, G., HAN-SEOK, L., RAHMAN, M., AND WATT, F. A fine tool servo system for global position error compensation for a miniature ultra-precision lathe. *International Journal of Machine Tools & Manufacture 47*, 7-8 (2007), pp. 1302–1310.

[115] TRAXLER, A. *Eigenschaften und Auslegung von berührungsfreien elektromagnetischen Lagern*. PhD thesis, Eidgenossische technische Hochschule Zuerich, 1985.

[116] VAVILOV, V. E., GERASIN, A. A., ISMAGILOV, F. R., AND KHAIRULLIN, I. K. An algorithm for controlling hybrid magnetic using the magnetic field pattern. *Journal of Computer and Systems Sciences International 52*, 5 (2013), pp. 794–799.

[117] W. B. ROWE, J. P. O. *Design Procedures for Hydrostatic Bearings*. The Machinery Publishing Co, Ltd, London, UK, 1971.

[118] WALCHER, H. *Position Sensing - Angle and Distance Measurement for Engineers*. Butterworth-Heinemann Ltd, Oxford, UK, 1994.

[119] WORLITZ, F. Aktive magnetlager und ihre anwendungen, 2014. Hochschule Zittau/Görlitz, Zittau, Germany, `http://ipm.hszg.de/en/institute/publikationen/publikationen-ipm/article/aktive-magnetlager-und-ihre-anwendungen.html` (accessed 20th December 2014).

[120] XIAO, W. *Beitrag zur Entwicklung von Magnetlager- und Fuzzy-Systemen*. PhD thesis, Universität Kassel, Germany, Kassel, Germany, 1994.

[121] XILINX. Xilinx all programmable, 2015. `http://www.xilinx.com/` (accessed 22th January 2015).

[122] XIPING, W., LIANG, Y., JINGUI, W., AND WEIDONG, C. Analysis on stiffness and damping performance of active magnetic bearing system. *Journal of Shanghai University 2*, 3 (1998), pp. 221–225.

[123] YAN, J., OOWADA, T., ZHOU, T., AND KURIYAGAWA, T. Precision machining of microstructures on electroless-plated nip surface for molding glass components. *Journal of Materials Processing Technology 209*, 10 (2009), pp. 4802–4808.

[124] YOON, S. Y. *Control of Surge in Centrifugal Compressors by Active Magnetic Bearings*. Springer, 2013.

[125] ZHANG, X., SHINSHI, T., LI, L., AND SHIMOKOHBE, A. Combined repetitive control for precision radial magnetic bearing. In *Proceedings of the Eighth International Symposium on Magnetic Bearings* (Mito, Japan, 26-28 August 2002), Dynamics and Control Lab., Dept. of Mechanical Eng., Ibaraki University, Hitachi, Japan, pp. 433–438.

[126] ZHANG, X., SHINSHI, T., LI, L., AND SHIMOKOHBE, A. Precision control for rotation about estimated center of inertia of spindle supported by radial magnetic bearing. *JSME International Journal, Series C: Mechanical Systems, Machine Elements and Manufacturing 47*, 1 (2004), 242–250.

[127] ZHANG, X., WANG, D., YU, X., SU, Z., WU, L., AND YI, X. Force-current factor investigation of a radial active magnetic bearing with large load capacity. In *Transportation Electrification Asia-Pacific (ITEC Asia-Pacific)* (Beijing, China, 31 August - 3 Semptember 2014), IEEE, Piscataway, NJ, USA, pp. 1–4.

[128] ZHANG, X. Y., SHINSHI, T., LI, L., CHOI, E. B., AND SHIMOKOHBE, A. Precision control of radial magnetic bearing. In *Initiatives of Precision Engineering at the Beginning of a Millennium* (Yokohama, Japan, 18-20 July 2001), Springer, Dordrecht, Netherlands, pp. 714–718.

[129] ZHAO, G. Advanced bearing system for ultra precision plastic electronics production systems. Master's thesis, Cranfield University, Cranfield, Bedfordshire, UK, 2014.